

# More than a century of rotor research

## 1.1. Introduction

Rotor aerodynamics has a history of more than a century, with the first performance prediction that still holds today published exactly 100 years ago. Joukowsky (1918) used a very simplified model of a rotor, the actuator disc, to connect thrust, velocity and power for predicting the performance of a ‘static’ rotor like a hovering helicopter rotor. A century later, rotor aerodynamics has several branches: ship screws, propellers, helicopter rotors and wind turbine rotors. All branches have excellent textbooks and survey papers, like Breslin and Andersen (1994) for ship propellers, Wald (2006) for propellers, Leishman (2006) for helicopter rotors and Schaffarczyk (2014) for wind turbine rotors. Especially the latter application, wind turbines, has been growing very fast over the last decades, giving rise to more specialized books like Sørensen (2015) and Branlard (2017), textbooks like Hansen (2008), Burton et al. (2011) and Manwell et al. (2009) in which rotor aerodynamics is treated as part of wind turbine design, and survey papers like Okulov et al. (2015) and van Kuik et al. (2015a). Loads, performance and dynamic behaviour can now be calculated with high accuracy under conditions that were unimaginable 100 years ago: rotors having diameters approaching 200 m, operating in the earth boundary layer with often high turbulence levels and extreme gusts, interacting with the neighbouring turbines when placed in a wind farm, and designed for 20 years lifetime.

This book returns to the rotor theories as developed in the first decades of rotor aerodynamic history, with the objective to renew the physical interpretation of some flow phenomena observed for heavily loaded discs and rotors, to complement the theory with knowledge about flow details which has become into reach by modern computing power, and to expand the theory to its limits of operation. Section 1.4 presents the questions which will be addressed, preceded by sections on the history of rotor aerodynamics, with special attention to the development of the actuator disc model. With its origin in the late 19<sup>th</sup> century this model is the basis for modern rotor design and analysis methods.

## 1.2. History of the actuator disc momentum theory

The three European aerodynamic research schools that were famous in the first half of the 20<sup>th</sup> century have contributed significantly to actuator disc momentum theory: the British school led by Froude and Lanchester, the German school led by Prandtl and Betz, and the Russian school led by Joukowsky and Vetchinkin. These contributions are reviewed in retrospect, based on van Kuik

Table 1.1: From actuator disc theory to BEM: the main contributions and contributors

contributions	British school	German school	Russian school
Actuator disc theory	1865 Rankine 1889 Froude	1904 Finsterwalder 1910 Bendemann	1913 Vetchinkin 1917 Bothezat 1918 Joukowsky
First power performance for the static disc			
Confirmation by vortex theory		1919 Betz, Prandtl	1912-1918 Joukowsky
Expansion to wind turbines, formulation of $C_{p,max}$		Aug.1920 Munk Sept.1920 Betz Jul.1921 Hoff	Febr.1920 Joukowsky
Blade element theory			1920 Drzewiecki
BEM: the Blade Element Momentum theory	1935 Glauert		

(2007) and Okulov and van Kuik (2012). In table 1.1 the main contributions are shown.

**1.2.1. The British School.** The idea to replace a rotor by an actuator disc goes back to the work of Rankine (1865). However, only in 1889 Froude has for the first time found a correct dynamic interpretation of the actuator disc action showing that for such a theoretical propeller one half the acceleration must take place before the propeller and the other half behind it. Unfortunately, the discussion on the question whether the contraction or expansion of the stream tube takes place before or behind the disc continued after Froude's paper, despite his formal mathematical treatment. Vetchinkin (1913, 1918), who was a pupil of Joukowsky, sought an explanation for the denial of Froude's result in the misunderstanding of the relation between the action of a disc and of real rotor blades. Most scientists at that time thought, erroneously, that the flow before the rotor plane is undisturbed, then receives a full speed alteration when it moves through the rotor blades, after which the flow behind the rotor is undisturbed too. From 1910 to 1915 there was a lively discussion in the Institution of Naval Architects (see issues 52, 53, 55 and 56 of their Transactions). The author of the last article is Lanchester (1915). In his analysis, Lanchester supports the energy and momentum balance as defined by Froude. However, Lanchester continues the discussion on the 'difficulties of regime' started by Froude, in particular on the pressure discontinuity at the disc edge. Although Lanchester says that 'the admitted difficulty relating to the edge of the actuator disc is probably more apparent than real', his next step is to substitute the continuously operating disc by an intermittently operating disc shedding vortex rings into the flow. Lanchester

**EXPLANATION 1.1. Froude's actuator disc** [Froude \(1889\)](#) formulated the earliest concept of the actuator disc: a permeable disc with a uniform pressure jump, representing a propeller with infinite rotational speed operating in a uniform parallel flow. The associated momentum theory is sometimes called the one-dimensional theory as it includes only the momentum balance in 1 direction, the axial direction. This concept is called 'Froude's disc' in contrast to **Joukowsky's actuator disc**. [Joukowsky \(1912\)](#) formulated the concept of the actuator disc with wake rotation: a permeable disc with an axial load and a torque, representing a propeller with a finite rotational speed operating in a uniform parallel flow. The associated momentum theory is sometimes called the two-dimensional theory as it includes not only the momentum balance in axial direction, but also the balance of angular momentum. See also Explanations [3.1](#).

states that a considerable portion of the change in kinetic energy is now to be found in the outer portions of the vortex rings, so outside the stream tube passing through the disc. According to modern insights in vorticity dynamics, Lanchester's statement is incorrect since he should include also the pressure- and unsteady terms arising from the intermittent operation in the energy equation. It is here where Lanchester deviates from Froude and leaves the possibility open that the velocity at the disc is not the average of the velocities far up- and downstream.

**1.2.2. The German and Russian School.** In 1917 [Bothezat](#) has generalized the result about the doubling of the induced velocity in the wake for actuator discs producing not only a forward but also a rotary movement in the wake. Joukowsky published a series of 4 papers on propeller aerodynamics in [1912; 1914; 1915; 1918](#). In the 4<sup>th</sup> paper he finally formulated the modern state of Froude's theory. This history has been supported and extended by [Hoff \(1921\)](#) who indicated Finsterwalder as the scientist who established the theory too, which was extended by [Bendemann \(1910\)](#).

Although Froude's theory was accepted by many scientists, it was not yet possible to show a connection between the abstraction of the actuator disc and the action of real blades on the flow. During the first two decades of the 20<sup>th</sup> century this led to a struggle of viewpoints, that was resolved by vortex theory.

**1.2.3. The contribution of Joukowsky and Betz to the vortex theory of propellers.** The first article of Joukowsky from his cycle *Vortex theory of the screw propeller* has been published in [1912](#). Herein he created the vortex model of a propeller based on a rotating horseshoe vortex, which expanded the elementary vortex model of a wing with a finite span. In his vortex theory each of the blades is replaced by a lifting line about which the circulation, associated with the bound vorticity, is constant, resulting in a free vortex system consisting of helical vortices with finite cores trailing from the tips of the blades and a rectilinear hub vortex, as sketched in figure [1.1a](#). In [1918](#) in the last, fourth, article of the cycle, he not only expounds the theory of an ideal propeller based on Froude's actuator disc theory but also derived the performance of a static disc. This is considered

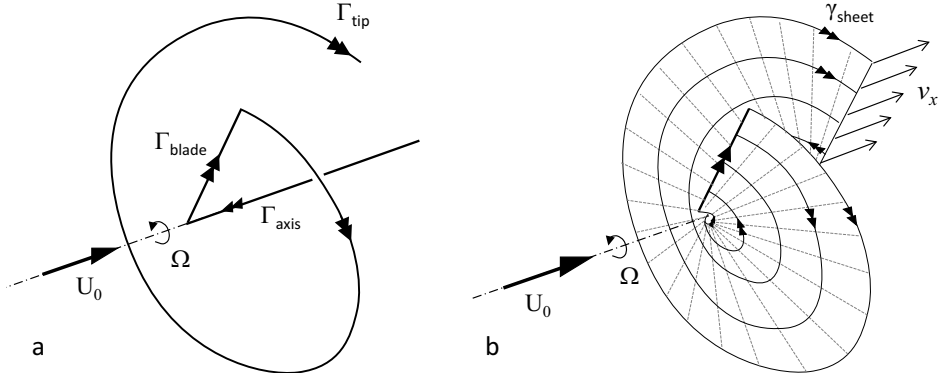


Figure 1.1: Rotor vortex models of Joukowsky, (a), and Betz, (b), for a 1-bladed propeller.

to be the very first performance prediction for a rotor. His static disc result is still valuable as a first indication for the power required to keep a helicopter or a modern drone hovering.

Simultaneously [Betz \(1919\)](#) worked on the creation of the propeller vortex theory. He proposed a model for rotors equivalent to Prandtl's model of a wing with an elliptically distributed load giving a uniform induced velocity with minimum induced drag. Each of the rotor blades is replaced by a lifting line releasing a free vortex sheet with constant velocity in axial direction, see figure 1.1b.

The models of Joukowsky and Betz are supposed to represent the ideal rotor. At the time of these pioneers it was not yet possible to evaluate which model was more ideal than the other. Both models neglected wake expansion or contraction, so were valid only for lightly loaded rotors. [Goldstein \(1929\)](#) found an analytical solution for the wake of Betz's rotor restricted to lightly loaded propellers. [Wald \(2006\)](#) pays great attention to the Goldstein solution as this is considered to be the optimal one for propellers. [Okulov et al. \(2015, chapter 4\)](#) present an overview of the development towards a complete non-linear solution to Betz's problem including wake expansion or contraction. A similar solution was published by [Wood \(2015\)](#). Both confirm the main result of Froude's analysis that the averaged axial velocity at the disc or rotor is the mean of the velocities far up- and downstream, and satisfies the results of momentum theory. Furthermore [Okulov et al. \(2015, chapter 4\)](#) show that Joukowsky rotors perform slightly better than Betz rotors for the same tip speed ratio. For the analyses in the next chapters it is relevant to know that in the limit for an infinite number of blades rotating with infinite speed, both models converge to Froude's actuator disc, so they become identical. For the Betz rotor this is shown by [Okulov and Sørensen \(2008\)](#), for the Joukowsky rotor the limit transition is presented in section 4.3.

Concluding this subsection we may say that [Joukowsky \(1912, 1914, 1915, 1918\)](#) and [Betz \(1919, 1921\)](#) have shown for the first time the connection between a real rotor and an abstract actuator disc.

**1.2.4. The Betz-Joukowsky limit for wind turbines.** Joukowsky (1920) and Betz (1920) have independently published articles to develop Froude's theory to the theory of the ideal wind turbine, predicting the maximum energy which can be extracted from wind. Munk (1920) did the same. In addition to this Hoff (1921) remarked that his article with the same topic was written somewhat later than the mentioned papers but was independent of them. Because the independent publications by Joukowsky and Betz are the result of their great achievements in vortex theory, their names are connected to this limit, see Okulov and van Kuik (2012). The maximum efficiency of an energy extracting device was known as the Joukowsky limit in Russia, and as the Betz limit in the rest of the world.

The reason why Joukowsky's name was not connected outside Russia may be explained by the following. The paper of Joukowsky (1920) had a quite special purpose: it was a response to an inventor, in which he formulated the maximum of wind energy utilization for the ideal wind turbine. The paper of Betz (1920) has a title that shows the topic clearly: *The maximum efficiency of a wind turbine*. In addition to this Betz has published the remarkable book *Wind energy and its utilization by windmills* which made the name of Betz well-known amongst wind energy engineers. Furthermore, the paper of Betz has been published in a journal, whereas the paper of Joukowsky was part of the Transactions of his scientific institute, with a possibly more limited distribution. Joukowsky was 73 in 1920 and it was his last article.

After this history has been published by Okulov and van Kuik (2012) the maximum efficiency of a wind turbine is known as the Betz-Joukowsky limit.

### 1.3. From actuator disc to rotor aerodynamics

The actuator disc is the basis for the industry standard rotor design method, the Blade Element Momentum method, BEM (see Explanations 1.2 for a brief description). There is a good reason for this, as shown in figure 1.2. The black line shows the result of Froude's momentum theory for the wind turbine mode, left part, and the propeller mode, right part. The vertical axis gives the average induced velocity at the disc, the horizontal axis the undisturbed wind speed with respect to the disc, both made dimensionless by the velocity at the static disc (representing a rotor in hover, so  $U_0 = 0$ ). This representation is well known in helicopter literature like Leishman (2006) as it is able to show the results for zero wind speed, but for the same reason only rarely used in wind turbine references, see e.g. Sørensen et al. (1998). In this branch of rotor aerodynamics figure 1.3 is used, showing the average velocity at the disc for the wind energy flow states as a function of the thrust coefficient  $C_T = T/(\frac{1}{2}\rho U_0^2 A_d)$ . Added to both graphs are results of experiments in the 80<sup>th</sup>ies of the previous century, Anderson et al. (1982), Wilmshurst et al. (1984), van Kuik (1989), more recent experiments, Leishman (2006), Medici and Alfredsson (2006), Haans et al. (2008), Parra et al. (2016) and Lignarolo et al. (2016a), and calculations found in literature from the 70<sup>th</sup>ies, Greenberg (1972), up to recent times, Sørensen et al. (1998), Spalart (2003), Rosen and Gur (2008), Mikkelsen et al. (2009), Madsen et al. (2010). The correspondence between the momentum theory and the data is quite good, except close to the static disc and close to the maximum load on a wind turbine disc. Figure 1.3 shows the engineering extension of the momentum theory for the

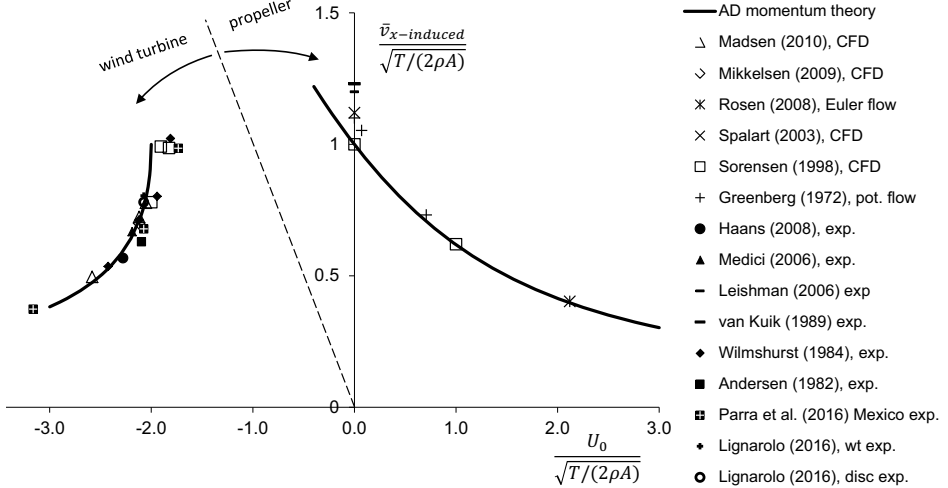


Figure 1.2: Actuator disc momentum theory compared with experiments and calculations. The vertical axis gives the induced velocity at the disc, the horizontal axis the undisturbed wind speed with respect to the disc, both made dimensionless by the velocity at the static or hovering disc at  $U_0 = 0$

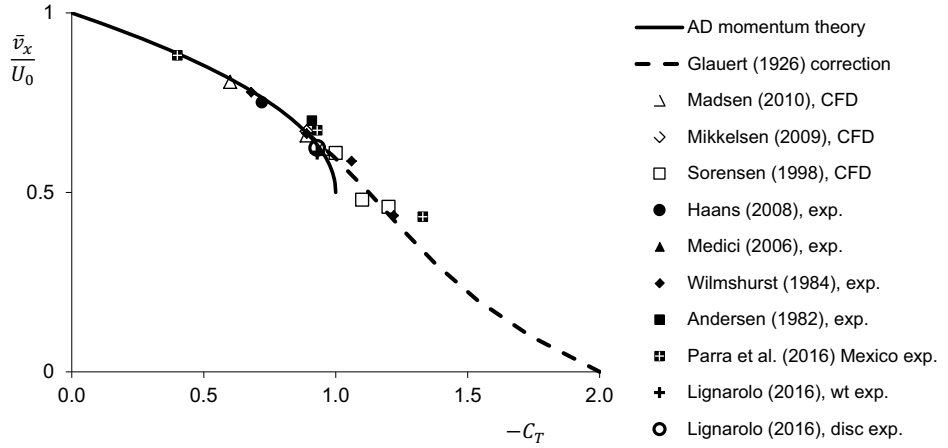


Figure 1.3: Actuator disc momentum theory including an engineering extension compared with experiments and calculations for wind turbine flow states. The vertical axis shows the velocity at the (rotor) disc, the horizontal axis the thrust coefficient.

heavily loaded disc developed by [Glauert \(1926\)](#) in the form presented by [Hansen \(2008\)](#).

The classical actuator disc momentum theory is not able to say anything about radial or azimuthal distributions of velocity and load for real rotors. The disc concept has been adapted by many as to make it useful for rotors with a finite number of blades. A major contribution was delivered by [Glauert \(1935, ch. III\)](#) who coupled disc loads to blade loads and introduced the torque in the momentum theory, resulting in the Blade Element Momentum method. One of the assumptions Glauert made to make the method executable is that the pressure in the far wake is uniform, despite the pressure gradient necessary to maintain swirl. Many authors have published similar adaptations with slightly different results, reviewed by [Sørensen \(2015\)](#). The main problems that were left after Glauert's work were the refinement of the blade model, the effect of swirl, the tip correction, the optimisation procedure and the adaptation of BEM to atmospheric and rotor conditions conditions not covered by the first versions of BEM. Much effort has been spent in making BEM suitable for real screws, propellers, helicopter and wind turbine rotors and to make it ready for digital computing, as done by [Wilson and Lissaman \(1974\)](#). For the wind energy application, models have been added for wind, wind shear, turbulence, three-dimensional flow along the blade surface, blade deformations, tip effects, yawed flow, dynamic inflow, unsteady aerofoil behaviour, dynamic stall, rotor and turbine control, etcetera. Similar adaptations and extensions have been developed for the other branches of rotor aerodynamics. Propeller, helicopter and wind energy textbooks like [Breslin and Andersen \(1994\)](#), [Leishman \(2006\)](#), [Burton et al. \(2011\)](#), [Manwell et al. \(2009\)](#), and [Schepers \(2012\)](#) present surveys of these BEM-adaptations, although improved corrections are continuously being published, e.g. by [Schaffarczyk \(2014\)](#) and [Sørensen \(2015\)](#).

Besides momentum theory also vortex theory is used to model the action of a  $B$ -bladed rotor. [Breslin and Andersen \(1994\)](#) presented, besides the actuator disc theory, a thorough treatment of the lifting line theory and propeller design optimization. [Branlard \(2017\)](#) gives a comprehensive survey of vorticity based modelling for wind turbine aerodynamics. Modern computer power has enabled vortex lattice methods like the one described by [Micallef et al. \(2013\)](#), where boundary conditions are applied at the true blade surface. The potential flow solution provides details of the wake as well as the blade loads. Full solutions including viscous effects using Computational Fluid Dynamics (CFD) are presented in early publications like [Sørensen and Myken \(1992\)](#) and [Madsen and Paulsen \(1990\)](#), and more recent publications like [Madsen et al. \(2010\)](#), [Sibuet Watters et al. \(2010\)](#) and [Troldborg et al. \(2010\)](#). Since the calculation time required for a complete solution of blade and wake flow is still too long, the blade is often represented by an actuator line as first proposed by [Sørensen and Shen \(2002\)](#). In the actuator line method the blade is represented by a prescribed load distributed along a line replacing the blade, see e.g. [Shives and Crawford \(2013\)](#) and [Réthoré et al. \(2014\)](#). This method is very successful in wake analyses where details of the flow around the blade cross section are not very relevant. Specially in the combination with atmospheric turbulence, rotor generated turbulence, interaction between multiple wakes and intervention by rotor control actions, methods

based on the actuator line, disc or surface are the method of choice. A survey of CFD methods in wind energy is published by [Sanderse \(2011\)](#).

Despite the progress in blade aerodynamics, the actuator disc has received and still receives continuous attention. [Wu \(1962\)](#) has derived a differential equation describing the flow in terms of the stream function, the circulation around the axis and the component of the disc load perpendicular to the stream tube. When the disc has a uniform normal load, the wake is bounded by a vortex sheet and the flow inside the wake is free of vorticity. This enables rewriting Wu's equation as a potential flow equation, with the position and strength of the vortex sheet as unknowns to be solved by numerical methods. [Greenberg \(1972\)](#) has published results for such a uniformly loaded disc. [Øye \(1990\)](#) and [Mikkelsen et al. \(2009\)](#) represented the vortex sheet emanating from the edge of a uniformly loaded disc by a series of concentric vortex rings. The strength and position of these rings is calculated with the appropriate boundary conditions. Several authors, amongst which [Sørensen and van Kuik \(2011\)](#), have presented an extension to Glauert's theory for rotating disc force fields including torque when the rotational speed tends to zero. [Conway \(1998\)](#) has presented exact analytical solutions for non-uniform load distributions in inviscid flow. His results have become a benchmark to test other flow solvers. [Rosen and Gur \(2008\)](#) developed a semi-analytical actuator disc model, in which the disc is represented by a distribution of sinks. They found a close correspondence with Conway's results. [Réthoré et al. \(2014\)](#) used Conway's work to successfully validate a CFD actuator disc method. A first CFD calculation for many actuator disc flow states is presented by [Sørensen et al. \(1998\)](#). An example of the calculation of the hover flow state is published by [Spalart \(2003\)](#).

This brief representation of the state-of-the-art in rotor aerodynamics shows that it has a long history with a well developed foundation in analytical theory, vorticity modelling and CFD calculations, and with BEM as well validated design method. The research area Rotor Aerodynamics is much wider than treated in this book. Especially for wind turbine aerodynamics the following references may help the interested reader to get acquainted: [Sørensen and Shen \(2002\)](#) for the first application of an actuator line, [Calaf et al. \(2010\)](#) for a Large Eddy Simulation (LES) study of wind turbine array boundary layers, [Churchfield et al. \(2012\)](#) for a LES study of wind plant aerodynamics, [Porté-Agel et al. \(2011\)](#) for a LES study of atmospheric boundary layer flow through a wind farm, [Schepers \(2012\)](#) for a survey of engineering models, [Hölling et al. \(2014\)](#) for the impact of turbulence, [Fleming et al. \(2015\)](#) for a comparison of wake mitigation control strategies, [Simão Ferreira \(2009\)](#) for the aerodynamics of vertical axis wind turbines, [Stevens and Meneveau \(2017\)](#) for a review of flow phenomena and models in wind turbine wakes and wind farms interacting with the earth boundary layer, and finally [van Kuik et al. \(2016, section 2,3\)](#) where long term research questions on aerodynamic, wind and turbulence issues are reviewed.

### EXPLANATION 1.2. BEM, the Blade Element Momentum method

In its most elementary form, BEM proceeds from a rotor placed in a uniform, undisturbed, parallel flow aligned with the rotor axis. The Momentum part uses the actuator disc momentum theory, see section 5.2, to find the induction at the position of the rotor. However, instead of doing so for the entire rotor disc, it is done for each radial element  $\Delta r$  of the rotor blades. The corresponding annulus contains the flow from far upstream to far downstream passing through the rotor in between the radii of the blade element. It is known that applying the disc momentum theory to annuli instead of the stream tube is not valid, but still it is used as the error is assumed to be limited, except close to the tip where all BEM codes apply a tip correction to modify the axial velocity and local load. The Momentum part of BEM requires the blade load as input. This is taken from the Blade Element part where 2-D aerofoil properties are used to determine lift and drag for a given axial induction. Both parts are solved iteratively. Based on the assumption of independent annuli, [Burton et al. \(2011, page 70\)](#) shows that the Joukowsky distribution of uniform circulation (see Explanation 3.1) results from BEM based rotor design optimisation. However, the independence of annuli is not correct, as will be discussed and quantified in chapters 5 and 6.

## 1.4. Why this book?

The fluid dynamic basis of rotor aerodynamics is revisited with emphasis on the first rotor model, the actuator disc. Three approaches characterize the analysis:

- in most fluid dynamic analyses the flow induced by lifting surfaces is solved using boundary conditions at the surface, with the resulting load on the surface as output. In doing so, the force field term in the equation of motion is absent. However, the equation of motion allows using a force field as input instead of output, with the force field determining the flow. In contrast to many other fields of fluid dynamics, this is common practice in most rotor aerodynamic models, so this approach is adopted here. This leads to relations between force fields and (conversion of) vorticity or energy which are underexposed in modern fluid dynamic textbooks.
- the actuator disc is supposed to represent a real rotor sufficiently accurate. The relation between a disc and a rotor is investigated analytically and numerically, and the respective flow fields measured in a wind tunnel are compared.
- using modern computer power, it has become possible to show several details of actuator disc flows which could not be determined by the pioneers in rotor aerodynamics. This numerical approach uses the same equations of motion as used by them: the inviscid, incompressible Euler equations.

The questions which are addressed are listed below. Several of these questions lead to improved understanding, others to improved rotor modelling:

- Q1 Most aerodynamic models calculate the load on a lifting body by integration of the pressure at a surface after the flow is solved: the load is output. In many rotor aerodynamic models the reverse method is used, with the load as input and the flow field as output. Are these approaches consistent and what are the benefits and drawbacks of the force field method?
- Q2 In solid mechanics it is useful to classify forces as conservative or non-conservative. Is this a relevant distinction in the force field method?
- Q3 It seems obvious to interpret Bernoulli's law as conservation of energy, but fluid dynamic textbooks are very cautious to do so. Is it possible to show that conservative forces conserve  $H$ , the Bernoulli parameter, and non-conservative forces change  $H$ ? If so, can pressure be interpreted as potential energy?
- Q4 Textbooks learn that lifting surfaces like wings and rotor blades, when modelled as a bound vortex, form a closed vortex system with the trailing vortices: vorticity and circulation are conserved, often explained by Helmholtz's conservation laws. However, the most simple rotor representation, the actuator disc, produces vorticity instead of conserving it. Are both approaches compatible?
- Q5 Physical intuition as well as numerical examples show that a rotor subjected to the limit  $B \rightarrow \infty$ ,  $B$  being the number of blades, becomes the actuator disc. Can we show this analytically?
- Q6 How close does the velocity field of an actuator disc resemble the velocity field of a rotor? In more detail: can we use the velocity distribution at the disc to represent the velocity distribution at the position of the rotor blade?
- Q7 Actuator disc momentum theory does not provide detailed results like the distribution of vorticity along the wake boundary. This boundary is a cylindrical vortex sheet with its leading edge coinciding with the disc edge. Leading edges of vortex sheets are known to be singular in the vorticity strength. Can modern computations be used to investigate the leading edge behaviour of this vortex sheet?
- Q8 The actuator disc momentum theory gives the average velocity at the disc. Can we say something about the radial distribution of the velocity?
- Q9 It is known that the actuator disc momentum theory can not be applied per stream annulus instead of the entire stream tube. Is it possible to modify the theory to become a useful prediction method per annulus?
- Q10 Some actuator disc momentum theories including swirl have a remarkable result for energy extracting discs with a rotational speed approaching zero: the efficiency becomes infinite. This is not physically acceptable. What goes wrong in the theory?
- Q11 The wake behind a disc or rotor with finite rotational speed includes an azimuthal velocity  $v_\varphi$ . Some publications consider this to be a loss of energy. Is this true?
- Q12 What are the main differences between actuator disc flows extracting energy and adding energy, apart from wake expansion versus contraction?

- Q13 Several experiments on wind turbine model rotors show that the tip vortex first moves inboard, so to a lower radius, before the wake expansion starts. What is the explanation?
- Q14 Joukowsky's model for an optimal rotor with a finite number of blades has uniform circulation along the radius while the model of Betz for such a rotor has a non-uniform circulation. The tip correction used in BEM has been formulated by Prandtl using Betz's model. Is it correct to apply a tip correction derived for Betz's concept in BEM calculations based on Joukowsky's concept?

Each of the next chapters ends with a section Evaluation, in which the answers to these questions will be summarized. Only actuator discs representing rotors operating in unbounded fluid are considered. Discs used to model devices in flows that are restricted laterally by walls, e.g. tubes, cascade disc flows and disc flows through flame fronts, are treated by [Horlock \(1978\)](#).

This page intentionally left blank

## Force fields in fluid dynamics

### 2.1. Introduction

Rotor aerodynamics is one of the few areas in aerodynamics where force fields are used as input in flow calculations: the flow field induced by predefined forces is solved (the dynamic method). In most other aerodynamic analyses the force field is the output instead of input: the flow field around a surface is solved using surface boundary conditions, after which the pressure and so the load are known (the kinematic method). One of the reasons why force fields as input are not used often is twofold: usually they are not known in advance, and the kinematic method for which Lanchester, Prandtl and Joukowsky laid the basis, has been shown to be very powerful. However, the use of force fields has some advantages, especially for rotor aerodynamics since the thrust, being the integrated load, is the main parameter defining flow states. The use of force fields as input is common practice in classical actuator disc theory, in the Momentum part of BEM methods, and in actuator line (AL) analyses. In the AL analyses the blade is replaced by a load carrying line in order to have a much lower computation time compared to full Computational Fluid Dynamics (CFD) solutions. The load in these methods is determined either by the definition of the problem (in actuator disc analyses: based on physical arguments a load distribution is assumed, e.g. [Sørensen et al. \(1998\)](#)) or by iteration with other methods (in AL and momentum methods: for a given flow field the load is taken from a Blade Element calculation, e.g. [Shen et al. \(2014\)](#)). Besides its modest computational effort, the force field approach offers the advantage of a force-field based interpretation of the three processes governing disc and rotor flows: the change of momentum, the generation or conservation of vorticity and the conversion or conservation of energy.

Before discussing these processes we treat the role of the force field term in the Euler equation of motion, involving a distinction between conservative and non-conservative force fields. Furthermore we show that the kinematic approach (no force field, boundary condition of zero normal velocity at the lifting surface) and the dynamic approach (external force fields) are equivalent.

### 2.2. The equation of motion and the coordinate systems

The flow is assumed to be incompressible, inviscid and isentropic, so the Euler equation:

$$\rho \frac{\partial \mathbf{v}}{\partial t} + \rho (\mathbf{v} \cdot \nabla) \mathbf{v} = -\nabla p + \mathbf{f} \quad (2.1)$$

is valid as well as the continuity equation:

$$\nabla \cdot \mathbf{v} = 0, \quad (2.2)$$

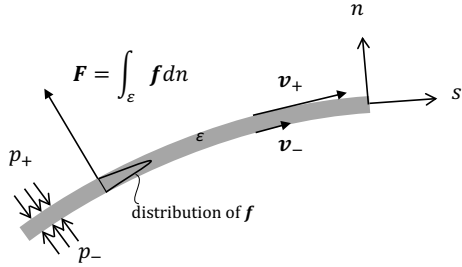


Figure 2.1: Properties of a bound vortex sheet with thickness  $\epsilon$  and force density distribution  $\mathbf{f}$ : pressure jump  $p_- - p_+ = F_n$ , velocity jump  $v_- - v_+ = \gamma$ .

with  $\mathbf{v}$  being the velocity vector,  $\rho$  the flow density,  $p$  the pressure and  $\mathbf{f}$  the force density, volume force or force field. Rewriting (2.1) with the vector identity  $(\mathbf{v} \cdot \nabla) \mathbf{v} = \nabla(\mathbf{v} \cdot \mathbf{v})/2 - \mathbf{v} \times \boldsymbol{\omega}$  yields:

$$\nabla H = \mathbf{f} - \rho \frac{\partial \mathbf{v}}{\partial t} + \rho \mathbf{v} \times \boldsymbol{\omega}, \quad (2.3)$$

where  $H$  is the Bernoulli constant  $p + \frac{1}{2}\rho \mathbf{v} \cdot \mathbf{v}$ , and  $\boldsymbol{\omega}$  the vorticity. Most textbooks pay some attention to the force term but at some moment assume that  $\mathbf{f}$  is conservative, like the gravity force field  $\rho \mathbf{g}$ . Then  $\mathbf{f} = \rho \mathbf{g} = -\nabla \mathcal{G}$  where  $\mathcal{G}$  is the potential of  $\rho \mathbf{g}$ . The right-hand side of (2.1) then becomes  $-\nabla(p + \mathcal{G})$ . With the potential  $\mathcal{G}$  considered to be part of the pressure, the conservative  $\mathbf{f}$  disappears from the equation of motion. Here this assumption is not made. Instead, force fields are assumed to be confined to thin surfaces having thickness  $\epsilon$ , see figure 2.1. Integration of  $\mathbf{f}$  along the normal  $n$ , becoming a Dirac delta function for  $\epsilon \rightarrow 0$ , gives the surface load  $\mathbf{F}$ :

$$\mathbf{F} = \int_{\epsilon} \mathbf{f} dn. \quad (2.4)$$

More integrations result in a line force or a discrete force, which will be named after its function, e.g. lift or thrust.

Most analyses in this book use the cylindrical coordinate system  $(x, r, \varphi)$  with the disc centreline coinciding with the positive  $x$ -axis and with  $\mathbf{e}$  denoting the unit vector with an appropriate index, as well as the local coordinate system  $(s, n, \varphi)$ , see figure 2.2. The coordinates  $s$  and  $n$  are in the meridian plane tangent respectively normal to a streamline. Besides these inertial coordinate systems also the rotating system  $(x, r, \varphi)_{rot}$  is used, rotating with respect to the inertial system with the angular velocity  $\Omega$  of the force field. The velocity and vorticity in the inertial and rotating systems are related by:

$$\mathbf{v}_{rot} = \mathbf{v} - \mathbf{e}_\varphi \Omega r \quad (2.5)$$

$$\boldsymbol{\omega}_{rot} = \boldsymbol{\omega} - 2\mathbf{e}_x \Omega. \quad (2.6)$$

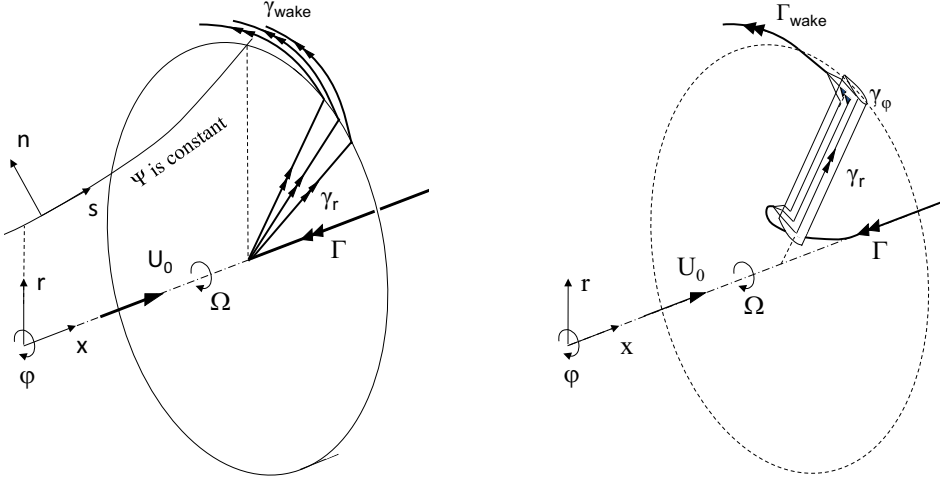


Figure 2.2: The coordinate systems of an actuator disc and rotor acting as a wind turbine.  $\Psi$  is the Stokes stream function. All vectors are in positive direction except  $\Gamma_{axis}$  and  $\gamma_\varphi$ . Shown are the flow states decelerating the flow.

Batchelor (1970, eq. (3.5.20))<sup>1</sup>, gives the steady Euler equation in the rotating coordinate system, including the centrifugal force  $-\boldsymbol{\Omega} \times (\boldsymbol{\Omega} \times \mathbf{r}) = \mathbf{e}_r \Omega^2 r = \frac{1}{2} \nabla (\Omega r)^2$  and Coriolis force  $\mathbf{v}_{rot} \times 2\boldsymbol{\Omega}$ :

$$\mathbf{f} + \frac{\rho}{2} \nabla (\Omega r)^2 + \rho \mathbf{v}_{rot} \times 2\boldsymbol{\Omega} = \nabla H_{rot} - \rho \mathbf{v}_{rot} \times \boldsymbol{\omega}_{rot}. \quad (2.7)$$

With (2.6) and with  $\nabla H_{rot} = \nabla \left( H - \rho v_\varphi \Omega r + \frac{\rho}{2} (\Omega r)^2 \right)$  this becomes:

$$\mathbf{f} = \nabla (H - \rho v_\varphi \Omega r) - \rho \mathbf{v}_{rot} \times \boldsymbol{\omega} \quad \text{for steady flows.} \quad (2.8)$$

### 2.3. Equivalence of the kinematic and dynamic methods

Prandtl (1918) showed that the pressure distribution acting on a translating lifting surface is equivalent to a distribution of normal forces acting on the surface modelled as a bound vortex sheet  $\gamma$ . The line of thoughts is the following: In the kinematic method usually the space occupied by a body is excluded from the flow domain, with appropriate boundary conditions like zero normal velocity applied at the surface. The flow and pressure around it are determined by solving  $\rho \frac{\partial \mathbf{v}}{\partial t} + \rho (\mathbf{v} \cdot \nabla) \mathbf{v} = -\nabla p$  resulting in the pressure acting at the surface. In the force field approach this exclusion of the body volume is not made, but the surface  $S$  is considered as a layer of infinitely thin thickness  $\epsilon$ , at which a normal force field  $\mathbf{f}$  is distributed. After integration across  $\epsilon$  the force term becomes  $\mathbf{F}$  defined

---

<sup>1</sup>Batchelor's equation is without  $\mathbf{f}$ . He has included the centrifugal term  $\frac{1}{2} \nabla (\Omega r)^2$  in  $\nabla H$ .

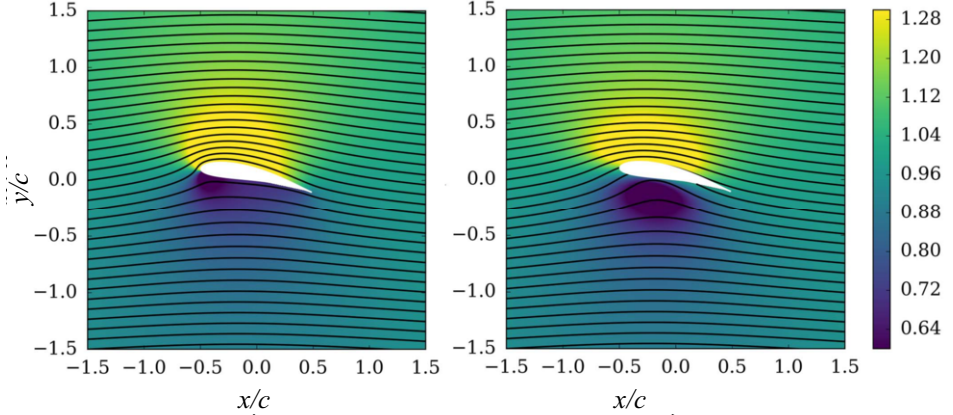


Figure 2.3: Comparison of the flow around a Joukowsky aerofoil. Left: the analytical solution, right: the numerical solution with the lift as input, copied with permission from [Martínez-Tossas et al. \(2017\)](#)

by (2.4) with  $\mathbf{f}$  behaving as a Dirac delta function for  $\epsilon \rightarrow 0$ . Integration of (2.3) across  $\epsilon$  gives:

$$\mathbf{F} = \lim_{\epsilon \rightarrow 0} \int_{\epsilon} (\nabla H - \rho \mathbf{v} \times \boldsymbol{\omega}) dn, \quad (2.9)$$

in which the unsteady term is absent as  $\mathbf{F} \perp \mathbf{v}$ . In the limit  $\epsilon \rightarrow 0$  the first term in the integrand results in a jump in  $H$ , while the second term becomes  $\int (-\rho v_s \frac{\partial v_s}{\partial n}) dn_\epsilon = \frac{1}{2} \rho (v_-^2 - v_+^2)$  with the subscripts + and - explained in figure 2.1. Herewith:

$$\mathbf{F} = e_n \Delta H - \rho \bar{\mathbf{v}} \times \boldsymbol{\gamma} \quad (2.10)$$

in which  $\bar{\mathbf{v}}$  is the average of the velocity on both sides of the vortex sheet and  $\boldsymbol{\gamma}$  is the vortex sheet strength:

$$\boldsymbol{\gamma} = \int_{\epsilon} \boldsymbol{\omega} dn = -e_\phi \Delta v_s. \quad (2.11)$$

Equation (2.10) shows that every vortex sheet having a non-zero velocity experiences a jump in Bernoulli parameter  $H$  or carries a normal load  $F$ . In case  $\Delta H = 0$  the famous Kutta-Joukowsky relation for the load on a vortex sheet results. If the sheet is the surface of an aerofoil contour, the pressure and velocity inside the aerofoil are constant, so  $\Delta H = \text{constant}$ , by which (2.10) gives for the lift on a 2 D aerofoil:

$$\mathbf{L}_{2-D} = \oint \mathbf{F} ds = -\rho \oint \bar{\mathbf{v}} \times \boldsymbol{\gamma} ds \quad (2.12)$$

with  $s$  following the contour of the aerofoil. As:

$$\mathbf{F} = -\rho \bar{\mathbf{v}} \times \boldsymbol{\gamma} = -e_n \Delta \left( \frac{1}{2} \rho v_s^2 \right) = e_n \Delta p \quad (2.13)$$

this becomes:

$$\mathbf{L}_{2-D} = \oint \mathbf{F} ds = \rho \oint \mathbf{e}_n p ds. \quad (2.14)$$

This shows the equivalence of the force field  $\mathbf{F}$  and the pressure  $\mathbf{e}_n p$ .

Besides showing the equivalence in equations, it is worthwhile to see some numerical implementations. The modelling of the force field  $\mathbf{F}$  in CFD methods requires a distribution of  $\mathbf{f}$  on a number of grid cells, satisfying (2.4), see for example [Martínez-Tossas et al. \(2017\)](#). He demonstrates the equivalence of the kinematic method and a numerically implemented dynamic method for a two-dimensional aerofoil flow. The left side of figure 2.3 shows the analytically resolved potential flow around a cambered Joukowsky aerofoil at 12° angle of attack, where the right side gives the flow induced by the Joukowsky lift for the same aerofoil. The flow is solved with a linearised equation of motion and the lift is approximated by an elliptic Gaussian distribution of which the centre is at the chord of the aerofoil. The position of the centre and the length parameters in the direction of the chord and thickness are optimized for a best fit with the analytical solution. Despite these approximations the flow field at 1 chord distance from the quarter chord point is almost identical for both methods as it follows the  $r^{-1}$  behaviour for a potential vortex. This example shows the pros and cons of the dynamic method: one has to know important information from the aerofoil such as the lift coefficient before running a CFD simulation, but if so, it allows an accurate calculation of the flow field without the need to resolve all aerofoil flow details.

A second example of the equivalence is shown in figure 2.4, where the axial velocity in the rotor plane of a 3 bladed rotor with constant bound circulation is shown, calculated by a lifting line (LL) method and an actuator line (AL) method as reported in [van Kuik et al. \(2015b\)](#). The LL method is the kinematic method: the blade is modelled as a line with prescribed constant bound circulation  $\Gamma$ . The AL method prescribes forces acting at the line. The force distribution is chosen such that the resulting circulation around the lines is identical to the prescribed constant circulation in the LL method. The load case shown is the wind turbine for tip speed ratio  $\lambda = 7$  where  $\lambda$  is the tip speed  $\Omega R$  divided by the wind speed  $U_0$ , for the thrust coefficient  $C_T = T / (\frac{1}{2} \rho U_0^2 \pi R^2) = -8/9$ . The results of both methods agree reasonably well except for minor differences for  $r < 0.1R$  and near the tip, due to differences in the desingularisation of the vortices. In section 4.4 both methods will be used to compare actuator disc and rotor flows.

## 2.4. Conservative and non-conservative force fields

The use of the force field  $\mathbf{f}$  is discussed in old text books and papers, like [Prandtl \(1918\)](#) and [von Kármán and Burgers \(1935\)](#) without making an explicit distinction between conservative and non-conservative components. In general, the force field can have both components:

A non-conservative force field is defined by:

$$\nabla \times \mathbf{f} \neq 0, \quad (2.15)$$

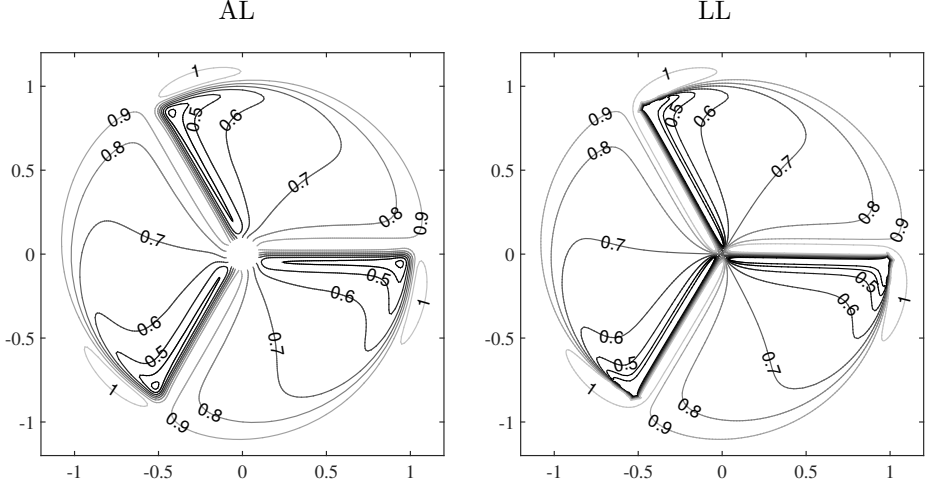


Figure 2.4: Distribution of  $v_x/U_0$  at the rotor plane  $x=0$  according to the actuator line (AL), and lifting line (LL) model, for  $\lambda = 7$  and  $C_T = -8/9$ , from [van Kuik et al. \(2015b\)](#). The direction of rotation is anti-clockwise

and is able to generate vorticity as shown by the curl of (2.3) (see [Saffman, 1992](#), pp. 10-11):

$$\frac{1}{\rho} \nabla \times \mathbf{f} = \frac{D\omega}{Dt} - (\boldsymbol{\omega} \cdot \nabla) \mathbf{v}, \quad (2.16)$$

with the last term denoting the change of vorticity due to stretching or tilting of already existing vortex filaments. When  $\mathbf{f}$  is distributed on a surface with thickness  $\epsilon$  as shown in figure 2.1, integration of  $\nabla \times \mathbf{f}$  and taking the limit for  $\epsilon \rightarrow 0$  gives:

$$\frac{1}{\rho} \nabla \times \mathbf{F} = \frac{D\gamma}{Dt} - (\boldsymbol{\gamma} \cdot \nabla) \mathbf{v}. \quad (2.17)$$

For inviscid flow around a 2-D aerofoil  $\oint \nabla \times \mathbf{F} ds = 0$  with  $s$  taken along the aerofoil contour, so the force field is conservative and no vorticity is produced. For a finite wing  $\oint \nabla \times \mathbf{F} ds \neq 0$  because of the spanwise gradient of the load. The force field of a 3-D lifting surface is non-conservative, producing trailing vorticity according to (2.17). However, when integrated over the entire surface  $S$  of a wing or rotor blade:

$$\oint_S \nabla \times \mathbf{F} dS = 0, \quad (2.18)$$

since the integrand consists of the derivatives of the normal load in spanwise direction, yielding 0 after integration on a closed contour. The force field of a lifting surface generates vorticity locally, but as an equal amount of opposite sign is produced somewhere else at the surface, the nett generation is zero. This is the force field based explanation of the fact that any lifting surface produces the same amount of positive and negative vorticity.

Since the generation of vorticity implies that fluid particles receive an angular speed, it is expected that (2.16) represents the differential balance of angular momentum. The Euler equation possesses a number of conserved quantities like the angular- or moment of momentum, as shown by e.g. Marshall (2001, p.50). However, an explicit relation between this balance and force fields is not found in literature. In appendix B it is shown that  $\nabla \times \mathbf{f}$  expresses, in differential form, the torque applied to a fluid element and similarly that (2.16) is the balance of angular momentum. The analysis is restricted to 2 – D and 3 – D axisymmetric flows without swirl.

A conservative force field satisfies  $\nabla \times \mathbf{f} = 0$  or, equivalently:

$$\mathbf{f} = -\nabla \mathcal{F} \quad (2.19)$$

where  $\mathcal{F}$  is the potential of  $\mathbf{f}$ . With (2.19) the Euler equation (2.1) becomes:

$$\rho \frac{\partial \mathbf{v}}{\partial t} + \rho (\mathbf{v} \cdot \nabla) \mathbf{v} = -\nabla (p^* + \mathcal{F}) = -\nabla p, \quad (2.20)$$

with  $p = p^* + \mathcal{F}$  where  $p^*$  indicates the pressure in absence of  $\mathcal{F}$ . When only conservative forces act, the flow is free of vorticity so  $\mathbf{v}$  can be expressed in its potential  $\Phi$ ,  $\mathbf{v} = \nabla \Phi$ . Analogous to (2.3) the unsteady Bernoulli equation follows:

$$\nabla \left( H + \rho \frac{\partial \Phi}{\partial t} \right) = 0 \text{ for } \mathbf{f} = \mathbf{f}_{cons}. \quad (2.21)$$

with  $H = H^* + \mathcal{F}$ . This can be compared with the Bernoulli equation derived from (2.8) for flows without a force field and free of vorticity:

$$\nabla (H - \rho v_\varphi \Omega r) = 0, \quad (2.22)$$

which has been derived previously by Thwaites (1960, p. 473) and de Vries (1979, app. C2). A comparison shows that in the wake of a rotor or disc, where  $\nabla \mathcal{F} = 0$ ,

$$\frac{\partial \Phi}{\partial t} = -v_\phi \Omega r \text{ in the wake where } \boldsymbol{\omega} = 0. \quad (2.23)$$

Equation (2.20) also shows that the effect of a conservative  $\mathbf{f}$  is to change the pressure field. According to (2.21) a conservative force acting in a steady flow conserves  $H = p + \frac{\rho}{2} |\mathbf{v}|^2$ , so changing  $p$  implies changing  $\frac{\rho}{2} |\mathbf{v}|^2$ , positioning  $p$  in the role of potential energy. This is examined further in section 2.5.

## 2.5. Force fields and energy

**2.5.1. Work done by force fields.** Batchelor (1970, p. 157) shows that the work per volume per second done by a distribution of volume forces is given by the dot product  $\mathbf{f} \cdot \mathbf{v}$ . This is evaluated using (2.3), integrated on volume  $V$  with surface  $S$  encompassing the area at which  $\mathbf{f}$  is distributed. With  $\mathbf{e}_{n,S}$  as the unit vector normal to  $S$  and using Gauss's theorem this gives:

$$\begin{aligned} \int_V \mathbf{f} \cdot \mathbf{v} dV &= \int_V \frac{\rho}{2} \frac{\partial |\mathbf{v}|^2}{\partial t} dV + \int_V (\mathbf{v} \cdot \nabla) H dV \\ &= \int_V \frac{\rho}{2} \frac{\partial |\mathbf{v}|^2}{\partial t} dV + \int_S H (\mathbf{v} \cdot \mathbf{e}_{n,S}) dS. \end{aligned} \quad (2.24)$$

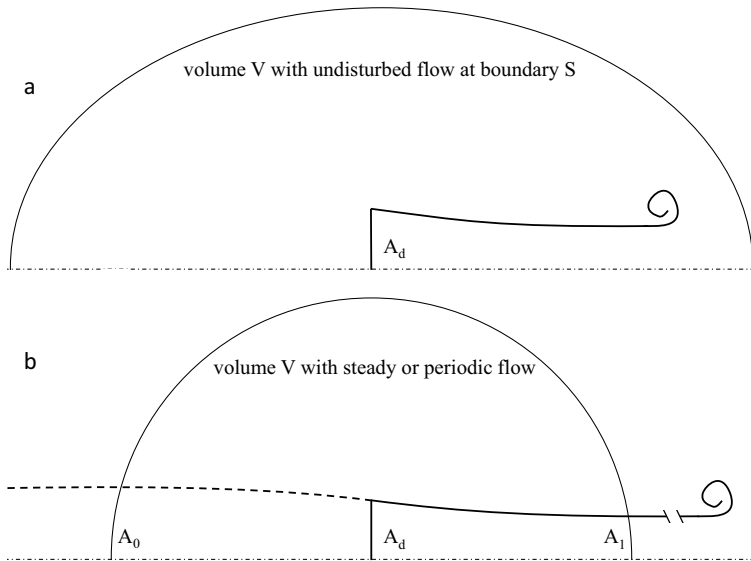


Figure 2.5: Control volume  $V$  used to assess the power converted by the disc: (a) is the volume extending to infinity encompassing the start vortex, (b) is the volume containing steady flow as the start vortex is far enough outside  $V$  to have no influence at the flow inside  $V$ .

The choice of the volume  $V$  determines which of the terms at the right-hand side contribute. Figure 2.5 shows the wake of an energy adding disc with two versions of  $V$ . In figure 2.5a  $V$  is large enough to encompass the wake including the start vortex which is convected downstream. The flow within  $V$  is unsteady, but at the surface  $S$  the flow and pressure are undisturbed. Figure 2.5b shows the volume in which the flow is steady.  $V$  is large enough to include a fully developed wake. Furthermore the stream tube passing through the disc is displayed, with the subscript 0 to indicate the undisturbed flow, subscript 1 for the fully developed wake, and subscript  $d$  for the disc itself. If the force field starts to work at a certain time and  $V$  is taken so large that at  $S$  the velocity and pressure remain undisturbed, figure 2.5a applies, and the second integral at the right-hand side of (2.24) is 0. The work done is expressed as the increase per second in kinetic energy contained within  $V$ :

$$\int_V \mathbf{f} \cdot \mathbf{v} dV = \int_V \frac{\rho}{2} \frac{\partial |\mathbf{v}|^2}{\partial t} dV \text{ when control volume } V \text{ extends to infinity.} \quad (2.25)$$

This holds for force fields representing wings or rotors when an inertial frame of reference is used, and  $V$  is sufficiently large to encompass the entire wake behind these lifting surface after the start.

In case  $V$  is chosen smaller such that  $S$  crosses the fully developed wake, figure 2.5b applies, so the unsteady integrand may be either zero (for the steady actuator disc) or periodic (for the rotor), yielding a zero result after integration

over time  $\Delta t$  required for 1 revolution of the force field. The work done per second is:

$$\int_V \mathbf{f} \cdot \mathbf{v} dV = \int_S H (\mathbf{v} \cdot \mathbf{e}_{n,S}) dS \text{ for steady or periodic flows, finite } V, \quad (2.26)$$

so is expressed in the flux of flow times  $H$ , where  $H$  is the energy level of the fluid particles.

**2.5.2. Choice of reference system.** The use of (2.25) implies that an inertial reference system is used, with  $V$  extending to infinity. To use (2.26) the reference system need to be fixed to the position of the force field in order to achieve steady or periodic flow within  $V$ , with  $V$  having finite dimensions. In case (2.26) is used it is important to check where and how the work is done. Let us consider a force field representing the action of a wing. The force field experiences a non-zero undisturbed velocity  $\mathbf{U}$  far upstream. At the wing surface the velocity  $\mathbf{v}$  is tangent to the surface while the force  $\mathbf{F}$  is perpendicular, so the wing load does *not* perform work as  $\mathbf{F} \cdot \mathbf{v} = 0$ . This situation is not an invented case, as this is what happens in wind tunnel tests: the energy required to maintain the flow against the induced drag is delivered by the wind tunnel fan. Consequently, for the energy balance  $V$  should be chosen large enough to include the force field of this fan. For a wing flying in a reference frame fixed to the earth (2.25) applies: the wing has a velocity  $\mathbf{U}$  in unbounded air which is undisturbed at infinite distance from the wing. The flow vector at the surface is  $\mathbf{v} - \mathbf{U}$  and the work done by the force field is (the integrated value of)  $\mathbf{F} \cdot \mathbf{U}$ , to be delivered by the wing engines. As the amount of work to be delivered by either the wing force field, (2.25), or the fan force field, (2.26), is the same, the right-hand side of (2.26) is conveniently used to assess the work required to keep a wing flying.

Comparison of the performance of a rotor in a (non-rotating) coordinate system fixed to the axis with the performance of a rotor moving in an inertial system reveals a remarkable difference, as already noted by Betz (1920). Represented as an actuator disc, it is clear that in both systems  $\mathbf{F} \cdot \mathbf{v} \neq 0$ . The power extracted by a wind turbine fixed to earth is calculated as  $\mathbf{T} \cdot \bar{\mathbf{v}}$  where  $\mathbf{T}$  is the thrust acting against the wind speed  $\mathbf{U}_0$  and  $\bar{\mathbf{v}}$  the averaged wind speed at the disc, with  $\bar{\mathbf{v}} < \mathbf{U}_0$ . When the same wind turbine is mounted on an aeroplane having flying speed  $\mathbf{U}_0$  in still air, the power required to overcome the turbine thrust is  $\mathbf{T} \cdot \mathbf{U}_0$ . According to Corten (2001b) the difference  $\mathbf{T} \cdot (\bar{\mathbf{v}} - \mathbf{U}_0)$  is the kinetic energy dissipated into heat in the flow outside of the stream tube passing the disc. He derives this result by including in his analysis the mixing of the wake with the flow outside the wake, resulting in a vanishing slipstream at a large downstream distance. As mixing and dissipation are processes not governed by the Euler equations, these phenomena remain outside the scope of this book.

Relevant for the present analysis is the comparison of the performance in a co-rotating reference frame fixed to the axis (and blades), with the performance in a similar but stationary system. In a reference system fixed to the blades the blade force field does not perform work as at the blade surface the velocity  $\mathbf{v}_{co-rotating}$  is perpendicular to the force  $\mathbf{F}$ , similar to the wing force field in the wing-fixed system. If the rotor reference system is a non-rotating system fixed to the rotor centre, the work done by the rotor is the torque times rotational speed.

From (2.25) we know that ultimately all work done is expressed in a change of kinetic energy. The contribution by conservative forces is evaluated using (2.1) and (2.3):

$$\mathbf{f} \cdot \mathbf{v} = \rho \mathbf{v} \cdot \frac{D\mathbf{v}}{Dt} + (\mathbf{v} \cdot \nabla) p. \quad (2.27)$$

Adapting the analysis in [Marshall \(2001, p. 102\)](#) for flows being at rest at infinity, to flows which are undisturbed at infinity, submission of  $\mathbf{f} = -\nabla \mathcal{F}$  yields for the change in kinetic energy  $KE$  within  $V$ :

$$\begin{aligned} \frac{dKE}{dt} \Big|_{f_{cons}} &= \int_V \mathbf{v} \cdot \frac{D\mathbf{v}}{Dt} dV = -\frac{1}{\rho} \int_V (\mathbf{v} \cdot \nabla) (p + \mathcal{F}) dV \\ &= -\frac{1}{\rho} \int_S (p + \mathcal{F}) \mathbf{v} \cdot \mathbf{e}_{n,S} dS. \end{aligned} \quad (2.28)$$

As we consider only force distributions originating from body forces on volumes with finite dimensions,  $(p + \mathcal{F}) \rightarrow p_0$  for infinitely large  $V$ , so:

$$\frac{dKE}{dt} \Big|_{f_{cons}} = -\frac{(p + \mathcal{F})}{\rho} \int_S \mathbf{v} \cdot \mathbf{e}_n dS = 0 \text{ for flows undisturbed at infinity.} \quad (2.29)$$

This shows that conservative forces can not perform work. Then, from the left-hand side of (2.27) it follows that  $\mathbf{f}_{cons} \cdot \mathbf{v} = 0$ , so conservative forces are perpendicular to the local velocity vector. If a force field performs work, it is non-conservative.

**2.5.3. Pressure as a conservative force in momentum balances.** A special class of conservative forces appears in momentum balances. When this momentum balance is drawn on a certain control volume, the pressure at the boundaries of the volume have to be included in the balance. For the flow in the control volume, the pressure acts as a force field normal to the boundary of the control volume:

$$\mathbf{F} = -\mathbf{e}_n(p - p_0) = \int \mathbf{f} dn \quad \text{with} \quad \mathbf{f} = -\nabla p \quad (2.30)$$

satisfying (2.19). As will be evaluated in chapters 5 and 6 this conservative load does not contribute to the energy balance.

**2.5.4. Pressure interpreted as potential energy.** [Batchelor \(1970, p. 138, 157\)](#) and [Kundu \(1990, p. 102\)](#) mention that  $\mathcal{F}$  can be considered as the potential energy. The same holds for pressure as Batchelor suggests (p. 157) that 'under certain conditions the pressure might play the part of a potential energy'. Equation (2.27) shows that the work done by  $\mathbf{f}$  is expressed in a change of pressure, kinetic energy or both. Consequently the pressure is to be considered as potential energy, while the Bernoulli value  $H$  expresses the total amount of energy which can be changed by non-conservative forces. The interpretation of pressure as potential energy is supported by [Morrison \(2006\)](#) who states that for ideal flows 'potential energy is stored in terms of pressure and temperature'. As here the flow is considered to be isentropic temperature does not play a role, leaving pressure as a measure for potential energy. The conversion of potential to kinetic energy depends on the evolution of the wake behind the force field.

As an example we take the flow through the actuator disc without swirl. The load on an energy extracting disc decreases the potential energy in the near wake, which is converted to a loss of kinetic energy in the far wake having recovered undisturbed pressure. For a disc adding energy to the flow the same happens in an opposite way. In section 6.3.2 an energy adding disc flow will be treated where the increase of energy in the wake is found to be only potential energy, so is expressed in pressure.

## 2.6. Definition of (non-)conservative forces as used in this book

The mathematical definition of non-conservative and conservative forces is given by (2.15) and (2.19) respectively. These equations define the local character of the force field, not of the entire distribution. For the analyses in this book the following unambiguous characterization of a force field distribution is used:

**DEFINITION 2.1.** A force field distribution integrated on a surface  $S$  or a volume  $V$  with finite dimensions is non-conservative when it releases vorticity into the flow. It is conservative when this is not done. In an inertial frame of reference non-conservative forces perform work, while conservative forces act perpendicular to the local velocity vector, so do not perform work.

## 2.7. Evaluation

In this chapter we answered research question Q1 in section 1.4: the kinematic method (loads as output of flow analyses) is consistent with the dynamic method (loads as input). The advantage of the dynamic method is that it gives explicit relations for the work done by the load on lifting surfaces. Also Q2 and Q3 are answered: the distinction between conservative and non-conservative forces is useful for the interpretation of the physical processes: conservative forces do not produce vorticity and do not convert energy but convert potential energy (pressure) to kinetic energy or vice-versa. Non-conservative forces do produce vorticity and convert energy. This distinction will play a role in the momentum theory chapters 5 and 6, and in chapter 7. For steady actuator disc flows and steadily rotating rotors the work done by the force field is expressed in a change of Bernoulli value  $H$ . For the flows considered here the pressure term in  $H$  represents the potential energy.

In the next chapter the relation between loads and vorticity is analysed in more detail.

This page intentionally left blank

## Force fields and vorticity

### 3.1. Introduction

One of the distinct features of the force field approach is the direct link with the generation of vorticity according to (2.16) or (2.17). The literature on creation of vorticity by force fields is limited. Several authors, e.g. [Betz \(1950\)](#), mention viscosity as the main source of vorticity while the force fields discussed here act in an inviscid flow. This is brought up for discussion by some authors. [von Kármán and Burgers \(1935\)](#) and [Saffman \(1992\)](#) treat the impulsive motion of respectively a force field and a body as a source of vorticity. With the equivalence of the kinematic and dynamic method, both impulsive actions become the same. [von Kármán and Burgers \(1935\)](#) also treat the continuous creation of vorticity for which they show that  $\nabla \times \mathbf{F} \neq 0$  is the requirement. [Prandtl \(1924\)](#) presents how vortex sheets emanate from a sharp aerofoil trailing edge in inviscid flow, but this solution is given another interpretation by [van Kuik \(2004\)](#). [Batchelor \(1970, section 5.4\)](#) describes the creation of vorticity by moving surfaces in inviscid fluid at rest. All of these analyses are presented in the inviscid Euler flow representation. [Morton \(1984\)](#) presents a comprehensive treatment on the generation of vorticity and the role of viscosity herein. He covers the mechanisms mentioned above, concluding that vorticity is generated by pressure gradients: non-zero tangential pressure gradients at the surface create vorticity while viscosity is responsible for diffusion. By (2.13) a non-zero tangential pressure gradient  $\partial p / \partial s$  is the same as a non-conservative force derivative  $\partial F_n / \partial s$ .

This limited literature study does not cover the topic of vorticity generation comprehensively, but is sufficient for the purpose of this chapter: vorticity generation in inviscid flows is possible by non-conservative force fields. While most kinematic considerations are qualitative and descriptive, the force field approach gives an explicit relation: (2.16) and (2.17) connect the force field to the *generation* of vorticity. This seems to be in contrast to Helmholtz's *conservation* laws which are often used in textbooks to show that circulation, being the integrated vorticity, is conserved when going from bound to free vortices. This will be analysed in section 3.2, after which the generation of vorticity by an actuator disc force field is treated in detail in section 3.3.

### 3.2. The role of Helmholtz's conservation laws

A lifting surface like a wing or rotor blade can be represented by a bound vortex, which is continued in the flow by trailing vortices. For a rotor blade the combination of the root vortex, blade-bound vortex and the tip vortex constitute a continuous vortex system, as shown at the left of figure 3.1 copied from

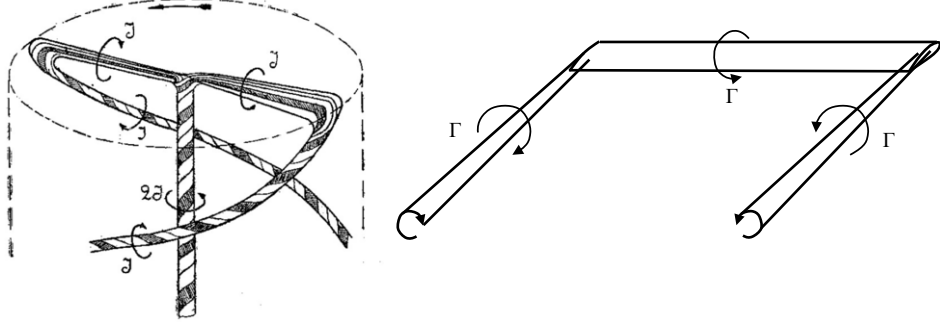


Figure 3.1: The rotor model of Joukowsky, left, and wing model of Prandtl, right. Joukowsky uses  $\mathcal{J}$  as symbol for circulation, where Prandtl uses  $\Gamma$ .

[Joukowsky](#) (1912). This is to be considered as the equivalent of the 'horse-shoe' vortex of a wing as developed by [Prandtl](#) (1918), displayed at the right of figure 3.1. When the bound vortex  $\Gamma$  ( $J$  in the left part of figure 3.1) is assumed to be constant, the models of Prandtl and Joukowsky show a continuous vortex line of uniform strength which is often explained by the vorticity conservation laws of Helmholtz, see e.g. [Clancy](#) (1986), [Kundu](#) (1990), [Katz and Plotkin](#) (2001), [Anderson Jr](#) (2011) and [Rathakrishnan](#) (2013). However, when the wing or blade is represented by a distribution of force fields  $\mathbf{F}$ , (2.17) shows that vorticity is generated instead of conserved. To solve this apparent contradiction, the original publication of [Helmholtz](#) (1858) has been studied. He clearly states that his conservation laws assume that there are no non-conservative force fields. Furthermore the concept of bound vorticity does not appear in his paper as this was introduced only half a century later by [Lanchester](#) (1907) and [Prandtl](#) (1918, I. Mitteilung). Prandtl himself notes that the concept of bound vorticity is not covered by Helmholtz's conservation laws. Consistent with this [Meyer](#) (1982, p. 42) shows that Helmholtz's laws are not applicable to bound vorticity. [Saffman](#) (1992, p. 10) confirms that these vorticity conservation laws are not applicable, since these have been derived assuming only conservative forces. In other words, the laws of Helmholtz cannot be used to explain the continuation of bound vorticity in trailing vorticity.

The correct kinematic explanation for the creation of trailing vorticity is well described by e.g. [Batchelor](#) (1970) and [Lighthill](#) (1986) who use Stokes' theorem to show that for a wing:

$$\gamma_{trailing} = -d\Gamma_{bound}/dy \quad (3.1)$$

with  $y$  the spanwise coordinate. These considerations do not affect the validity of the horse-shoe models of Prandtl and Joukowsky but the physical explanation: these models do not proceed from *conservation* of vorticity. Similarly this holds for Kelvin's circulation theorem. The circulation around any closed contour enclosing the bound or free vortices equals  $\Gamma$ , so is constant. However, this is not because of vorticity conservation since Kelvin's theorem is derived assuming 1) only conservative forces, 2) the contour being a material contour convected with

the flow, see Saffman (1992, §1.6). This is not the case for lifting surfaces, since a material contour around the tip vortextip vortex was a circulation-free contour when it was still upstream of the surface position.

The conclusion is that a lifting surface generates vorticity which may be modelled by the dynamic method using (2.17) and by the kinematic method using (3.1). There is no conflict with Helmholtz's laws since these do not apply. The circulation of bound and free vortices is the same, although this is not based on Helmholtz's laws or Kelvin's theorem. By this result the apparent contradiction between a rotor and actuator disc is removed: both generate vorticity governed by the curl of the force field.

### 3.3. Generation of actuator disc vorticity

A contour  $\mathcal{L}$  enclosing the upstream part of the stream tube is free of circulation  $\Gamma$ . It remains so when moving downstream enclosing the wake, as can be explained in terms of the force field. Branlard (2017, eq. 2.159) shows that for incompressible inviscid flow  $\frac{d\Gamma}{dt} = \oint_{\mathcal{L}(t)} \mathbf{F} \cdot d\mathbf{l}$ . In case the force field is absent Kelvin's theorem follows, but also when  $\oint \mathbf{F} \cdot d\mathbf{l} = 0$ . For a rotor or disc force field, (2.18) is valid by which this is true, so Kelvin's theorem applies to a contour enclosing the stream tube. This implies that the total of axial vorticity enclosed by  $\mathcal{L}$  must be zero, irrespective of the stream wise position of  $\mathcal{L}$ . Here we analyse how the generation of vorticity by the disc force field satisfies Kelvin's theorem.

For the Joukowsky actuator disc, shown in figure 3.2 and described in Explanation 3.1, the generation and convection of vorticity is analysed in detail. As only the pressure and azimuthal velocity will be discontinuous across the infinitely thin disc, integration of (2.1) across the disc gives:

$$\mathbf{F} = \mathbf{e}_x \Delta p + \mathbf{e}_\varphi \rho v_x \Delta v_\varphi. \quad (3.2)$$

The Bernoulli equation  $p + \frac{1}{2} \rho \mathbf{v} \cdot \mathbf{v} = H$ , integrated across the disc, is:

$$F_x = \Delta p = \Delta H - \frac{1}{2} \rho \Delta v_\varphi^2 \quad (3.3)$$

so:

$$\mathbf{F} = \mathbf{e}_x \left( \Delta H - \frac{1}{2} \rho \Delta v_\varphi^2 \right) + \mathbf{e}_\varphi \rho v_x \Delta v_\varphi. \quad (3.4)$$

Evaluation of  $\nabla \times \mathbf{F}$  gives:

$$\mathbf{e}_x \frac{1}{\rho} \frac{\partial (r F_\varphi)}{r \partial r} - \mathbf{e}_\varphi \frac{1}{\rho} \frac{\partial F_x}{\partial r} = \mathbf{e}_x \frac{\partial (r v_x \Delta v_\varphi)}{r \partial r} - \mathbf{e}_\varphi \frac{\partial \left( \frac{1}{\rho} \Delta H - \frac{1}{2} \Delta v_\varphi^2 \right)}{\partial r}. \quad (3.5)$$

For any load distribution the integration of  $\partial(r F_\varphi)/(r \partial r)$  over the entire disc gives a nett zero result, so the total amount of axial vorticity produced by the disc is zero. This is not the same for the  $\partial F_x/\partial r$ : the nett production of azimuthal vorticity is non-zero. Three regions are distinguished to analyse (3.5):

**EXPLANATION 3.1. Joukowsky circulation distribution** Figure 3.2 shows the rotor and disc model of Joukowsky, characterized by a constant circulation  $\Gamma$ . For the 1-bladed rotor shown in the figure the vortices at the axis, blade and tip have equal strength. The disc vorticity system has the same vortex at the axis and constant  $\Gamma = -\gamma_{disc}2\pi r$ . The azimuthal velocity in the wake of a rotor, averaged over a revolution, and the local velocity in the disc wake are:  $v_\varphi = \Gamma/(2\pi r)$ . For both systems the flux of  $v_\varphi \Omega r$  represents the work done by the disc or rotor force field, see section 4.2. For a disc with  $\Omega \rightarrow \infty$  the azimuthal velocity vanishes like  $\Omega^{-1}$  as will be shown in section 4.3.

The disc region:  $\delta < r < R$  where  $\delta$  is the radius of the vortex core at the axis and where  $\Delta v_\varphi = \Gamma/(2\pi r)$ . With  $\partial v_\varphi / \partial r = -v_\varphi/r$  (3.4) and (3.5) become:

$$\mathbf{e}_x \frac{1}{\rho} \frac{\partial(rF_\varphi)}{r \partial r} - \mathbf{e}_\varphi \frac{1}{\rho} \frac{\partial F_x}{\partial r} = \mathbf{e}_x (r\Delta v_\varphi) \frac{\partial v_x}{r \partial r} - \mathbf{e}_\varphi \frac{\Delta^2 v_\varphi}{r}, \quad (3.6)$$

with  $r\Delta v_\varphi$  being independent of  $r$  as it concerns a Joukowsky disc.

This shows that the distribution of  $rF_\varphi$  is responsible for the distribution of the angular momentum  $rv_x\Delta v_\varphi$ , thereby creating the disc vortex sheet strength  $\mathbf{e}_r \gamma$ , defined by the velocity discontinuity across the disc:

$$\mathbf{e}_r \gamma = -\mathbf{e}_r \Delta v_\varphi. \quad (3.7)$$

The axial load derivative provides the required centripetal pressure distribution  $\frac{1}{\rho} \frac{\partial \Delta p}{\partial r} = \Delta^2 v_\varphi/r$ . Furthermore  $F_x$  depends only on  $v_\varphi$  where  $F_\varphi$  depends too on the distribution of  $v_x$ :

$$F_x \propto r^{-2} + \text{constant}, \quad F_\varphi \propto \frac{v_x}{r}. \quad (3.8)$$

This describes the load on an infinitely thin disc. For a disc with thickness, several other terms contribute to the right-hand side of (3.5). In chapter 7 the role of these additional terms is evaluated for a disc load generating a wake with a solid body rotation like a Rankine vortex.

The disc centre:  $r \leq \delta$ . If a Rankine core is assumed<sup>1</sup>  $\Delta v_\varphi = \frac{r}{\delta} \frac{\Gamma}{2\pi\delta}$ . Integration of (3.5) across the core yields, with  $(\frac{1}{\rho} \Delta H - \frac{1}{2} \Delta v_\varphi^2) = \frac{1}{\rho} (\Delta p + v_x^2 - U_0^2)$  remaining finite for  $\delta \rightarrow 0$ :

$$\frac{1}{\rho} \lim_{\delta \rightarrow 0} \int_0^\delta \nabla \times \mathbf{F} 2\pi r dr = \lim_{\delta \rightarrow 0} \int_0^\delta \mathbf{e}_x \frac{\Gamma}{2\pi\delta^2} \frac{\partial(r^2 v_x)}{r \partial r} 2\pi r dr \quad (3.9)$$

$$= \lim_{\delta \rightarrow 0} \int_0^\delta \mathbf{e}_x v_x \frac{\Gamma}{\pi\delta^2} 2\pi r dr \quad (3.10)$$

$$= \mathbf{e}_x \bar{v}_x \Gamma \quad \text{for } r < \delta, \quad (3.11)$$

showing that the force field produces the centreline vortex  $\Gamma$ .

<sup>1</sup>The Rankine core is known as a viscous core, but the same distribution of  $\Delta v_\varphi$  can be generated by a force field  $\mathbf{F}$ , see van Kuik et al. (2014) and chapter 7.

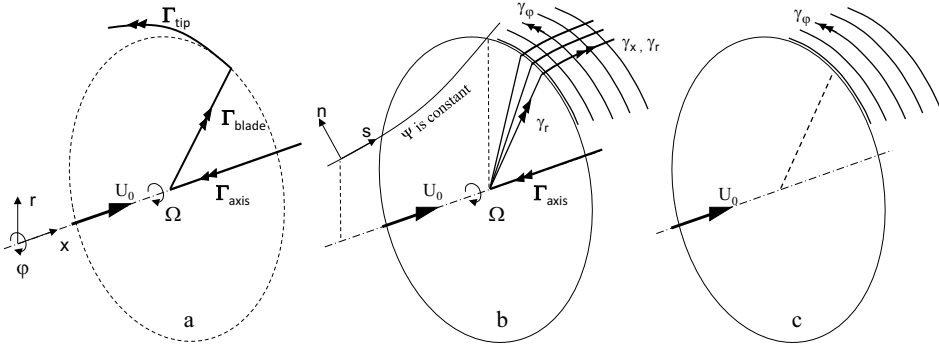


Figure 3.2: The Joukowsky circulation distribution for (a) a one-bladed lifting line rotor, (b) the actuator disc with swirl, and (c) the classical disc without swirl, see Explanation 3.1.

The disc edge:  $r = R$ , where integration of the right-hand side of (3.5) across the disc edge gives:

$$\frac{1}{\rho} \int_{edge} \nabla \times \mathbf{F} 2\pi r dr = -\mathbf{e}_x (2\pi R v_x \Delta v_\varphi)_{r=R} + \mathbf{e}_\varphi 2\pi R \left( \frac{\Delta H}{\rho} - \frac{1}{2} \Delta v_\varphi^2 \right)_{r=R} \quad (3.12)$$

$$= -\mathbf{e}_x v_x \Gamma + \mathbf{e}_\varphi 2\pi R F_x \quad \text{for } r = R, \quad (3.13)$$

where (3.3) has been used. The axial component shows that the force field produces the axial vorticity having the same circulation as the root vortex but with a negative sign. With (2.17) the azimuthal component can be written as  $\int_{edge} \frac{D\omega_\varphi}{Dt} r dr = \frac{D\Gamma_\varphi}{Dt}$  expressing the increase of azimuthal circulation of the wake boundary. Combined with (3.13) this gives:

$$\frac{D\Gamma_\varphi}{Dt} = \frac{1}{\rho} 2\pi R F_{x,edge}, \quad (3.14)$$

so only the pressure jump at the edge defines the increase of  $\Gamma_\varphi$ . In summary we see that the force field

- creates the disc bound vorticity  $\gamma_r$ ,
- sheds equal amounts of positive and negative axial vorticity: the root vortex  $\Gamma$  and the wake boundary with the axial component equalling  $-\Gamma$ ,
- sheds azimuthal vorticity being part of the wake boundary.

### 3.4. Convection of actuator disc vorticity

So far the occurrence of free radial vorticity does not follow from the preceding equations. In other words: the disc force field does not generate the radial component of the wake boundary vorticity but is a consequence of convection. Once generated, vorticity is convected with the flow  $\mathbf{v}$  and is subject to stretching and tilting, described by  $(\boldsymbol{\omega} \cdot \nabla) \mathbf{v}$ . In the wake  $\mathbf{f} = 0$  so the azimuthal component of

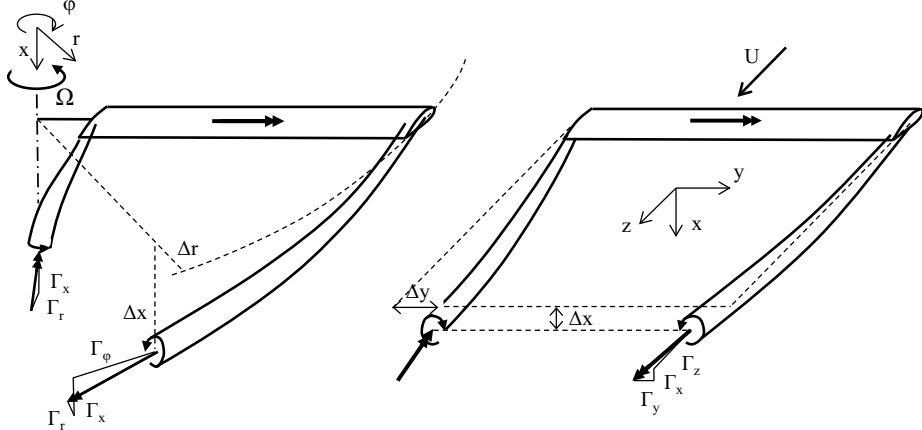


Figure 3.3: Details of the vortices trailing from a rotor blade in hover and a wing.

the steady version of (2.16) becomes:

$$(\mathbf{v} \cdot \nabla) \omega_\varphi = (\boldsymbol{\omega} \cdot \nabla) v_\varphi - \omega_r \frac{v_\varphi}{r} + \omega_\varphi \frac{v_r}{r}. \quad (3.15)$$

By substitution of the axial and radial components of (A.7)  $(\boldsymbol{\omega} \cdot \nabla) v_\varphi = \omega_x \partial v_\varphi / \partial x + \omega_r \partial v_\varphi / \partial r = -\omega_r v_\varphi / r$  is obtained, so:

$$(\mathbf{v} \cdot \nabla) \omega_\varphi = -2\omega_r \frac{v_\varphi}{r} + \omega_\varphi \frac{v_r}{r}. \quad (3.16)$$

According to Darmofal (1993) the first term at the right hand side describes the change of azimuthal vorticity due to tilting of radial vorticity. The second term describes the stretching of vorticity, also described by Saffman (1992, p. 14). Further simplification of (3.16) is achieved by considering (2.22). In the wake but also outside the wake  $\nabla(H - \rho v_\varphi \Omega r) = 0$  so this term vanishes after the integration of (2.8) across the free vortex sheet forming the wake boundary, resulting in  $\mathbf{v}_{rot} \times \boldsymbol{\omega} = 0$ . The  $x$ -component reads  $v_r \omega_\varphi = v_{\varphi,rot} \omega_r$ . With (2.5) this becomes  $v_r \omega_\varphi = (v_\varphi - \Omega r) \omega_r$ . Substitution in (3.16) yields:

$$(\mathbf{v} \cdot \nabla) \omega_\varphi = -\left(\frac{v_\varphi}{r} + \Omega\right) \omega_r. \quad (3.17)$$

Equation (3.17) shows that  $\omega_r$  depends on the convection of  $\omega_\varphi$ , so is needed to transport the azimuthal vorticity to other radii. Once generated, the azimuthal vorticity is determined by the boundary conditions for a free vortex sheet, satisfying conservation of circulation within a contour moving with the flow.

The axial vorticity contained in the centreline vortex and wake boundary are related, as shown in figure 3.2b, where the wake vorticity is decomposed. The centreline vorticity, the disc bound vorticity and the axial wake boundary vorticity constitute a system of connected vortex lines of equal (integrated) strength. Conservation of circulation on a contour  $\mathcal{L}$  enclosing the stream tube is satisfied, as discussed in the previous section. This vortex system induces the swirl in the

wake, which is the measure for the work done by the force field as will be shown in the next chapter.

### 3.5. Convection of rotor vorticity

Figure 3.1 shows the linearised vortex models of Joukowsky for a two-bladed rotor and of Prandtl for a wing. Comparison with the physical models as shown in figure 3.3 show the simplifications of the early models: Joukowsky kept the wake radius  $R$  constant,  $\Delta r = 0$ , as well as the pitch  $\theta = \arctan \frac{x}{r\varphi}$  of the wake spirals constant, so  $\Delta x = R\varphi \tan \theta$ . Prandtl (1918) assumes zero inboard and downward movement of the tip vortices,  $\Delta x = \Delta y = 0$  (see also Milne-Thomson (1966)). The distances  $\Delta x$ ,  $\Delta y$  and  $\Delta r$  are shown in figure 3.3. For a wing  $\Delta x$  and  $\Delta y$  indicate the location of the wing tip vortices with respect to the plane defined by the undisturbed wind speed vector and the vector along the wing span, for a rotor blade  $\Delta x$  and  $\Delta r$  give the downwind respectively inboard displacement of the tip vortex.

Conservation of wake circulation by Kelvin's theorem as discussed in section 3.2 shows that the summation of all axial vorticity in the rotor wake at any downstream  $x$ -position has to be zero, so  $\int \omega_x dA_{x,root} = -\int \omega_x dA_{x,tip}$  where  $A_x$  is the cross-section of the vortices with the plane  $x = \text{constant}$ . This leads to  $\Gamma_{x,root} = -\Gamma_{x,tip}$ . At first sight this may conflict the rotor equivalent of (3.1), expressing that the root and tip vortices equal the  $+/-$  strength of the bound blade vortex:  $\Gamma_{root} = -\Gamma_{tip}$ . However, this equation originates from  $\int |\boldsymbol{\omega}| dA_{root} = -\int |\boldsymbol{\omega}| dA_{tip}$  in which  $A$  is the cross section of the vortex perpendicular to the direction of the vorticity  $\boldsymbol{\omega}$ . Geometric considerations show that  $\int \omega_x dA_{x,root} = \int |\boldsymbol{\omega}| dA_{root}$ .

A characteristic difference between the linearised rotor and wing models is observed. First is that  $\Delta x \neq 0$  in the rotor model while  $\Delta x = 0$  in the wing model. Converted to the components of the vorticity, this implies that  $\Gamma_x = 0$  for the linearised wake of a wing, while for a rotor it is essential to have  $\Gamma_x \neq 0$  since  $\Gamma_x$  defines the swirl. In the next chapter we show that the swirl defines the converted power. In other words: the vorticity component that is least important for determining the performance of a wing is essential for a rotor.

## 3.6. Evaluation

This chapter contributes to the answer of question Q2 in section 1.4: the force field approach allows explicit expressions for the generation of vorticity by non-conservative force fields acting on lifting surfaces. Furthermore this chapter gives an answer to research question Q4: with respect to vorticity dynamics, there is no conceptual difference between the most simple model of a rotor, the actuator disc, and real rotor models. In both type of models vorticity is produced by the disc or rotor blade instead of conserved. The continuation of the blade bound vorticity into free tip vorticity is not governed by Helmholtz's conservation laws as often assumed. Furthermore the components of bound and free vorticity in actuator disc flows have been characterised. The relations between forces, energy and vorticity will be used in subsequent chapters. Particularly equation (3.3) will play a major role in chapter 6.

This page intentionally left blank

## The disc as representation of a rotor

### 4.1. Introduction

The actuator disc momentum theory is the basis for the design and load calculations of real rotors with a finite number of blades. In this chapter the expressions for thrust and power for a disc and rotor are derived and compared in order to find similarities and differences. Furthermore the limit transitions to convert a real rotor to a disc with an axisymmetric load will be presented as an answer to the question: is the actuator disc the result of a rotor subjected to the limit of the number of blades  $B \rightarrow \infty$ , the blade cross section  $C \rightarrow 0$ , the rotational speed  $\Omega \rightarrow \infty$ , meanwhile keeping the converted power  $P$  and thrust  $T$  constant? Thereafter, section 4.4 compares the velocity fields of a disc and a rotor having the same size and having been measured in the same wind tunnel.

### 4.2. Loads and power of a Joukowsky disc and rotor

Joukowsky discs and rotors (in equations abbreviated as J-disc and J-rotor) are characterised by a constant circulation  $\Gamma$  around the axis, as shown in figure 3.2 and mentioned in Explanation 3.1. This centreline vortex is modelled with a vortex core having radius  $\delta$ . For  $r \geq \delta$   $v_\varphi = \Gamma/(2\pi r)$ , inside the core  $v_\varphi$  depends on the assumed characteristics of the core.

**4.2.1. The actuator disc equation.** The power produced or absorbed by an annulus  $dr$  of the actuator disc can be expressed in two ways. First as torque  $Q$  times rotational speed  $\Omega$  giving  $\Omega dQ = 2\pi\Omega f_\varphi r^2 dr$ , second by integration of  $\mathbf{f} \cdot \mathbf{v}$  using the steady version of (2.3), resulting in  $2\pi r(\mathbf{v} \cdot \nabla) H dr$ . Comparison shows that:

$$\mathbf{f} \cdot \mathbf{v} = \Omega r f_\varphi = (\mathbf{v} \cdot \nabla) H. \quad (4.1)$$

The expression for  $f_\varphi$  is derived from the  $\varphi$ -component of the steady version of (2.1), with the help of (A.4):

$$r f_\varphi = \rho(\mathbf{v} \cdot \nabla) r v_\varphi. \quad (4.2)$$

Substitution in (4.1) gives:

$$\mathbf{f} \cdot \mathbf{v} = \rho(\mathbf{v} \cdot \nabla) (\Omega r v_\varphi) = (\mathbf{v} \cdot \nabla) H, \quad (4.3)$$

so:

$$\frac{1}{\rho} \nabla H = \nabla (\Omega r v_\varphi) = \nabla \left( \frac{\Omega \Gamma}{2\pi} \right). \quad (4.4)$$

This relation between converted power and azimuthal velocity has been obtained in chapter 2 for flows without force fields and vorticity, see (2.22), but is now shown to be valid at the disc too. Equation (4.4) shows that the work done by

the force field is expressed in a change in the total pressure or Bernoulli constant  $H$ . Integrated across the disc this gives:

$$\Delta H_d = \rho \Omega r v_\varphi \quad (4.5)$$

so combined with (3.3):

$$F_x = \Delta p_{d,\Delta H} + \Delta p_{d,v_\varphi} = \rho \Omega r v_\varphi - \frac{1}{2} \rho v_\varphi^2. \quad (4.6)$$

Both terms at the right-hand side are pressure jumps:  $\rho \Omega r v_\varphi$  converts power so is a non-conservative disc load,  $-\frac{1}{2} \rho v_\varphi^2$  is required for the radial pressure gradient balancing  $v_\varphi$ . The increase of kinetic energy,  $\frac{1}{2} \rho v_\varphi^2$  is balanced by the change in potential energy  $\Delta p_{d,v_\varphi} = -\frac{1}{2} \rho v_\varphi^2$  and is not a measure of the work done.

A combination of (4.4) with (2.8) gives the actuator disc equation:

$$\mathbf{f} = -\rho \mathbf{v}_{rot} \times \boldsymbol{\omega}. \quad (4.7)$$

An alternative way to derive (4.7) is to express (4.4) in  $\boldsymbol{\omega}$ :  $\nabla(\Omega r v_\varphi) = \mathbf{e}_\varphi \Omega r \times \boldsymbol{\omega}$ . Substitution in the steady version of the Euler equation (2.3) using the coordinate transformations (2.5) and (2.6) results in (4.7).

Equation (4.7) is the equation of motion for the steady actuator disc converting power for any radial distribution of  $\mathbf{f}$ . The subscript  $rot$  in (4.7) distinguishes it from the expression of a Kutta-Joukowsky force: the disc load is the cross product of the velocity as experienced in the rotating system with the vorticity in the inertial system. Since it is expressed in kinematic terms it enables an easier physical interpretation of the relation between loads and vorticity compared to the Euler equation including  $H$ .

The thrust  $T$  is obtained by integration of (4.7) on the disc volume. With  $\epsilon$  denoting the thickness of the disc, the limit  $\epsilon \rightarrow 0$  gives, analogous to the conversion of (2.9) to (2.10),  $\int_\epsilon \mathbf{v}_{rot} \times \boldsymbol{\omega} d\epsilon = \bar{\mathbf{v}}_{rot} \times \boldsymbol{\gamma}_d$ . For a Joukowsky disc  $2\pi r \boldsymbol{\gamma}_d = -\Gamma$ , see (3.7), so the thrust becomes, using (2.5):

$$\begin{aligned} T &= \rho \oint \int_0^R \bar{v}_{\varphi,rot} \gamma r dr d\varphi = -\rho \Gamma \int_0^R \bar{v}_{\varphi,rot} dr \\ &= \rho \frac{\Omega \Gamma}{2} R^2 - \rho \Gamma \int_{\delta}^R v_{\varphi,d} dr \quad \text{for a J-disc, } \delta \rightarrow 0 \end{aligned} \quad (4.8)$$

The power converted by the non-conservative force field of a steady actuator disc or a steadily rotating rotor is given by (2.26). As a conservative force field does not convert power, see (2.28), this can be generalized to:

$$P = \int_V \mathbf{f} \cdot \mathbf{v} dV = \int_S H (\mathbf{v} \cdot \mathbf{e}_{n,S}) dS \quad (4.9)$$

with volume  $V$  having surface  $S$  shown in figure 2.5b. At the cross section with the wake  $\mathbf{v} \cdot \mathbf{e}_{n,S} = v_x$ . At the cross section with the stream tube far upstream the velocity is undisturbed  $U_0$ . For the part of  $V$  outside the stream tube  $H = H_0$

and  $\int (\mathbf{v} \cdot \mathbf{e}_{n,S}) dS = 0$  so the expression for the converted power becomes:

$$\int_V \mathbf{f} \cdot \mathbf{v} dV = \int_{A_1} H v_x dA_1 - H_0 U_0 A_0, \quad (4.10)$$

where  $A_0$  is the cross section of the stream tube far upstream and  $A_1$  the same far downstream. For a Joukowsky disc (4.4) shows that in the wake  $H$  is constant. Mass conservation  $U_0 A_0 = v_x A_1$  gives:

$$P = (H - H_0) \int_{A_1} v_x dA_1 \text{ for a J-disc, } \delta \rightarrow 0, \quad (4.11)$$

or, with (2.22):

$$P = \rho \Omega \Gamma \int_{\delta_1}^{R_1} v_x r_1 dr_1 = \rho \frac{\Omega \Gamma}{2\pi} \bar{v}_{x,d} R^2 \quad \text{for a J-disc, } \delta \rightarrow 0, \quad (4.12)$$

where conservation of mass is used to convert the integral from plane  $A_1$  to the disc area, and where  $\bar{v}_{x,d}$  is the disc averaged axial velocity.

**4.2.2. The rotor blade.** Figure 4.1 shows a rotor blade having a cross section  $C$  at which the bound vorticity is distributed. The sectional load on a blade is derived in the rotating coordinate system by integration of (2.8) on  $C$ :

$$\mathbf{L} = -\rho \int_C \mathbf{v}_{rot} \times \boldsymbol{\omega} dC + \int_C \nabla (H - \rho v_\varphi \Omega r) dC. \quad (4.13)$$

According to (4.4) the gradient term is zero for an actuator disc, but for a rotor this is not yet clear. The integral is converted by Green's theorem to  $\oint (H - \rho v_\varphi \Omega r) \mathbf{e}_n dS$  where  $S$  is a contour enclosing  $C$  and  $\mathbf{e}_n$  the outward unit vector at  $S$  in the plane of  $C$ . According to (2.22) the integrand is constant when  $\boldsymbol{\omega} = 0$ , so outside of the vortex sheet leaving the aerofoil. As we consider inviscid flows, any vorticity leaving the aerofoil trailing edge is concentrated in an infinitely thin sheet. At the sheet the integrand  $(H - \rho v_\varphi \Omega r)$  has to behave as a Delta function in order to contribute to the integral. As  $H$  and  $\rho v_\varphi \Omega r$  remain finite, this is not the case. Consequently  $\oint (H - \rho v_\varphi \Omega r) \mathbf{e}_n dS = 0$ , by which the sectional load (4.13) becomes:

$$\mathbf{L} = -\rho \int_C \mathbf{v}_{rot} \times \boldsymbol{\omega} dC. \quad (4.14)$$

Depending on the orientation of  $\mathbf{v}_{rot}$  and  $\boldsymbol{\omega}$  the sectional load may have a radial component, besides the axial and azimuthal components. Figure 4.1 shows the load on the radial bound vorticity but also, close to the blade tip and root, on the chordwise bound vorticity, being able to carry an additional axial and radial load. This is treated in detail in chapter 7. In case the blade is modelled as a lifting line, so  $C \rightarrow 0$ , only the radial bound vorticity is taken into account, and:

$$\lim_{C \rightarrow 0} \mathbf{L} = -\rho \int_C \mathbf{v}_{rot} \times \mathbf{e}_r \omega_r dC = -\rho \mathbf{v}_{rot,B} \times \mathbf{\Gamma}_B \quad (4.15)$$

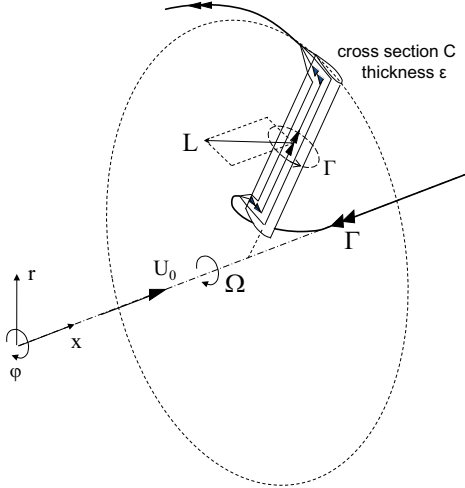


Figure 4.1: The load on bound radial vorticity of a wind turbine rotor blade.

with the blade bound vortex strength  $\mathbf{\Gamma}_B = e_r \int_C \omega_r dC$  remaining invariant for  $C \rightarrow 0$ , and with  $\mathbf{v}_{rot,B}$  the velocity at the position of the lifting line. This is the expression for the Kutta-Joukowsky load used in rotor aerodynamic textbooks like [Stepniewski and Keys \(1978\)](#), [Leishman \(2006\)](#) and [Schaffarczyk \(2014\)](#). Blade Element Momentum design methods as presented by [Sørensen \(2015\)](#) and wind turbine textbooks like [Burton et al. \(2011\)](#) express the inviscid load as  $L_{blade} = C_l \frac{1}{2} \rho v_{rel}^2 c$  where  $c$  is the chord,  $C_l$  the lift coefficient and  $v_{rel}$  the velocity perceived by the blade, so identical to  $v_{rot}$ . This expression is fully equivalent to  $-\rho \mathbf{v}_{B,rot} \times \mathbf{\Gamma}$ .

The thrust at the rotor is defined by the axial component of (4.15). With (2.5) and with  $\Gamma = -B\mathbf{\Gamma}_B$ :

$$T = -\rho \Gamma \int_{\delta}^R v_{\varphi,rot,B} dr_d = \rho \frac{\Omega \Gamma}{2} R^2 - \rho \Gamma \int_{\delta}^R v_{\varphi,B} dr_d \text{ for a J-rotor, } \delta \rightarrow 0. \quad (4.16)$$

The converted power  $P$  is torque  $Q$  times  $\Omega$ , so with the azimuthal component of (4.15):

$$P = Q\Omega = -\Omega B\rho \int_{\delta}^R \int_C v_x \omega_r r dr_d dC. \quad (4.17)$$

In (4.15) the limit  $C \rightarrow 0$  was included, so  $\int_C v_x \omega_r dC = v_{x,B} \Gamma_B$ . As before  $\Gamma = -B\mathbf{\Gamma}_B$ , yielding:

$$P = \rho \Omega \Gamma \int_{\delta}^R v_{x,B} r dr \text{ for a J-rotor, } \delta \rightarrow 0. \quad (4.18)$$

Equations (4.16) and (4.18) are equivalent to the disc equations (4.8) and (4.12) apart from the indication  $B$  in (4.18).

A contribution by the vortex kernel itself is not included in  $P$  and  $T$  as we have assumed a Rankine-like distribution of  $v_\varphi$  with  $v_\varphi = 0$  at  $r = 0$ . Evaluation of the contribution to  $P$  and  $T$  shows that the kernel does not contribute when  $\delta \rightarrow 0$ .

For the disc as well as rotor the conversion of power by the force field is expressed in the in- or decrease of the amount of wake swirl. The sign conventions shown in figure 2.2 are that the rotational speed  $\Omega > 0$  and  $\Gamma < 0$  for energy extracting discs, so  $\Delta H < 0$ . For an energy adding disc  $\Gamma$  and  $\Delta H > 0$ .

**4.2.3. Power and thrust coefficients for Joukowsky discs / rotors.**  
The disc: Equation (4.12) gives the expression for the power  $P$  converted by the disc. With the introduction of the non-dimensional vortex strength  $q = \Gamma/(2\pi R U_0)$  and tip speed ratio  $\lambda = \Omega R/U_0$ , (4.5) becomes:

$$\frac{\Omega\Gamma}{2\pi} = 2q\lambda \quad \text{for } r \geq \delta. \quad (4.19)$$

Herewith the dimensionless power coefficient  $C_p$  becomes<sup>1</sup>:

$$C_p = \frac{P}{\frac{1}{2}\rho U^3 \pi R^2} = 2q\lambda \frac{\overline{v_{x,d}}}{U_0} \quad \text{for a J-disc, } \delta \rightarrow 0. \quad (4.20)$$

The thrust  $T$  is given by (4.8). As the first term at the right-hand side of (4.8) is the thrust converting power and the second term the thrust due to the pressure gradient connected to the rotation of the wake, the dimensionless thrust coefficient is written as:

$$\left. \begin{aligned} C_T &= \frac{T}{\frac{1}{2}\rho U^2 \pi R^2} = C_{T,\Delta H} + C_{T,\Delta v_\varphi} \\ C_{T,\Delta H} &= 2\lambda q \\ C_{T,\Delta v_\varphi} &= -q^2 \ln \left( \frac{R}{\delta} \right)^2 \end{aligned} \right\} \text{for a J-disc, } \delta \rightarrow 0. \quad (4.21)$$

For  $\delta \rightarrow 0$   $C_{T,\Delta v_\varphi} \rightarrow \infty$ . The consequences of this will be discussed at the end of this section.

The rotor: The power is given by (4.18). As for the disc, the power coefficient becomes:

$$C_p = 2\lambda q \frac{\overline{v_{x,B}}}{U_0} \quad \text{for a J-rotor, } \delta \rightarrow 0. \quad (4.22)$$

The thrust is given by (4.16), so in dimensionless form:

$$C_T = 2\lambda q - 4q \int_{\delta}^R \frac{v_{\varphi,B}}{U_\delta R} dr. \quad (4.23)$$

---

<sup>1</sup>the definitions for  $C_p$  and  $C_T$  used here differ from the definitions used by Wald (2006), where  $C_p = P/(\rho n^3 D^5)$  and  $C_T = T/(\rho n^2 D^4)$ , but are the same as his coefficients  $K_p$  and  $K_T$ . The definitions used by Leishman (2006) are  $C_{p,\text{Leishman}} = C_p/(2\lambda^3)$ ,  $C_{T,\text{Leishman}} = C_T/(2\lambda^2)$ .

The local thrust coefficient  $C_t$  defined as  $BdL_x / (\rho U_0^2 \pi r dr)$ , where  $L_x$  is the axial component of (4.15):

$$C_t = 2\lambda q - 2q \frac{v_{\varphi,B}}{U_0} \frac{R}{r}, \text{ for a J-disc, } r \geq \delta. \quad (4.24)$$

In the wake the azimuthally averaged value  $\overline{v_\varphi} = \Gamma / (2\pi r)$  but in the rotor plane it is half this value:  $\overline{v_{\varphi,x=0}} = \Gamma / (4\pi r)$ . The azimuthal distribution of  $v_\varphi$  will be approximately uniform for low values of  $r/R$  as the induction by the root vortex dominates. However, for larger  $r/R$  values the tip vortices will add a harmonic distribution. With the actuator line and lifting line calculations of which the axial velocity is shown in figure 2.4, the order of magnitude of the approximation  $v_{\varphi,B} = \overline{v_\varphi} = \Gamma / (2\pi r)$  is estimated: the deviation in  $\Delta C_T$  is  $< 1\%$ , so the approximation is well in place. When the non-uniformity of  $v_\varphi$  is neglected,  $v_{\varphi,B}/U_0 \approx \Gamma / (4\pi r U_0)$  for  $r > \delta$  and  $\approx \Gamma r / (4\pi \delta^2 U_0)$  for  $r < \delta$  when  $v_\varphi = 0$  for  $r = 0$  is assumed. For  $\delta \rightarrow 0$  the contribution of the area  $\pi\delta^2$  to the thrust vanishes so the result for  $C_T$  is:

$$\left. \begin{aligned} C_T &= C_{T,\Delta H} + C_{T,\Delta v_\varphi} \\ C_{T,\Delta H} &= 2\lambda q \\ C_{T,\Delta v_\varphi} &= -4q \int_{\delta}^R \frac{v_{\varphi,B}}{U_0 R} dr \approx -q^2 \ln \left( \frac{R}{\delta} \right)^2 \end{aligned} \right\} \text{ for a J-rotor, } \delta \rightarrow 0 \quad (4.25)$$

and for the local thrust coefficient  $C_t$ :

$$\left. \begin{aligned} C_t &= C_{t,\Delta H} + C_{t,\Delta v_\varphi} \\ C_{t,\Delta H} &= 2\lambda q \\ C_{t,\Delta v_\varphi} &= -2q \frac{v_{\varphi,B}}{U_0} \frac{R}{r} \approx -q^2 \left( \frac{R}{\delta} \right)^2 \end{aligned} \right\} \text{ for a J-rotor, } \delta \rightarrow 0 \quad (4.26)$$

The expressions for the rotor and disc are identical, apart from the approximation in (4.25) and (4.26) for the rotor thrust component  $C_{T,\Delta v_\varphi}$ .

$C_{T,\Delta v_\varphi}$ , representing the contribution to the thrust by the radial pressure gradient balancing the radial distribution of  $v_\varphi$ , becomes  $\infty$  for  $\delta \rightarrow 0$ . With  $\delta \ll R$  the singular term is positive, so it adds up to  $C_{T,\Delta H}$  for a wind turbine rotor but is opposite to this for a propeller. For practical wind turbine conditions  $\delta$  mimics the root cut-out radius, which is the radius below which the nacelle and blade root connection occupy the space. A practical value is  $0.15R$  so for  $\lambda > 7$  and  $2\lambda q > -1$  we find that  $C_{T,\Delta v_\varphi} \leq 0.02C_{T,\Delta H}$  so this contribution to the thrust may be ignored. In forthcoming results and figures  $C_{T,\Delta H}$  will be used as parameter defining flow states, together with the tip speed ratio  $\lambda$  for wind turbine discs and the advance ration  $J = U_0/(nD)$  for propeller discs, with  $\lambda = \pi/J$ .

### 4.3. The transition from a B-bladed rotor to the Joukowsky disc

The actuator disc carrying a constant pressure jump is supposed to represent a rotor with an infinite number of blades by which the rotor load is distributed

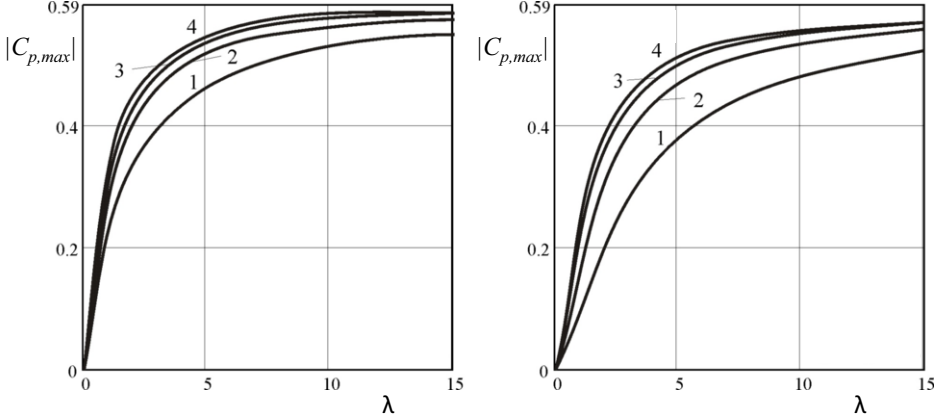


Figure 4.2: Maximum power coefficients  $|C_p|$  of an optimum rotor as function of tip speed ratio  $\lambda$  and number of blades 1 to 4. Left: Joukowsky rotor; Right: Betz rotor. From [Okulov and Sørensen \(2010\)](#) with permission.

over the entire disc. Physical arguments support this notion, as well as a numerical approach by [Okulov and Sørensen \(2010\)](#). Figure 4.2 shows the power coefficients  $C_p$  as a function of  $\lambda$  and the number of blades for the load distributions according to Betz and Joukowsky. For both distributions the  $|C_p|$  values grow to the actuator disc maximum for an increasing number of blades. A remarkable property of this analysis is that the distance between the tip vortices, modelled with a core diameter  $\delta$  to avoid velocity singularities, will not vanish for  $B \rightarrow \infty$  as  $B\delta$  remains non-zero. Apparently the transition from spiralling vortices with a vortex core to a continuous vortex sheet with a velocity jump is not an automatically generated result.

Apart from the numerical and physical arguments, an analytical transition from rotor to disc, based on the relevant equations for the rotor and disc, has to provide the formal basis for the statement that the disc represents the rotor with an infinite number of blades. The limit transitions with which Joukowsky rotors turn into a Froude disc are:  $B \rightarrow \infty$ ,  $\Omega \rightarrow \infty$ ,  $C \rightarrow 0$ , meanwhile keeping the thrust  $T$  and power  $P$  constant.

The power converted by a disc and rotor is given by (4.12) and (4.18), and the thrust by (4.8) and (4.16). The limit  $C \rightarrow 0$  has already been used in their derivation. For  $B \rightarrow \infty$  the velocity at the rotor plane will become azimuthally uniform, so with invariant power and thrust  $v_{x,B} \rightarrow v_{x,d}$  and  $v_{\varphi,B} \rightarrow v_{\varphi,d}$ , and:

$$\lim_{\substack{C \rightarrow 0 \\ B \rightarrow \infty}} P_{J\text{-rotor}} = \rho \Omega \Gamma \int_0^R v_x r dr = \rho \frac{\Omega \Gamma}{2\pi} \bar{v}_{x,d} A_d = P_{J\text{-disc}}, \quad (4.27)$$

$$\lim_{\substack{C \rightarrow 0 \\ B \rightarrow \infty}} T_{J\text{-rotor}} = \rho \Omega \Gamma R^2 - \rho \Gamma \int_0^R v_\varphi dr = T_{J\text{-disc}}. \quad (4.28)$$

So far the rotor blade and the disc still have a finite  $\Omega$ . With increasing  $\Omega$  the torque  $Q$  disappears and the load becomes normal. For constant  $P$  but  $\Omega \rightarrow \infty$ , (4.1) and (4.3) yield:

$$rf_\varphi \propto \Omega^{-1} \quad \text{and} \quad rv_\varphi \propto \Omega^{-1} \quad \text{if } \lim_{\Omega \rightarrow \infty} \mathbf{f} \cdot \mathbf{v} = \text{constant}. \quad (4.29)$$

This implies that  $f_\varphi$  and  $v_\varphi$  vanish but not  $v_\varphi \Omega r = \Omega \Gamma / (2\pi)$ . By (4.4) at the disc  $\rho \Omega \Gamma / (2\pi) = \Delta H = \Delta p$  so (4.27) and (4.28) become:

$$\lim_{\substack{C \rightarrow 0 \\ B \rightarrow \infty \\ \Omega \rightarrow \infty}} P_{J\text{-rotor}} = \rho \Delta p \bar{v}_{x,d} A_d = P_{Froude \text{ disc}} \quad (4.30)$$

and:

$$\lim_{\substack{C \rightarrow 0 \\ B \rightarrow \infty \\ \Omega \rightarrow \infty}} T_{J\text{-rotor}} = \rho \Delta p A_d = T_{Froude \text{ disc}}. \quad (4.31)$$

Herewith a Joukowsky rotor with  $B$  blades has been transferred to Froude's disc with a constant pressure jump  $\Delta p$  by the limits  $C \rightarrow 0$ ,  $B \rightarrow \infty$  and  $\Omega \rightarrow \infty$ .

#### 4.4. Comparison of the flow fields of a disc and rotor

In the previous sections we showed the conformity of the loads and power conversion by a rotor and an actuator disc. However, this does not yet include the development of the wake behind both. An experimental analysis compares the wake development of a 2-bladed model rotor and of an actuator disc tested in identical circumstances: the same wind tunnel, wind speed and turbulence level, size of rotor and disc, Reynolds number and thrust coefficient. This experimental comparison is entirely based on Lignarolo et al. (2016a)<sup>2</sup>.

A porous disc<sup>3</sup> and a two bladed horizontal axis wind turbine model running at tip speed ratio  $\lambda = 7$ , both with a 0.6m diameter, have been tested in the low speed closed loop Open Jet Facility at a wind speed of 4.7m/s. The OJF is a wind tunnel located at Delft University of Technology, faculty Aerospace Engineering. It has an octagonal test section with an equivalent diameter of 3 m and a contraction ratio of 3:1, delivering a uniform stream with about 0.5% turbulent intensity up to 1m from the nozzle and lower than 2% at 6m from the nozzle exit. The disc and turbine model have been tested in identical conditions with identical measurement systems, described in Lignarolo et al. (2016a). This paper presents a comprehensive analysis of both experiments, while here only the data on the axial velocity and the wake expansion are reproduced. The thrust coefficient  $C_T = -0.93$ .

Figure 4.3 shows the axial velocity  $v_x$  of the disc (AD) flow field and the azimuthally averaged  $v_x$  of the wind turbine (WT) flow field. The area between  $x = 0.15D$  and  $.55D$  could not be covered by the SPIV (Stereo Particle Image

<sup>2</sup>The authors of this paper have given permission to include their results in this book.

<sup>3</sup>A porous disc changes  $H$  by dissipation and heat exchange, instead of changing angular momentum or swirl. However, as shown in section 4.3, swirl disappears for  $\Omega \rightarrow \infty$ , so a porous disc represents the Froude disc at the right-hand sides of (4.30) and (4.31). The difference is in the origin of the disc force field: an externally applied force field for Froude's disc, versus the viscous drag for the porous disc, and the type of extracted energy:  $Q\Omega$  with  $Q \rightarrow 0$ ,  $\Omega \rightarrow \infty$  for Froude's disc, heat for the porous disc.

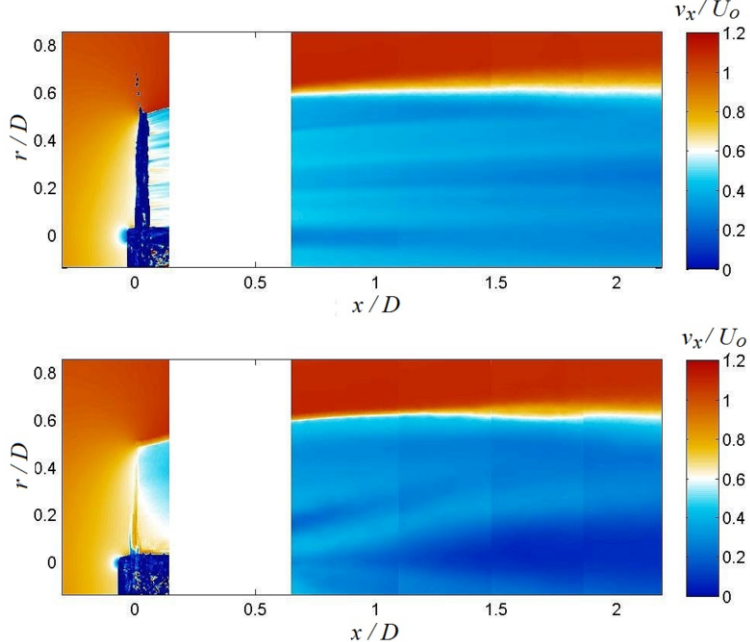


Figure 4.3: Axial velocity field in the wake of the AD (top) and of the WT (bottom), both operating at  $C_T = -0.93$ .

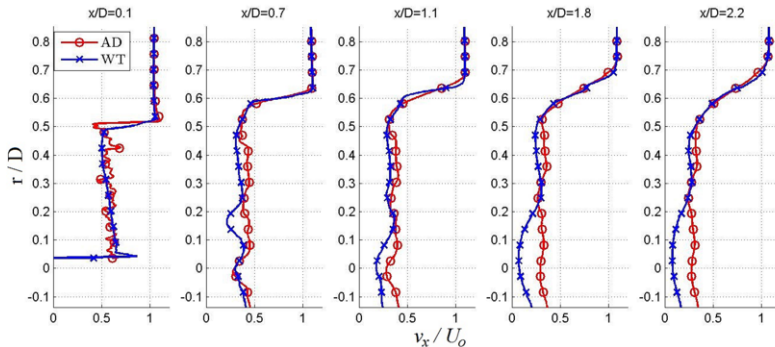


Figure 4.4: Axial velocity profiles at five different locations in the wake of the AD and of the WT.

Velocimetry) system, so no data are available. Figure 4.4 shows the radial distribution of  $v_x$  at several positions downstream of the plane of the AD-WT. Finally figure 4.5 shows the wake expansion behind the AD and WT. Figures 4.3, 4.4 and 4.5 show a good correspondence between the AD and WT results.

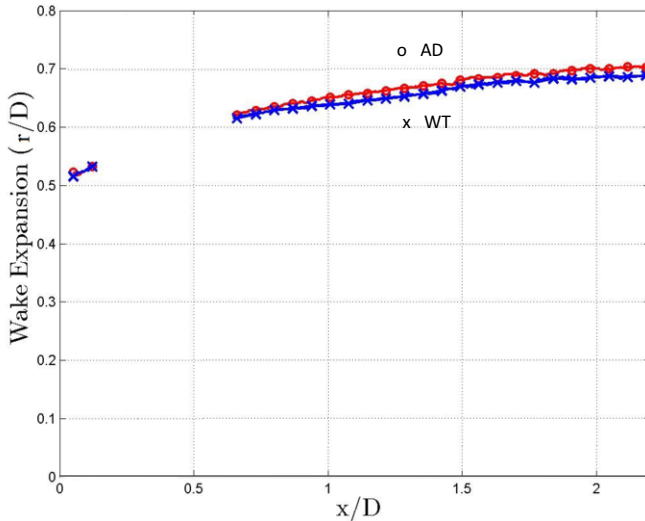


Figure 4.5: ADs and WTs wake expansion and relative difference. The curves represent the loci of the points where the axial velocity is 99% of the free stream value.

Next to this experimental comparison, section 8.3 presents a numerical comparison of the velocity distribution in the plane of a 3-bladed rotor with the velocity in the plane of an actuator disc. This numerical exercise uses the results of the Lifting Line and Actuator Line methods described in section 2.3 and the results of the actuator disc method described in chapter 5 and 6, so the presentation of the results is postponed to chapter 8.

#### 4.5. Evaluation

Research question Q5 listed in section 1.4 has been answered. The expressions for the thrust and power for a Joukowsky rotor and disc are similar. A Joukowsky rotor becomes the classical Froude disc with a uniform load after a series of limit transitions. The power converted by the actuator disc as well as the rotor shows itself as a change of the Bernoulli value  $H$ , being equal to the change in the angular momentum times rotational speed.

Question Q6 has been answered positively by experiments with a wind turbine disc and rotor having the same size and thrust, tested in the same wind tunnel. The flow of a disc and rotor resemble enough to be confident that the disc can be used for analyses of rotors with a finite number of blades. Chapter 5 treats the performance of a Froude disc, chapter 6 of a Joukowsky disc.

## Analysis of Froude's actuator disc flows

### 5.1. Introduction

This chapter addresses the actuator disc as conceived by [Froude \(1889\)](#): a disc with a uniform normal load created by a pressure jump over the disc, with the disc placed perpendicular to a uniform inviscid flow. As shown in chapter 4 such a disc is the end product after a series of limit transitions starting with a rotor having a finite rotational speed and finite number blades. The momentum theory couples the disc load to the acceleration or deceleration of the flow in the fully developed wake, allowing for optimisation of the action of the disc. This actuator disc momentum theory, sometimes called ‘one-dimensional’ as only the axial momentum balance is included, is repeated in section 5.2.2. The theory gives the average value of the axial velocity at the disc, not the velocity distribution. Modern computational approaches are able to provide flow details like the shape and strength of the vortex tube that separates the wake from the outer flow. Using a Computational Fluid Dynamics (CFD) solver for the Navier-Stokes equations, the velocity field for propeller as well as wind turbine flows states was published by [Sørensen et al. \(1998\)](#), and for a static or hovering disc by [Spalart \(2003\)](#). The method to find details of the actuator disc flow used in this chapter is based on the inviscid method of [Øye \(1990\)](#), aiming for such a high numerical accuracy that conclusions may be drawn supporting or rejecting analytical treatments.

First section 5.2 presents the axial momentum theory with and without conservative force. In section 5.3 the numerical method is explained where-after in section 5.4 flow details are investigated like the shape and strength of the wake boundary vortex sheet, the distribution of the pressure and velocity at the disc and in the wake, the inflection points in the streamlines passing the disc and the role of the pressure in the momentum balance. The chapter is based on the papers by [van Kuik and Lignarolo \(2016\)](#) and [van Kuik \(2018\)](#).

### 5.2. One-dimensional momentum theory

**5.2.1. The momentum balance.** The general expression for the momentum balance is given by [Batchelor \(1970, p. 138\)](#). For inviscid flow the balance in  $x$ -direction drawn on a volume  $V$  enclosed by a surface  $S$ :

$$T - \oint_S \mathbf{e}_x \cdot \mathbf{e}_n p dS = \rho \oint_S v_x (v_x - U_0) dS \quad (5.1)$$

with  $p$  being the pressure acting at the boundary  $S$ . According to section 2.5.3 the pressure integral represents a conservative contribution, but when applied to the stream tube passing through the disc the integral becomes zero, as will be

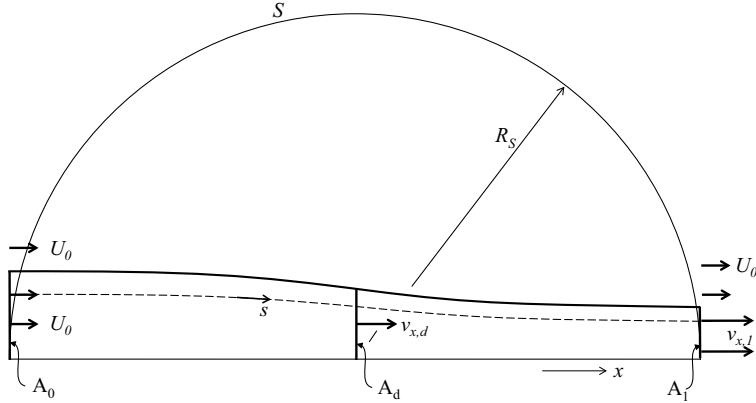


Figure 5.1: Sphere with surface  $S$  as control volume for the momentum balance, crossing the stream tube of an actuator disc far upstream with undisturbed flow, and far downstream with a fully developed wake. Only half of the cross section is displayed.

shown in the next section. Sections 5.2.3 and 5.2.4 treat the balance including conservative contributions, e.g. when the balance is applied per annulus instead entire stream tube.

Usually the stream tube passing through the actuator is used as the control volume  $V$ . Several proofs have been published that the pressure acting at the stream tube boundary does not contribute to the momentum balance, e.g. by Thoma (1925). Here another control volume is used, equivalent to figure 2.5b: figure 5.1 shows the control volume bounded by a sphere with radius  $R_S$ , with the centre of the sphere coinciding with the centre of the actuator disc. The advantage of this control volume is that only the flow conditions at infinite distance need to be known, not at the vortex sheet itself. Furthermore this control volume can be used for the flow induced by a static disc which does not have a stream tube.

Outside the wake of the actuator disc at a large distance from the origin, the flow can be considered as a summation of a parallel flow and a source/sink flow. Analogous to Batchelor (1970, p. 351) momentum and pressure terms in (5.1) at the sphere  $S$  but outside the wake vanish for  $R_S \rightarrow \infty$ . This is because the summation of undisturbed  $U_o$  and source/sink induced velocities  $v$  gives rise to momentum flux and pressure terms containing  $U_o^2$ ,  $vU_o$  and  $v^2$ . The source/sink velocity vanishes like  $R_S^{-2}$  by continuity of mass, so the  $v^2$  term does not contribute after integration on  $S$  for  $R_S \rightarrow \infty$ . The same holds for the constant term containing  $U_0^2$ . The mixed terms containing  $vU_o$  do not vanish for increasing  $R_S$  but do not contribute after integration on  $S$ , due to the symmetry of the source/sink flow with respect to the plane  $x = 0$ . What remains for  $R_S \rightarrow \infty$  are the contributions by the disc itself and the momentum transport at stream tube cross sections  $A_0$  far upstream and  $A_1$  far downstream. The pressure acting at these cross sections is undisturbed,  $p_0$ , so the pressure integral in (5.1) vanishes. As Froude's disc has a constant pressure jump  $\Delta p$  the momentum balance

becomes:

$$\Delta p A_d = \rho \int_{A_1} v_{x,1} (v_{x,1} - U_0) dA_1. \quad (5.2)$$

The same result is obtained when we use the stream tube as control volume, and assume that the pressure at the stream tube boundary does not result in an axial force acting on the control volume. In other words: the momentum balance using the sphere as control volume confirms this assumption, so it may be considered as an indirect proof that the stream tube pressure does not contribute.

**5.2.2. Momentum theory without conservative forces.** The Bernoulli equation applied to the upstream and downstream part of a streamline (the dashed line in figure 5.1) can be coupled by the pressure jump  $\Delta p_d$ , giving:

$$\Delta p_d = \frac{1}{2} \rho (v_{x,1}^2 - U_0^2). \quad (5.3)$$

As  $\Delta p_d$  is uniform, also the velocity in the wake  $v_{x,1}$  is uniform so (5.2) becomes:

$$\Delta p_d A_d = \rho v_{x,1} (v_{x,1} - U_0) A_1. \quad (5.4)$$

Mass conservation gives  $\bar{v}_{x,d} A_d = v_{x,1} A_1$  where  $\bar{v}_{x,d}$  is the velocity averaged on the disc area. Elimination of  $\Delta p_d$  from (5.3) and (5.4) gives the famous result, first obtained by Froude (1889):

$$\bar{v}_{x,d} = \frac{1}{2} (v_{x,1} + U_0). \quad (5.5)$$

The converted power  $P = \Delta p_d \bar{v}_{x,d} A_d$  so in dimensionless form the power coefficient is:

$$C_p = \frac{P}{\frac{1}{2} \rho U_0^3 A_d} = \frac{1}{2} \left( \left( \frac{v_{x,1}}{U_0} \right)^2 - 1 \right) \left( \frac{v_{x,1}}{U_0} + 1 \right) \quad (5.6)$$

or, expressed in  $\bar{v}_{x,d}$ :

$$C_p = 4 \left( \frac{\bar{v}_{x,d}}{U_0} \right)^2 \left( \frac{\bar{v}_{x,d}}{U_0} - 1 \right). \quad (5.7)$$

The thrust coefficient becomes:

$$C_T = \frac{T}{\frac{1}{2} \rho U_0^2 A_d} = 4 \frac{\bar{v}_{x,d}}{U_0} \left( \frac{\bar{v}_{x,d}}{U_0} - 1 \right). \quad (5.8)$$

Differentiation of (5.7) to  $\bar{v}_{x,d}$  to find the coefficient for maximum of power extraction gives:

$$C_{p,max} = -\frac{16}{27} \text{ for } \frac{\bar{v}_{x,d}}{U_0} = \frac{2}{3} \quad (5.9)$$

which was obtained by Joukowsky and Betz in 1920. The minus sign indicates that the energy is taken from the flow.

For the static disc  $U_0 = 0$  so  $C_p$  loses its meaning. To cover the entire regime of the disc it is common to non-dimensionalise velocities by the velocity at the disc when  $U_0 = 0$ . The combination of (5.4) and (5.5) gives  $\bar{v}_{x,d} = \sqrt{T/(2\rho A_d)}$  which is used in figure 1.2. The power  $P = T \bar{v}_{x,d}$  required to keep the disc static or a helicopter hovering is:

$$P = 2\rho A_d \bar{v}_{d,x}^3 = \sqrt{\frac{T^3}{2\rho A_d}} \quad (5.10)$$

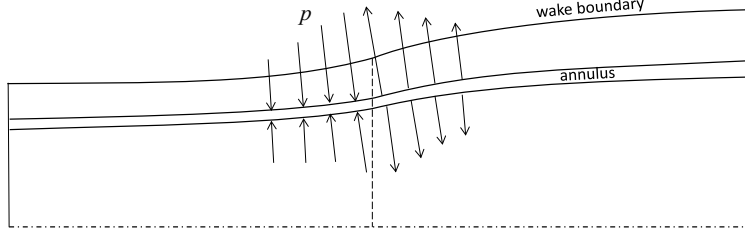


Figure 5.2: The annulus as control volume for the momentum balance, including the contribution of the pressure at the surface of the annulus.

corresponding to equations 17 and 19, p. 143, in the French translation of Joukowsky (1918)<sup>1</sup>.

**5.2.3. Momentum theory including conservative forces.** In the previous section the momentum balance is applied to the entire stream tube, with the disc load as the only load entering this balance. Now it is assumed that the pressure integral in (5.1) is  $\oint_S \mathbf{e}_x \cdot \mathbf{e}_n p dS \neq 0$ . This contribution acts as a conservative force as discussed in section 2.5.3. Furthermore the thrust may contain a conservative component  $T_{cons,d}$ . Herewith the momentum balance becomes:

$$T_{non-cons} + T_{cons} = \rho \oint_S v_x (v_x - U_0) dS \quad (5.11)$$

with:

$$\left. \begin{aligned} T_{non-cons} &= \Delta p A \\ T_{cons} &= T_{cons,d} - \oint_S \mathbf{e}_x \cdot \mathbf{e}_n p dS. \end{aligned} \right\} \quad (5.12)$$

The energy equation (5.3) is unaffected by  $T_{cons}$  so the combination of (5.11) with (5.4) gives:

$$\overline{v_{x,d}} = \left( \frac{T_{cons}}{T_{non-cons}} + 1 \right) \frac{U_0 + v_{x,1}}{2}. \quad (5.13)$$

Expression (5.7) for the power coefficient becomes:

$$C_p = \left( \frac{T_{cons}}{T_{non-cons}} + 1 \right) C_{p,T_{cons}=0} \quad (5.14)$$

and for the thrust coefficient:

$$C_T = C_{T_{cons}} + C_{T_{non-cons}} \quad (5.15)$$

Equations (5.13) and (5.14) have first been derived by van Holten (1981) for discs or rotors placed in a shroud or ring wing. The lift on the ring wing contributes thrust  $T_{cons,d}$  to the momentum balance but does not convert energy. The average axial velocity at the disc is then given by (5.13). When both thrust components have the same sign the average velocity increases and so does the power coefficient.

<sup>1</sup>Please note that the translation uses a reversed notation:  $P$  for thrust,  $T$  for power.

Sørensen (2015, section 3.4) presents a survey of recent publications on the so-called diffuser-augmented wind turbines and discusses the associated momentum theory in detail.

**5.2.4. Momentum theory applied per stream annulus.** Equation (5.13) has also been derived by Sørensen and Mikkelsen (2001) and is included in Sørensen (2011) although they, as well as van Holten (1981), did not use the classification *cons* and *non – cons*. Sørensen and Mikkelsen (2001) derived (5.13) for the momentum theory applied to a stream annulus instead of stream tube. A stream annulus is a part of the stream tube, e.g. the volume bounded by the stream line shown as a dashed line in figure 5.1 or the volume between two such stream lines passing the disc at radii  $r$  and  $r + \Delta r$  as shown in figure 5.2. Such a volume is called an annulus. Applying the momentum balance to an annulus can only be done with the volume of the annulus as control volume, by which (5.2) becomes:

$$\Delta p_d A_{d,ann} + \int_{ann} \mathbf{e}_x \cdot \mathbf{e}_n p dS_{ann} = \rho \int_{A_1} v_{x,1} (v_{x,1} - U_0) dA_{1,ann}, \quad (5.16)$$

where  $S_{ann}$  is the surface of the annulus,  $A_{d,ann}$  and  $A_{1,ann}$  the cross sections of the annulus with the disc and far wake, and  $\mathbf{e}_n$  the unit vector normal to  $S_{ann}$ . With  $T_{cons} = T_d = \Delta p_d A_{d,ann}$  and  $T_{non\ cons} = T_{ann} = \int \mathbf{e}_x \cdot \mathbf{e}_n p dS_{ann}$ :

$$\overline{v_{x,d}} = \left( \frac{T_{ann}}{T_d} + 1 \right) \frac{U_0 + v_{x,1}}{2}, \quad (5.17)$$

equivalent to (5.13). In section 5.4.5, equation (5.17) will be verified by a numerical evaluation of the momentum theory applied to annuli.

### 5.3. Numerical assessment of Froude's actuator disc performance

In order to supplement the results of the momentum theory with flow details like the velocity and pressure distributions at the disc and in the wake, van Kuik and Lignarolo (2016) developed a numerical potential flow code which calculates the position and strength of the wake for a prescribed axial disc load. With the wake known, all flow details can be calculated. The potential flow model of the wake is described in detail in appendix D, so here only a summary is presented.

**5.3.1. The model and accuracy of computation.** The disc generates a cylindrical vortex sheet with expanding or contracting diameter, emanating from the disc edge as shown in figure 5.3 for an energy extracting disc. The cylindrical sheet stretches from the disc to downwind infinity, and separates the flow that has passed the disc from the flow outside this stream tube. The numerical implementation of the vortex sheet splits the sheet in two parts.

- The fully developed far wake has a constant radius  $R_1$  and is modelled as a semi-infinite vortex tube with constant  $\gamma = \mathbf{e}_\varphi \gamma_1 = \mathbf{e}_\varphi (-U_0 + \sqrt{2\Delta p + U_0^2})$  starting at  $x = 30R_1$ . An analytical solution for the axial velocity induced by this semi-infinite tube has been derived by van Kuik and Lignarolo (2016) and a solution including the axial and radial velocity by Branlard and Gaunaa (2015). The properties of this far wake do not change during the iteration process towards a converged solution.

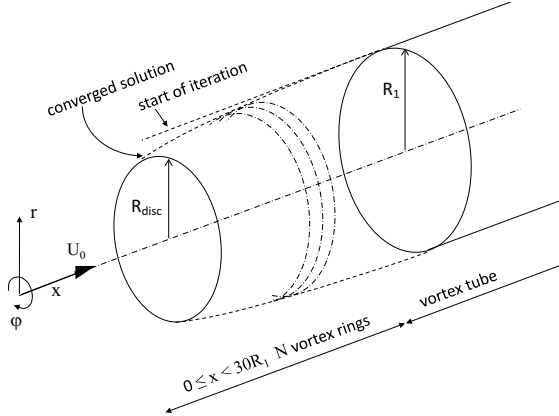


Figure 5.3: The vortex model. The far wake has a constant radius during the convergence process, while the vortex rings adapt their radii and strength. The first vortex ring coincides with the disc edge.

- From the disc position  $x = 0$  up to  $x = 30R_1$  the sheet is discretised using  $N$  vortex rings with strength  $\Gamma(i)(x(i), r(i))$ ,  $1 \leq i \leq N$ , like in the model of Øye (1990). The velocity close to the vortex ring core is de-singularised by adopting a core with radius  $\delta$ . The boundary conditions defining the radius and strength of each ring are: 1- the sheet is force free; 2- Stokes' stream function  $\Psi$  is constant or the normal velocity  $v_n = 0$ . The iteration starts with all rings having equal radius  $r(i) = R_1$ , and vortex sheet strength  $\Gamma(i)/\Delta s(i) = \gamma_1$  where  $\Delta s(i)$  is the distance between the cores of ring  $(i+1)$  and  $(i)$ . In each iteration the radius and strength of the rings are adapted to decrease the deviation from the boundary conditions until these are satisfied.

Appendix D gives details of the convergence scheme, the verification of the model, a sensitivity analysis for the model parameters  $N$  and  $\delta$ , and an assessment of the accuracy. The conclusions are repeated here:

- The vortex model is verified by comparison with an analytical solution of the semi-infinite vortex tube, yielding deviations in local velocity vectors less than 2 % for  $N = 6909$ ,  $\delta = 0.0001$ , except for the velocity component normal to the vortex sheet within a distance  $0.02R_{tube}$  from its leading edge
- Solutions converged to a constant stream function  $\Psi$  have similar deviations in normal velocity. By comparing these with solutions converged to  $v_n \leq 0.0002U_0$  it has been shown that calculated flow properties differ less than 3 %, except for  $\gamma$  deviating up to a few % for  $s/R_d < 0.13$ , with  $s$  measured from the disc edge.
- By this uncertainty in  $\gamma$  or  $v_n$  close to the disc edge, accurate quantitative conclusions with respect to the vortex sheet strength close to the disc edge are not possible. Qualitative conclusions are possible as the accuracy is limited to a few %. It has an effect of  $\leq 3\%$  on other flow parameters,

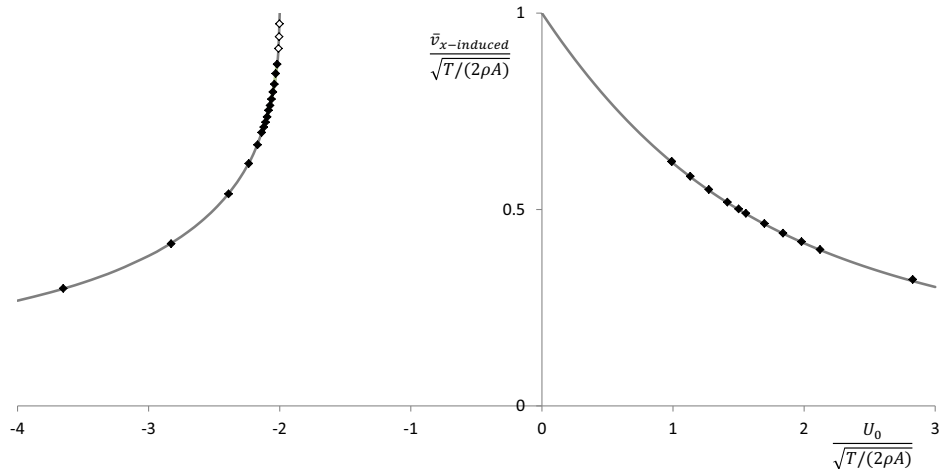


Figure 5.4: Comparison of momentum theory (—) and computed induced velocity at the disc indicated by a ♦ and ◊. Most data have been calculated with  $N = 4656$  and  $d = 0.001$ , some with  $N = 6909$  and  $d = 0.0001$ . The data displayed by a ◊ do not have the required accuracy.

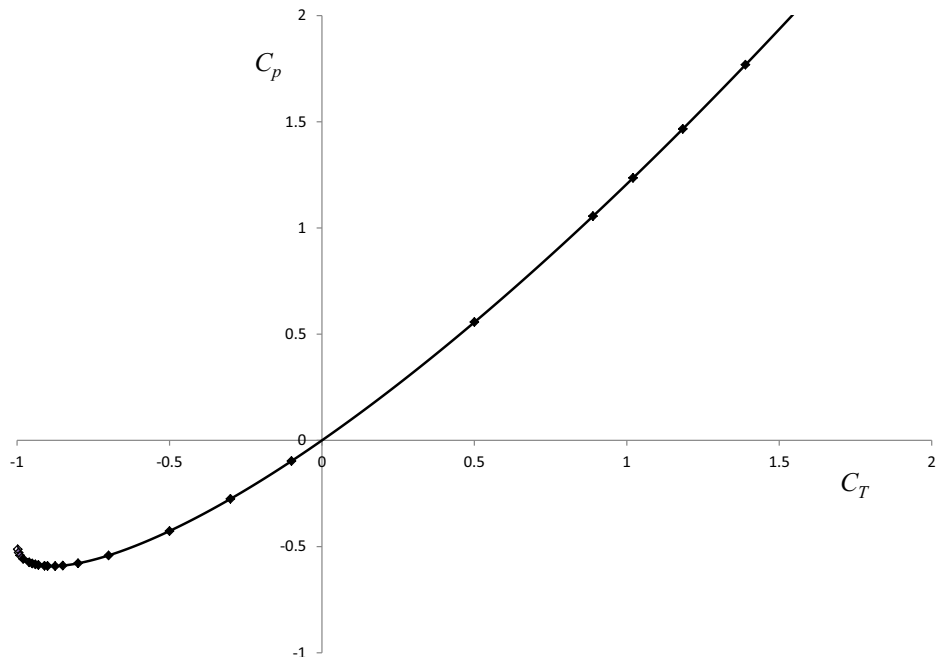


Figure 5.5: Comparison of momentum theory (—) and computed  $C_p$  as a function of  $C_T$ . For explanation of the symbols, see the previous figure.

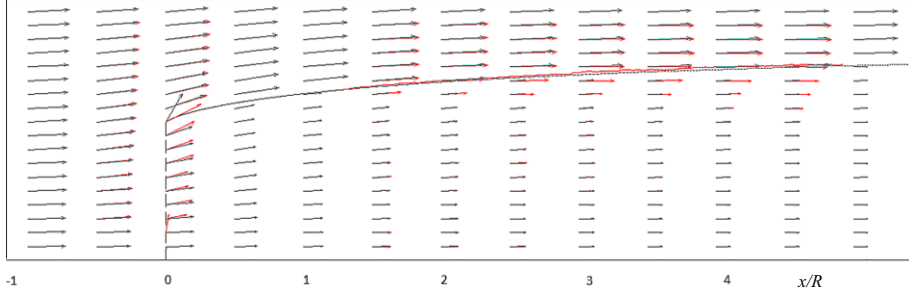


Figure 5.6: Comparison of the calculated (black) velocities and wake expansion with the measured values (red) for  $C_T = -0.93$

- The results are, with deviations of 2 %, insensitive to variations in  $N$  and  $\delta$ . The smoothness of the wake boundary vorticity distribution increases with higher  $N$ .
- The overall accuracy is assessed at 3 % except for flow details within a distance of  $0.13R_d$  from the disc edge.
- For thrust coefficients  $-1 < C_T < -0.96$ , the required accuracy is not achieved, see the results in figure 5.4 indicated with a  $\diamond$ .

**5.3.2. Comparison of calculated performance with momentum theory results.** Figures 5.4 and 5.5 show the calculated performance in terms of the induced velocity at the disc, for wind turbine and propeller discs, and the efficiency for wind turbine discs. The results of the actuator disc momentum theory are reproduced accurately:

- for  $C_T = -8/9$  or  $U_0/\sqrt{T/(2\rho A)} = -2.12 R_d/R_1$  deviates  $< 1\%$ , the induced velocity and  $C_p$  2.5%, with the boundary conditions satisfied within 1%.
- for  $C_T = 16/9$  or  $U_0/\sqrt{T/(2\rho A)} = 1.5$  the same data are: 0.4, 3, 1 %

These flow cases have been chosen for further analyses of flow details in section 5.4 as, according to momentum theory, the absolute value of the average induction at the disc and in the wake is the same:

- $C_T = -8/9$  gives  $\bar{v}_i/U_0 = -1/3$  and  $\gamma_1/U_0 = -2/3$ ,
- $C_T = 16/9$  gives  $\bar{v}_i/U_0 = +1/3$  and  $\gamma_1/U_0 = +2/3$ .

As figure 5.4 shows, no solutions are available for low but positive values of  $U_0/\sqrt{T/(2\rho A)}$ . This is due to the convergence scheme as with the radial displacement of the vortex ring cores it is not possible to converge to a wake boundary with an increasing slope for decreasing  $U_0/\sqrt{T/(2\rho A)}$ .

**5.3.3. Comparison with experimental results.** The actuator disc experiment of Lignarolo et al. (2016a) described in section 4.4 provides the flow field measured by Stereo Particle Image Velocimetry (SPIV). The disc has a diameter of 0.6m and is realised with three layers of fine metal mesh, with a total porosity (open to total area) of 32%, resulting in a measured  $C_T = -0.93$ . The comparison of the measured velocities and wake expansion with the calculated

values is shown in figure 5.6 taken from Lignarolo et al. (2016b). The SPIV measurements did not cover the region immediately behind the disc. Furthermore the disc in the experiment was mounted at a nacelle, by which the vectors near the disc centre do not match. The experimental wake expansion shown in the figure is determined as the position where  $|v|$  equals  $0.99U_0$ . The measured and calculated velocity vectors and wake expansion match very well.

## 5.4. Flow details

**5.4.1. Flow and pressure patterns.** Figures 5.7 and 5.8 show the velocity vectors, streamlines, wake boundary and isobars for  $C_T = -8/9$  and  $16/9$ . All other flow states show similar patterns. The isobars show a continuous pressure at the wake boundary, but a discontinuous pressure gradient.

**5.4.2. Properties of the wake boundary.** A steady actuator disc with a uniform load  $e_x\Delta p$  creates a wake in which the Bernoulli constant is uniform. This becomes clear by applying Bernoulli's law separately to a the up- and downstream part of a streamline passing the disc, and combining both by the pressure jump. It also follows from (2.3) which reduces in the wake to  $\nabla H = 0$ . Upstream of the disc and outside the wake also  $\nabla H = 0$ . The difference  $\Delta H$  follows from the combination of (2.3) and (2.4) for an infinitely thin disc, giving  $\Delta H_d = F = \Delta p_d$ , and for the wake boundary:

$$\Delta \left( \frac{1}{2} \rho |v|^2 \right) = \Delta H \quad (5.18)$$

as the vortex sheet forming the wake boundary is force free. With  $\gamma = (v_- - v_+)$  denoting the strength of the vortex sheet,  $v_-$  and  $v_+$  the velocities at the wake side and outer side of the sheet and  $v_s = \frac{1}{2}(v_- + v_+)$  the velocity of the sheet, (5.18), becomes:

$$\rho v_s \gamma = \Delta H = \text{constant} \quad (5.19)$$

or:

$$\frac{v_s \gamma}{v_{s,1} \gamma_1} = 1. \quad (5.20)$$

For a disc accelerating the flow, the velocity of the vortex sheet  $v_s$  increases to  $v_{s,1}$  when going downstream, so  $\gamma/\gamma_1$  decreases to become 1 in the far wake. As  $\gamma$  is positive the maximum value is at the leading edge of the sheet. For a disc decelerating the flow the opposite is true: as  $v_s/v_{s,1}$  decreases when going downstream,  $\gamma/\gamma_1$  increases with a minimum value of  $\gamma/\gamma_1$  at the leading edge. As  $\gamma_1$  is negative, this implies that  $\gamma$  reaches a maximum at the leading edge. However, this reasoning assumes that the velocity of the sheet is in- or decreasing everywhere along the sheet, so  $d\gamma/ds \neq 0$  along the sheet. Figure 5.9 shows the calculated distribution  $\gamma(s)$ . For  $C_T = 16/9$  the above reasoning is confirmed: the maximum value of  $\gamma$  is at  $s = 0$ . For the flow decelerating case  $C_T = -8/9$  the maximum of  $\gamma$  occurs at  $s/R_d = 0.0513$ . In both cases the distribution tends to become singular for  $s/R_d \rightarrow 0$  but with a different slope  $d\gamma/ds$ : for positive  $C_T$   $d\gamma/ds < 0$  at  $s = 0$ , while  $d\gamma/ds > 0$  at  $s = 0$  for negative  $C_T$ . Using (5.20) this implies that in the flow accelerating case  $v_s$  increases smoothly from the disc edge to the far wake, but in the flow decelerating case  $v_s$  increases immediately after

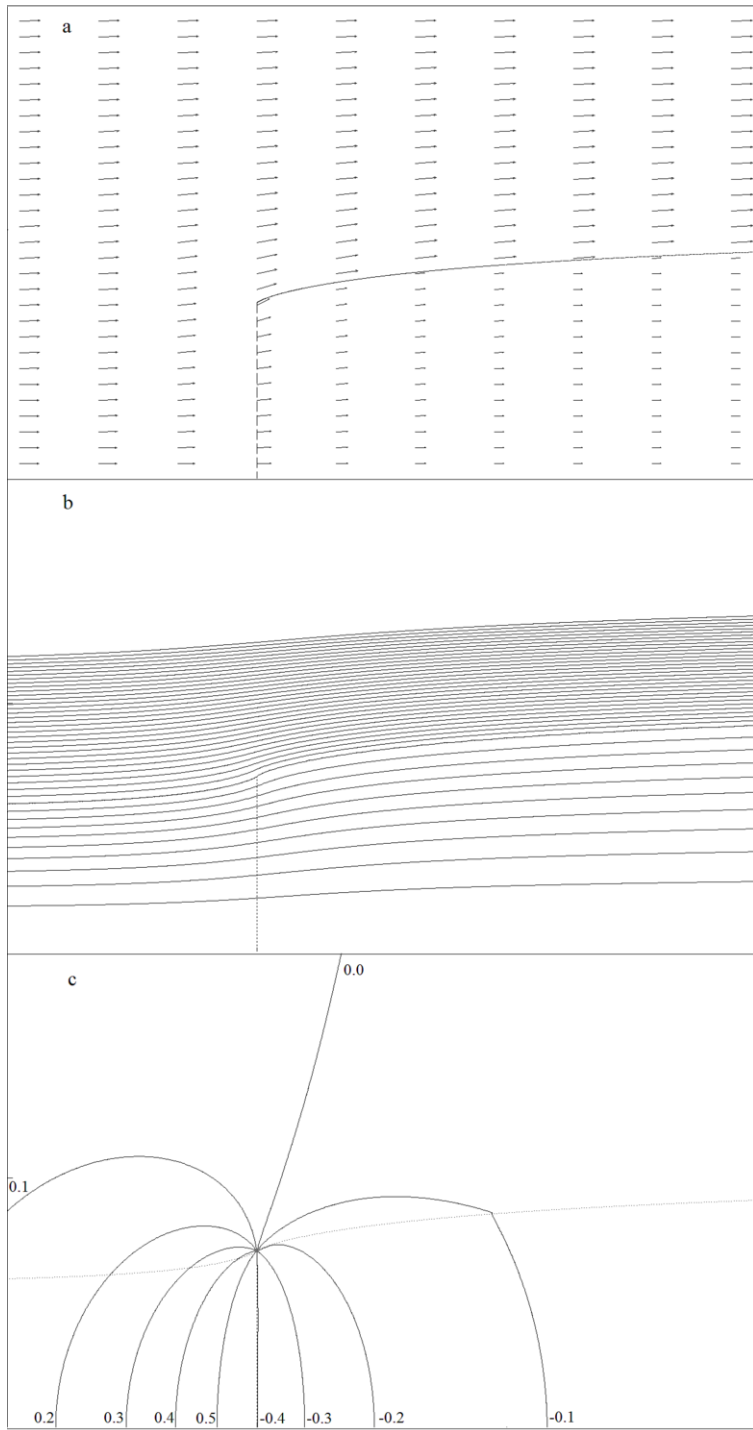


Figure 5.7: For  $C_T = -8/9$ : (a) shows the velocity field and wake boundary, (b) stream tube value  $\Psi/\Psi_1$ , (c) isobars  $(p - p_0) / |\Delta p_d|$ , both with increments of 0.1.

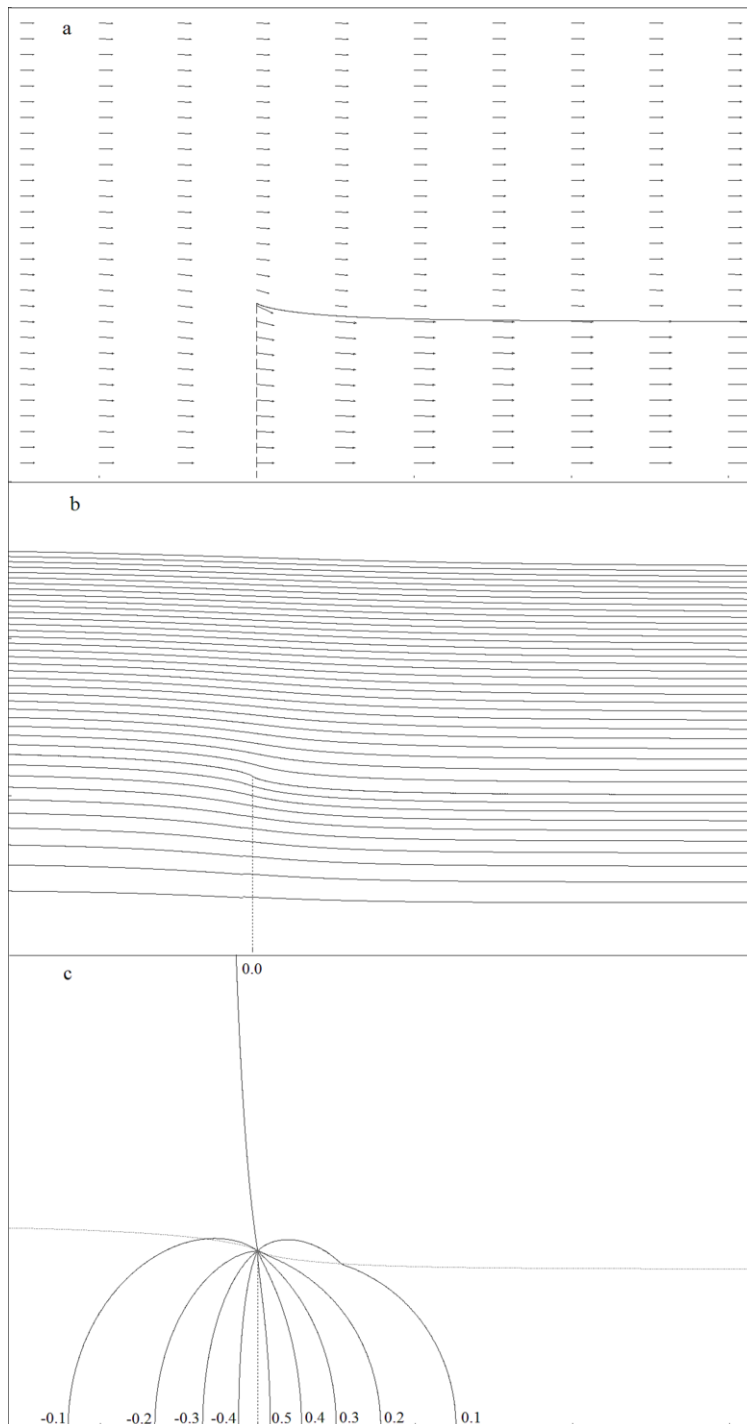


Figure 5.8: For  $C_T = 16/9$ : (a) shows the velocity field and wake boundary, (b) stream tube value  $\Psi/\Psi_1$ , (c) isobars  $(p - p_0) / |\Delta p_d|$ , both with increments of 0.1.

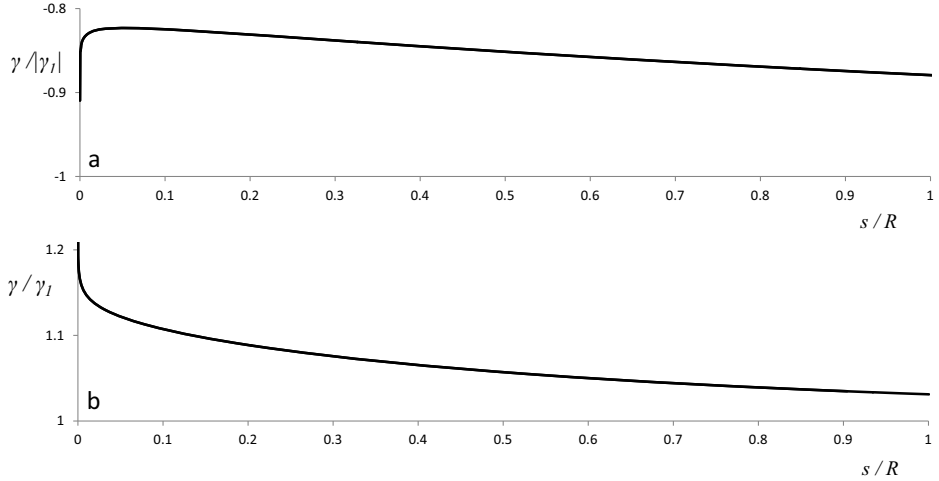


Figure 5.9: The distribution  $\gamma(s)$  for a:  $C_T = -8/9$ , b:  $C_T = 16/9$ .

$s = 0$  reaching a maximum value at a small distance behind the disc, where-after  $v_s$  decreases until  $v_{s,1}$  is reached in the far wake.

Despite the differences between the vortex sheet development for propeller and wind turbine discs, the vortex sheet characteristics at the leading edge of the sheet are similar. For all flow cases the shape of the vortex sheet close to its leading edge is somewhat curved but does not show a particular behaviour. For wind turbine discs the slope of the vortex sheet at  $x = 0$  is always less than  $90^\circ$  so the sheet does not turn upwind of  $x = 0$ . For  $C_T = -0.998$  the slope is  $65^\circ$ , for  $C_T = -8/9$  it is  $46^\circ$ . For all calculated propeller disc flows the same holds, with a slope  $-30.5^\circ$  for  $C_T = 16/9$ . For very high values of  $C_T$ , as in case of a static disc ( $U_0 = 0$ ), the vortex sheet is known to turn upwind, see e.g. [Spalart \(2003\)](#). The strength of the vortex sheet seems to exhibit a singular behaviour at the disc leading edge as shown in figure 5.9. For  $s \rightarrow 0$  the strength  $|\gamma|$  tends to go to  $\infty$ , but as discussed in appendix D the uncertainty in local flow properties close to the disc edge is a few %. Consequently it is not possible to draw quantitative conclusions with respect to the singular behaviour.

The numerical solution does not resemble the two-dimensional solution published by [Schmidt and Sparenberg \(1977\)](#). They have derived a 2-D solution of an infinite vortex sheet carrying a constant jump in Bernoulli value  $H$ . This solution is a  $45^\circ$  spiral (the tangent is at  $45^\circ$  with the radial vector in all positions) with constant  $\gamma$ . Both properties are not present in the calculated potential flow solution. [van Kuik \(2009\)](#) showed that their spiral is a particular member of a family of vortex sheet spirals developed by [Prandtl \(1924\)](#). These spirals are defined at a Riemann surface instead of a plane 2-D surface, see [van Kuik \(2004\)](#), so do not represent a 2-D solution.

**5.4.3. Pressure and velocity distribution at the disc.** The isobar patterns shown in figures 5.7 and 5.8 seem to indicate that the pressure at the disc

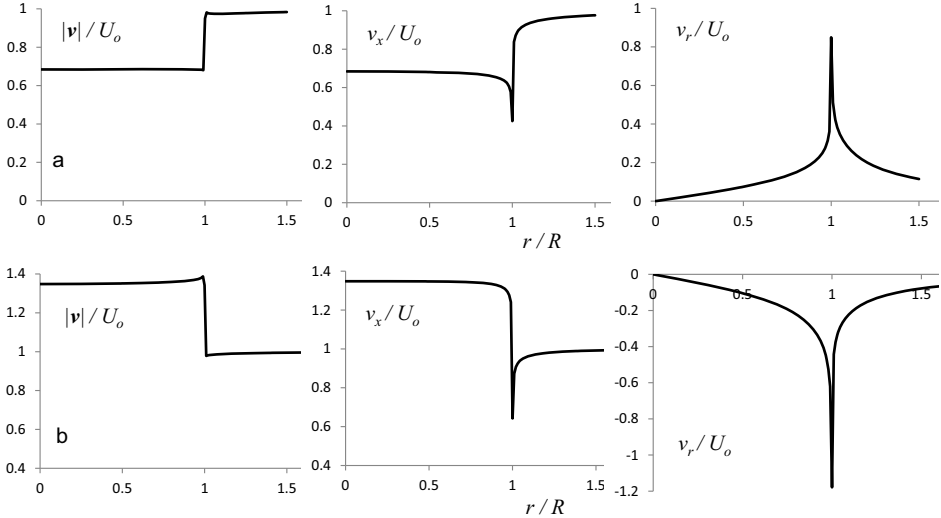


Figure 5.10: The velocity components at  $x = 0$  for a:  $C_T = -8/9$ , b:  $C_T = 16/9$ .

is uniform for  $C_T = -8/9$  but non-uniform for  $C_T = 16/9$ . A close examination of the pressure data confirms this. When the pressure at the disc is constant the absolute value of the velocity at the disc will be constant, based on Bernoulli's law. The velocity components at the disc are shown in figure 5.10, confirming that the absolute value of  $v_s$  is constant (with a deviation of  $\pm 2\%$ ) for  $C_T = -8/9$  while  $v_s$  increases 2.3% from  $r = 0$  to  $r/R = 0.98$  for  $C_T = 16/9$ . The same behaviour is found for other values of  $C_T$ . To explain the constant velocity and pressure at the flow decelerating disc, the radial component of the (steady version of the) equation of motion (2.1) is helpful:

$$\rho v_s \frac{\partial v_r}{\partial s} = - \frac{\partial p}{\partial r}. \quad (5.21)$$

As the disc force field is only axial,  $f$  is absent in (5.21). When following a stream line passing the disc and observing the in- or decrease of  $v_r$ , the following observations are made for a disc *decelerating* the flow:

- (i) when the position of observation  $s^*$  travels along a stream line from far upstream,  $s_0$ , to the disc position  $s_d$ ,  $v_s$  increases due to the decreasing distance to the vorticity  $\gamma$  in the wake boundary. The induction becomes stronger when the distance decreases, so  $\partial v_r / \partial s > 0$ .
- (ii) following the streamline in the wake, so with  $s^* > s_d$ , two regions can be distinguished: the wake downstream of the disc up to the position of observation  $s^*$ , and the wake downstream of  $s^*$ . The vorticity between  $s_d$  and  $s^*$  induces a negative  $v_r$  which increases for increasing  $s^*$ , so contributes to  $\partial v_r / \partial s < 0$ . The induction by the vorticity downstream of  $s^*$  does not change sign but becomes constant for large  $s^*$  so  $\partial v_r / \partial s \rightarrow 0$ .
- (iii) consequently  $\partial v_r / \partial s = 0$  at the disc itself, by which (5.21) gives  $\partial p / \partial r = 0$  and  $|v_d|$  is constant.

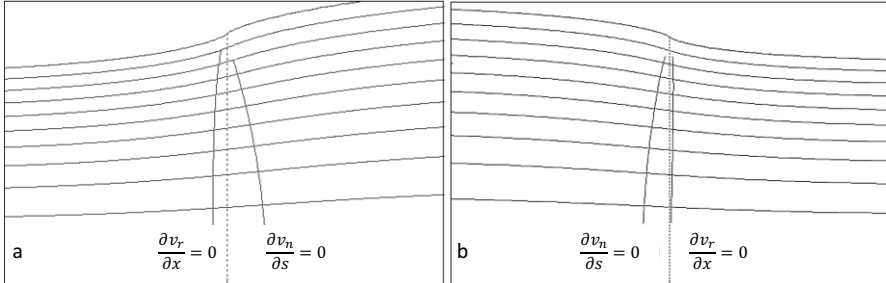


Figure 5.11: The inflection points in the streamlines for **a**:  $C_T = -8/9$ , **b**:  $C_T = 18/9$ .

This reasoning does not yet account for:

- (iv) the variation in distance from the position of observation  $s^*$  to the most nearby vorticity due to the wake expansion
- (v) the variation in the strength  $\gamma$  of the wake boundary sheet as shown in figure 5.9.

Apparently, these additional aspects support the result that  $\partial p / \partial r = 0$  for  $C_T < 0$ . However, repeating the line of arguments (i) to (iii) for positive  $C_T$  leads to a similar conclusion that  $v_s$  should be constant, which is not supported by figure 5.10. This is attributed to these additional aspects. Further discussion about the velocity at the disc is postponed to section 6.4.4 where the effect of swirl is included.

The conclusion is that:

- for discs decelerating the flow the absolute velocity at the disc is constant while the axial velocity is non-uniform
- for discs accelerating the flow the absolute and the axial velocity are non-uniform.

These results do not support the assumption mentioned in several wind turbine textbooks and papers that the axial velocity is constant. As discussed by Xiros and Xiros (2007) this is based on the expression for the vorticity being zero:

$$\omega = \frac{\partial v_r}{\partial x} - \frac{\partial v_x}{\partial r} = 0 \quad \text{for } x = 0, r < R_d, \quad (5.22)$$

combined with the assumption that the inflection points defined as  $\partial v_r / \partial x = 0$  are located at  $x = 0$ , leading to  $\partial v_x / \partial r = 0$ . Mikkelsen (2011) noted that the deflection point may be at  $x \neq 0$  which is confirmed by the present calculations. Figure 5.11 shows the positions where  $\partial v_r / \partial x = 0$  as calculated for  $C_T = 8/9$  and  $16/9$ , located upstream, respectively downstream of the disc. The explanation is that for a flow decelerating disc  $\partial v_r / \partial x$  is always lower than  $\partial v_r / \partial s$  as the wake expansion gives lower values of  $\Psi$  and  $v_r$  when moving in  $x$ -direction instead of  $s$ -direction. Consequently  $\partial v_r / \partial x = 0$  is reached at  $x < 0$ . Furthermore figure 5.11 shows where  $\partial v_n / \partial s = 0$  marking the inflection from concave or convex streamlines to convex or concave streamlines.

The conclusion that  $v_{x,d}$  is non-uniform contradicts the assumption of uniform  $v_{x,d}$  made in BEM. This assumption finds its roots in vortex models used to analyse actuator disc and rotor flows. In most vortex models it is assumed that the wake expansion may be neglected, by which analytical treatments become into reach, e.g. [Okulov and Sørensen \(2010\)](#), [Burton et al. \(2011\)](#), [Okulov et al. \(2015\)](#), [Branlard and Gaunaa \(2015\)](#), [Branlard et al. \(2014\)](#) and [Branlard \(2017\)](#). The vortex models reproduce the result of momentum theory that the averaged induced velocity at the disc is the average of the velocities far up- and downstream. However, the present analysis reveals an essential difference between the two approaches:

- for the semi-infinite vortex tube with constant radius:  $v_{x,d}$  is uniform,  
 $|\mathbf{v}_d|$  is non-uniform
- for the actuator disc extracting energy :  $v_{x,d}$  is non-uniform,  
 $|\mathbf{v}_d|$  is uniform.
- for the actuator disc adding energy :  $v_{x,d}$  is non-uniform,  
 $|\mathbf{v}_d|$  is non-uniform.

This conceptual difference is caused by the wake expansion / contraction, by which the pressure at expanding annuli acts as a conservative load, as will be treated in section 5.4.5. As long as expansion or contraction may be neglected, the vortex tube offers elegant analytical treatments providing physical insights. However, modern wind turbines operate at thrust coefficients  $|C_T| > 0.6$  at which the expansion is significant so the non-uniformity in  $v_{x,d}$  has to be taken into account.

**5.4.4. Pressure at the axis.** Figure 5.12 shows the pressure distribution at the axis for  $C_T = -8/9$  and  $C_T = 16/9$ . The pressure jump across the disc is not symmetric:  $|(p - p_0)|_{upstream} \neq |(p - p_0)|_{downstream}$ . A symmetric jump would require, by the Bernoulli equation, that at the upstream side of the disc  $\frac{1}{2}\rho(v_{x,r=0}^2 - U_0^2) = \frac{1}{2}\Delta p$ , leading to  $v_{x,r=0}/U_0 = 0.745$  respectively 1.247. This differs from the calculated values shown in figure 5.10. Apart from this numerical disagreement there is no argument found in the momentum theory why the pressure jump should be symmetric.

As for flow decelerating discs  $|\mathbf{v}|$  is constant for all  $r/R$ , see the previous section, also the pressure and pressure jump are uniform in  $r$ .

**5.4.5. Momentum balance per annulus.** In the actuator disc momentum theory the change in the momentum of the flow passing the disc is uniquely coupled to the thrust at the disc. The pressure at the boundary of the stream tube does not play a role, as shown in section 5.2.2. The calculations confirm this: for  $C_T = -8/9$  the resultant force in  $x$ -direction equals 0.5% of the disc thrust. When the momentum theory is applied per annulus instead of the stream tube this may not be valid any more, as discussed in section 5.2.4. Still this is done in the Blade Element Momentum theory where the results of the actuator disc theory are assumed to be valid per annulus with each annulus being independent of the other annuli. It is known that this assumption is invalid, as shown theoretically by [Goorjian \(1972\)](#) and numerically by [Sørensen and Mikkelsen \(2001\)](#), but the consequences of this assumption are assumed to be modest.

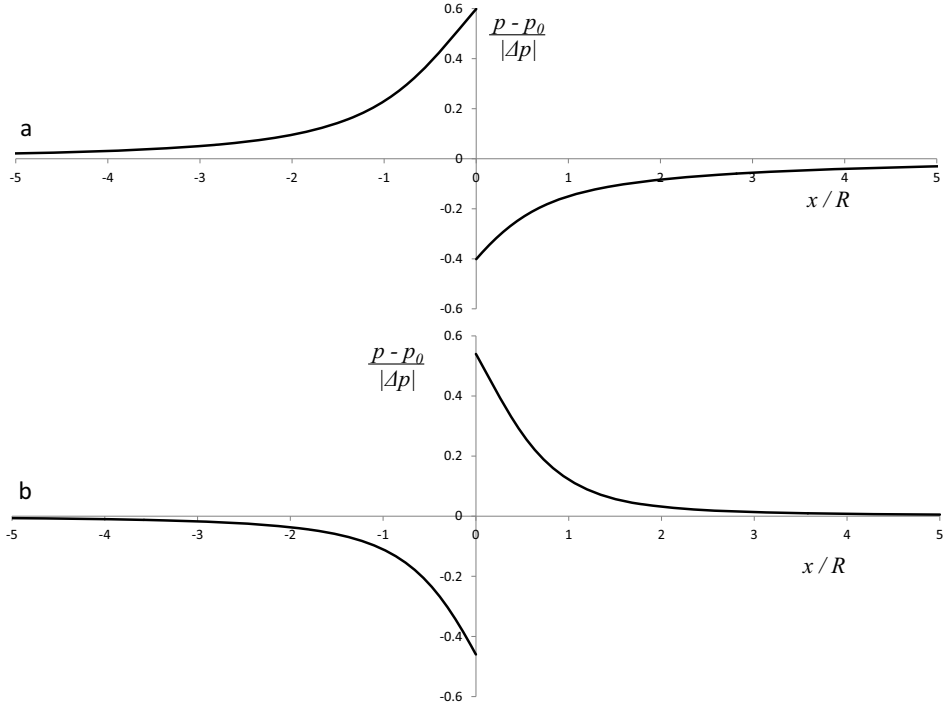


Figure 5.12: The pressure distribution at the disc and stream tube axis for a:  $C_T = -8/9$ , b:  $C_T = 16/9$ .

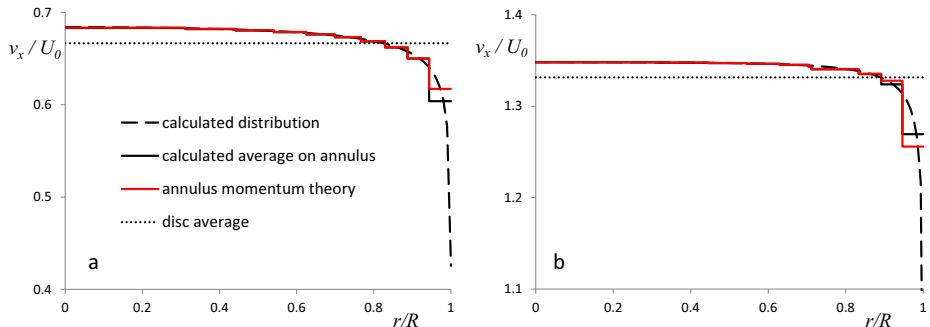


Figure 5.13: The axial velocity at the disc for a:  $C_T = -8/9$ , b:  $C_T = 16/9$ .

In section 5.2.4 the role of conservative forces in the momentum theory is treated, with the pressure at the boundary of an annulus, integrated to become an axial load  $T_{\text{annulus}}$ , as an example of a conservative load. Equation (5.17) shows that the ratio of  $T_{\text{annulus}}/T_d$  determines the deviation from the momentum theory without conservative forces, with  $T_d = \Delta p A_d$  and  $T_{\text{annulus}} = \int \mathbf{e}_x \cdot \mathbf{e}_n p dS_{\text{annulus}}$ .

This ratio has been calculated for the annuli defined by  $\Psi = \frac{n}{10}\Psi_d$  with  $n$  from 0 to 10 for both flow states  $C_T = -8/9$  and  $C_T = 16/9$ . The pressure integral is calculated with  $x/R = \pm 15R_1$  as up- and downstream limits.

Figure 5.13 shows the calculated distribution of  $v_x$ , the calculated average value in the respective annulus, the result of the annulus momentum theory (5.17) with calculated  $T_{annulus}/T_d$ , and the disc averaged value  $(U_0 + v_{x,1})/2$ . The results show a very good match of the calculated average per annulus and the momentum theory value except close to the disc edge where the steep change of  $v_{x,d}$  requires a finer resolution of annuli to capture the distribution accurately. The fact that  $v_x$  is not uniform appears to be a consequence of the contribution of the pressure to the momentum balance of the annuli. The annulus method gives the momentum balance in a number of discrete steps  $\Delta r$ . When it is applied in a differential form the contribution of the pressure is expressed in the pressure gradient normal to the streamline, so in  $\partial p/\partial n$ , which is the pressure gradient due to the expansion or contraction of the wake. One of the remarkable results is that in the centre of the disc  $v_x$  is higher than  $(U_0 + v_{x,1})/2$  so for a wind turbine disc the local power coefficient exceeds the Betz-Joukowsky limit.

Sørensen and Mikkelsen (2001) have done the same analysis by viscous CFD calculations, with approximately the same result. They attribute the large deviation from the disc-averaged value near the disc edge to the strong influence of viscous effects. Similar distributions of the axial velocity have been calculated by several others, e.g. Mikkelsen et al. (2009), Crawford (2006), Madsen (1996) and Madsen et al. (2007, 2010). Madsen et al. (2007) explain the high  $v_x$  for low  $r/R$  by the effect of wake rotation instead of pressure gradients due to wake contraction or expansion. Furthermore they analyse the decrease of the axial velocity near the tip and propose a correction method based on the radial velocity. Qualitatively the results of Madsen et al. (2007) correlate well with the present calculations but quantitatively they differ, e.g. the correction near the tip ( $r > 0.8R$ ) is approximately half of the correction presented in the next section.

The conclusion is that the non-uniformity of the induction is due to the pressure at the annuli acting as a conservative contribution to the momentum balance, not viscous effects or wake rotation. The non-uniform induction has consequences for the application of the momentum theory in BEM, see chapter 8.

## 5.5. An engineering model for the velocity at a wind turbine disc

With the distribution of  $v_{x,d}$  calculated for all  $C_T$  values shown in figure 5.4 a surface fit to  $v_{x,d}$  has been made, showing the non-uniformity as defined by the ratio  $T_{annulus}/T_d$  in (5.17). This is presented as an annulus-correction  $G(r, C_T)$ .

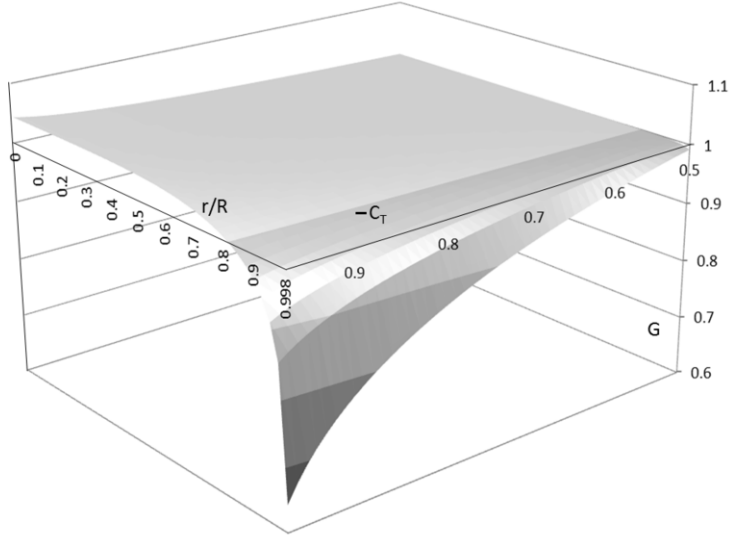


Figure 5.14: The function  $G(r, C_T)$  defined in (5.23) accounting for the non-uniformity of  $v_x$ .

Surface fitting gives the following engineering equation:

$$\left. \begin{aligned} G(r, C_T) &= 1 + a_1 \left( 1 - 1.00076 \left( 1 - \left( \frac{r}{R} \right)^{a_2} \right)^{0.0015} \right) \\ \text{with } a_1 &= 62.05(1 - C_T)^{0.42} - 47.56 \\ a_2 &= 5 - 2.5(C_T - 0.8) \end{aligned} \right\} C_T \leq -0.5 \quad (5.23)$$

$$G(r, C_T) = 1 \quad \left. \right\} -0.5 < C_T < 0 \quad (5.24)$$

The surface fit matches the calculated data with a difference less than  $< 1\%$  for  $C_T \geq -0.995$  and  $r/R < 0.95$ , and  $< 1.4\%$  for  $C_T \geq -0.995$  and  $r/R < 0.99$ . For  $C_T > -0.5$  the deviation of  $v_{x,d}$  from  $\bar{v}_{x,d}$  is negligible.

With the average velocity  $\bar{v}_{x,d}$  at the disc determined by momentum theory, the distribution is  $v_{x,d}(r, C_T)$  becomes:

$$\left. \begin{aligned} \frac{v_{x,d}}{U_0} &= G \frac{U_0 + v_{x,wake}}{2} \\ \frac{v_{x,wake}}{U_0} &= \sqrt{1 - C_T} \end{aligned} \right\} \quad (5.25)$$

The function  $G(r, C_T)$  will be used in chapter 8 to evaluate the effect on the non-uniformity of  $v_{x,d}$  in BEM.

## 5.6. Evaluation

This chapter has provided details of Froude actuator disc flows, so without swirl, by potential flow calculations complementing the results of the momentum theory. The pressure and flow fields as well as properties of the wake boundary vortex sheet have been analysed. This enables an answer to question Q7 listed in section 1.4 about a possible singularity at the leading edge of this vortex sheet. The calculations indeed show a singularity in the strength of the vortex sheet at its leading edge, which is at the same time the disc edge. This singularity is not strong enough to give a non-zero vortex strength at the disc leading edge. This holds for propeller as well as wind turbine disc flows.

A difference between wind turbine and propeller disc flows is found in the distribution of the velocity at the disc, giving an answer to Q8: the absolute velocity is constant for wind turbine disc flows, but not for propeller disc flows. An explanation of this is postponed to chapter 6. Q9 addresses the validity of applying the momentum balance per annulus instead of the entire stream tube. The change in axial momentum per annulus is accurately captured by a momentum balance in which the pressure at the surface of the annulus is included. The contribution of this pressure appears as a conservative load in the momentum balance, and does not appear in the energy balance. This explains the deviation of the results per annulus compared with the result per stream tube.

This page intentionally left blank

## Analysis of Joukowsky's actuator disc flows

### 6.1. Introduction

The basis for the momentum theory including the balance of angular momentum in the wake has been laid by [Joukowsky \(1918\)](#). The angular velocity or swirl is induced by a discrete vortex at the wake centre line, see figure [3.2](#). If the vortex kernel is infinitely small, the azimuthal velocity and pressure become infinite for the radius  $r \rightarrow 0$ . The question of how to model the discrete vortex and how this impacts the momentum balance has been studied by e.g. [de Vries \(1979\)](#); [Sharpe \(2004\)](#); [Xiros and Xiros \(2007\)](#); [Wood \(2007\)](#); [Sørensen and van Kuik \(2011\)](#). The reported performance predictions show a remarkable result for the disc extracting energy from the flow: in the limit to zero rotational speed, the efficiency of the disc increases to infinity, which is highly non-physical. Within the inviscid flow regime, the analysis in [Sørensen and van Kuik \(2011\)](#) is considered to be exact apart from the choice of the vortex core at the axis of the wake. This centreline vortex is assumed to be a Rankine vortex of which the core diameter is proportional to the wake radius. The analysis of [Sørensen and van Kuik \(2011\)](#) shows that adding a disturbance parameter to the momentum balance removes the non-physical result of infinite efficiency for zero rotational speed, no matter how small this disturbance is. This is an indication that the momentum balance is very sensitive to small deviations in the flow parameters.

The next section treats the momentum theory for Joukowsky discs, including an analysis of the vortex core model and its impact on the momentum theory, based on [van Kuik \(2017\)](#) and [van Kuik \(2018\)](#). The general mass, momentum and energy balances are derived and combined, with emphasis on the swirl-related pressure acting as a conservative load. Section [6.4](#) describes the numerical approach and its results, which are compared with the momentum theory results in section [6.6](#). This section also includes the comparison with the Betz-Goldstein solutions reported in literature.

### 6.2. Two dimensional momentum theory

**6.2.1. The equations for a Joukowsky disc.** The Joukowsky distribution is described in Explanation [3.1](#) and shown in figure [3.2](#). The flow is governed by the steady version of the Euler equation [\(2.1\)](#). The cylindrical reference system  $(x, r, \varphi)$  is applied, see also figure [6.1](#). The wake flow is characterized by a constant circulation induced by a free potential flow vortex  $\Gamma$  at the axis of the wake with

a vortex core having radius  $\delta(x)$ . The azimuthal velocity in the wake is:

$$\left. \begin{aligned} v_\varphi &= \frac{\Gamma}{2\pi r} && \text{for } r \geq \delta(x) \\ &= \frac{\Gamma}{2\pi\delta(x)} \mathcal{C}\left(\frac{r}{\delta(x)}\right) && \text{for } r < \delta(x) \end{aligned} \right\} \quad (6.1)$$

The functions  $\delta(x)$  and  $\mathcal{C}(r/\delta(x))$  remain unspecified apart from  $\mathcal{C} = 0$  for  $r = 0$  and  $\mathcal{C} = 1$  for  $r = \delta(x)$ . The core radius at the disc is indicated as  $\delta$  and the radius in the far wake as  $\delta_1$ . Figure 6.1 shows (half of) the cross section through the stream tube in the meridian plane, with the disc and fully developed wake indicated. The shaded area is the vortex core with an increasing radius towards the far wake due to the flow deceleration. The analysis starts with  $\delta$  being non-zero after which the limit of  $\delta \rightarrow 0$  is taken. The only assumption made is that:

$$\left. \begin{aligned} \delta_1 &\rightarrow 0 && \text{when } \delta \rightarrow 0 \\ \text{while} \\ \frac{\delta_1}{\delta} &> 1 && \text{for } \Delta H_d < 0 \\ \frac{\delta_1}{\delta} &< 1 && \text{for } \Delta H_d > 0 \end{aligned} \right\} \quad (6.2)$$

**6.2.2. The disc load.** In section 4.2.3 the disc load has been formulated for the disc area outside the vortex core. Here this will be extended to include the vortex core. Equations (4.5) applies in the vortex core so with (6.1):

$$\left. \begin{aligned} \frac{1}{\rho} \Delta H_d &= \frac{\Omega \Gamma}{2\pi} && \text{for } r \geq \delta(x) \\ &= \frac{\Omega \Gamma}{2\pi} \frac{r}{\delta(x)} \mathcal{C}\left(\frac{r}{\delta(x)}\right) && \text{for } r < \delta(x) \end{aligned} \right\} \quad (6.3)$$

Outside the core  $\Delta H_d = \text{constant}$  equal to (4.19) for  $r \geq \delta(x)$ . The thrust  $T$  is obtained by integration of (3.3) on the disc area. With (6.1) and (6.3) this gives for  $\delta \rightarrow 0$ :

$$\left. \begin{aligned} C_T &= C_{T,\Delta H} + C_{T,\Delta v_\varphi} \\ C_{T,\Delta H} &= \frac{\Omega \Gamma}{2\pi} = 2\lambda q \\ C_{T,\Delta v_\varphi} &= -q^2 \ln\left(\frac{R}{\delta}\right)^2 && \text{for } r \geq \delta(x) \\ &= -\left(\frac{\Gamma}{2\pi R U_0}\right)^2 \int_0^1 \mathcal{C}^2\left(\frac{r}{\delta}\right) d\left(\frac{r}{\delta}\right)^2 = 0 && \text{for } r < \delta(x) \end{aligned} \right\} \quad (6.4)$$

This is the same expression as (4.21) but now including the core area. The contribution of the vortex core to the thrust is zero as  $\mathcal{C}(0) = 0$  and  $\mathcal{C}(1) = 1$ . The thrust component  $C_{T,\Delta v_\varphi}$  is absent in the one-dimensional momentum theory.

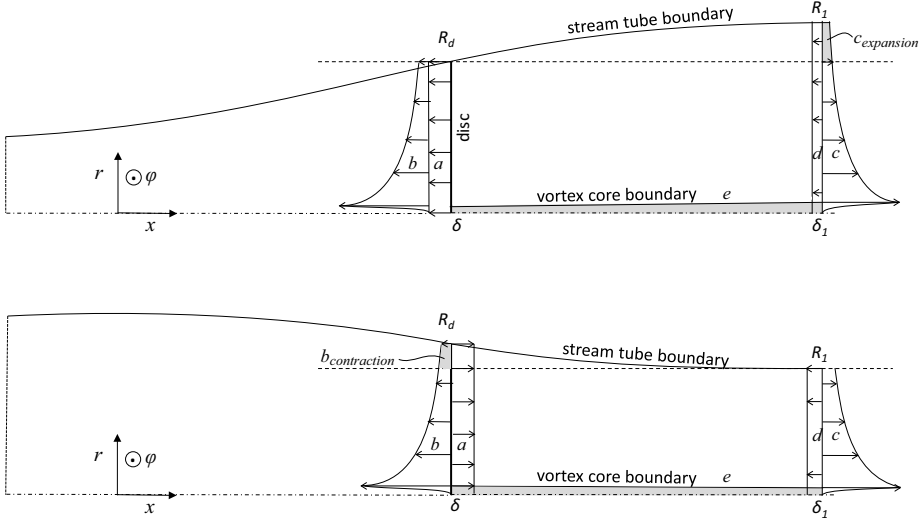


Figure 6.1: Pressure distributions acting in the momentum balance sketched for an energy extracting disc flow (up) and energy adding disc (down). The arrows give the direction of the pressure fields acting on the flow. The meaning of  $a$ ,  $b$ ,  $c$ ,  $d$  and  $e$  is given in section 6.2.5.

**6.2.3. The far wake outside the vortex core.** The Bernoulli equation (6.3) for  $r \geq \delta_1$  is written as:

$$\frac{1}{\rho} (p_0 - p_1) = \frac{1}{2} (v_{x,1}^2 - U_0^2 + v_{\varphi,1}^2) - \frac{\Omega \Gamma}{2\pi}. \quad (6.5)$$

Differentiation with respect to  $r$  yields  $\partial p_1 / \partial r_1 = \rho(v_{\varphi,1}^2 / r_1 - v_{x,1} \partial v_{x,1} / \partial r)$ . Comparison with the expression for radial pressure equilibrium obtained from the radial component of the (steady) equation of motion (A.10) with  $v_r = 0$ :

$$\frac{\partial p_1}{\partial r_1} = \rho \frac{v_{\varphi,1}^2}{r_1} \quad (6.6)$$

shows that  $v_{x,1}$  is constant. By this (6.5) can be written as:

$$p_1 - p_0 = -\frac{1}{2} \rho v_{\varphi,1}^2 + p^*. \quad (6.7)$$

At the wake boundary the pressure has to be undisturbed ( $p_0$ ), so  $p^* = \frac{1}{2} \rho v_{\varphi,R_1}^2$  and, with (6.1):

$$p_1 - p_0 = -\frac{1}{2} \rho v_{\varphi,1}^2 + \frac{1}{2} \rho \left( \frac{\Gamma}{2\pi R_1} \right)^2. \quad (6.8)$$

This shows that the pressure variation in the far wake is caused only by the swirl, similar to the pressure jump across the disc. By substitution of (6.8) in (6.5) and with (6.3) the second term on the right-hand side appears as a loss in  $H$  due to

swirl:

$$\Delta H = \frac{1}{2}\rho(v_{x_1}^2 - U_0^2) - \frac{1}{2}\rho\left(\frac{\Gamma}{2\pi R_1}\right)^2. \quad (6.9)$$

This is consistent with the optimization of rotors according to Glauerts theory which involves minimization of the swirl, see e.g. [Sørensen \(2015\)](#).

**6.2.4. The vortex core.** The momentum theory results are very sensitive to the choice of  $\delta$  and  $\delta_1$ . This is caused by the logarithmic singularity resulting from the integration of the pressure due to the azimuthal velocity: at the disc  $-\rho\pi \int_\delta^R v_\varphi^2 r dr = -\rho \frac{\Gamma^2}{4\pi} \ln \frac{R}{\delta}$  and similarly in the far wake  $-\rho \frac{\Gamma^2}{4\pi} \ln \frac{R_1}{\delta_1}$ . Previous solutions have dealt with the singularity in different ways. [Sørensen and van Kuik \(2011\)](#) have adopted  $\delta/\delta_1 = R/R_1$ , assuming that the vortex core grows with the stream tube radius. This removes the singularity as  $-\rho \frac{\Gamma^2}{4\pi} \ln \frac{R}{\delta} + \rho \frac{\Gamma^2}{4\pi} \ln \frac{R_1}{\delta_1} = 0$ . For the energy extracting disc this leads to  $C_p \rightarrow -\infty$  for  $\lambda \rightarrow 0$ . [van Kuik \(2016\)](#) assumes  $\delta = \delta_1$  leading to the power coefficient  $C_p \rightarrow 0$  for  $\lambda \rightarrow 0$ . However, as discussed in [van Kuik \(2016\)](#), both core models do not comply with the inviscid flow equations, so the impact of the vortex core model to the momentum balance merits an additional investigation.

Both analyses used the vortex core boundary as lower limit in the integration of momentum and energy on the control volume used in momentum theory. This implies that the vortex core is excluded, motivated by its vanishing dimension in the limit  $\delta, \delta_1 \rightarrow 0$ . Here the vortex core will be included in the momentum balance, while still the same limit is taken.

With  $\delta(x)$  denoting the local core radius the Bernoulli equation (6.3) in the vortex core region becomes:

$$\frac{1}{\rho}(p_0 - p) = \frac{1}{2} \left( v_s^2 - U_0^2 + \left( \frac{\Gamma}{2\pi\delta(x)} \mathcal{C} \left( \frac{r}{\delta(x)} \right) \right)^2 \right) - \frac{\Omega\Gamma}{2\pi} \frac{r}{\delta(x)} \mathcal{C} \left( \frac{r}{\delta(x)} \right) \quad \text{with } \frac{r}{\delta(x)} \leq 1, \quad (6.10)$$

where  $v_s$  is the velocity in the meridian plane. As  $v_s$ ,  $U_0$  and the last term on the right-hand side remain finite in the limit  $\delta(x) \rightarrow 0$  the pressure becomes in this limit:

$$\lim_{\delta(x) \rightarrow 0} \frac{1}{\rho}(p_0 - p) = \frac{1}{2} \left( \frac{\Gamma}{2\pi\delta(x)} \mathcal{C} \left( \frac{r}{\delta(x)} \right) \right)^2 \quad \text{with } \frac{r}{\delta(x)} \leq 1. \quad (6.11)$$

As the momentum flux through the control volume boundary has become 0 for  $\delta(x) \rightarrow 0$ , the momentum balance reduces to a balance of pressures acting on the control volume boundary, integrated as a load in  $x$  direction:

$$\int_0^\delta (p - p_0) 2\pi r dr - \int_0^{\delta_1} (p_1 - p_0) 2\pi r dr + \int_\delta^{\delta_1} (p(x, \delta(x)) - p_0) 2\pi \delta(x) d\delta(x) = 0. \quad (6.12)$$

where the path of integration of the third integral is the core boundary  $\delta(x)$  with  $0 \leq x \leq x_1$ . The third integral is evaluated with (6.11) so:

$$\lim_{\delta(x) \rightarrow 0} \left[ \int_{\delta}^{\delta_1} (p(x, \delta(x)) - p_0) 2\pi\delta(x) d\delta(x) \right] = -\rho\pi \int_{\delta}^{\delta_1} v_{\varphi}^2 2\pi\delta(x) d\delta(x) = -\rho \frac{\Gamma^2}{4\pi} \ln \frac{\delta_1}{\delta}. \quad (6.13)$$

The combination of (6.12) and (6.13) gives:

$$\lim_{\delta(x) \rightarrow 0} \left[ \int_0^{\delta} (p - p_0) 2\pi r dr - \int_0^{\delta_1} (p_1 - p_0) 2\pi r dr \right] = \rho \frac{\Gamma^2}{4\pi} \ln \frac{\delta_1}{\delta}, \quad (6.14)$$

irrespective of the choice of core model  $\delta(x)$ ,  $\mathcal{C}(r/\delta(x))$ .

This result will be used in section 6.2.5 where the momentum balance for the entire stream tube is studied. Unless specifically indicated, all equations in the forthcoming sections are derived for the flow region outside of the vortex core.

**6.2.5. The momentum, mass and energy balance.** The momentum balance (5.1) drawn on the stream tube as control volume, see figure 6.1, is written as:

$$T - \int_{A_1} (p_1 - p_0) 2\pi r dr = \rho \int_{A_1} v_{x,1} (v_{x,1} - U_0) dA_1. \quad (6.15)$$

The boundaries of the momentum balance volume are the stream tube boundary and the cross sections  $A_0$  and  $A_1$  far up- and downstream. As discussed in section 5.2 the pressure at the stream tube boundary does not contribute to the momentum balance so is not included in (6.15).

Figure 6.1 shows the pressure distributions appearing on the left-hand side of (6.15) including the thrust:

- a constant pressure jump across the disc giving the jump in Bernoulli parameter  $H$  according to the first term on the right-hand side of (3.3).
- b pressure distribution due to jump in  $v_{\varphi}$  for  $r \geq \delta$  according to the second term on the right-hand side of (3.3). This term conserves  $H$ .
- c apart from correction by (d) the pressure distribution in the far wake due to the  $v_{\varphi}$  distribution is identical to (b) for  $r \geq \delta_1$  according to the first term at the right hand side of (6.8), conserving  $H$ .
- d a correction to (c) to achieve  $p_1 - p_0 = 0$  according to the second term on the right-hand side of (6.8).
- e the contribution by the vortex core cross sections, (6.14).

When all contributions are expressed in  $\Gamma$  by (6.1) and (6.3), integrated, subjected to  $\lim \delta \rightarrow 0$ , substituted in (6.15) and divided by the disc surface  $\pi R^2$  the result is:

$$\frac{\Omega\Gamma}{2\pi} - \frac{1}{2} \left( \frac{\Gamma}{2\pi R} \right)^2 - \left( \frac{\Gamma}{2\pi R} \right)^2 \left[ \ln \frac{R}{\delta} - \ln \frac{R_1}{\delta_1} - \ln \frac{\delta_1}{\delta} \right] = v_{x,1} (v_{x,1} - U_0) \left( \frac{R_1}{R} \right)^2 \quad (6.16)$$

*a*                    *d*

*b*                    *c*                    *e*

where the terms on the left-hand side have been named in accordance with figure 6.1. The term between square brackets simplifies to  $\ln(R/R_1)$ . In other words:

only the wake expansion area ( $c_{expansion}$ ) or wake contraction area ( $b_{contraction}$ ) contribute to this term. These contributions are shown as grey areas in figure 6.1. The mass balance is:

$$\frac{\bar{v}_{x,d}}{v_{x,1}} = \left( \frac{R_1}{R} \right)^2 \quad (6.17)$$

with the bar above  $v_{x,d}$  indicating that it is the average value. The energy balance follows from (6.9):

$$\frac{\Omega\Gamma}{2\pi} - \frac{1}{2} \left( \frac{\Gamma}{2\pi R_1} \right)^2 = \frac{1}{2} (v_{x,1}^2 - U_0^2). \quad (6.18)$$

Mixing (6.16) and (6.17) simplifies the momentum balance, yielding:

$$\frac{\Omega\Gamma}{2\pi} - \frac{1}{2} \left( \frac{\Gamma}{2\pi R} \right)^2 - \left( \frac{\Gamma}{2\pi R} \right)^2 \ln \frac{R}{R_1} = \bar{v}_{x,d} (v_{x,1} - U_0). \quad (6.19)$$

As in section 4.2.3 the non-dimensional vortex  $q = \frac{\Gamma}{2\pi R U_0}$  is introduced. Herewith (6.3) becomes:

$$\frac{1}{\rho} \frac{\Delta H_d}{U_0^2} = \lambda q, \quad (6.20)$$

and the momentum balance:

$$-2\lambda q + q^2 \left( 1 + \ln \left( \frac{R}{R_1} \right)^2 \right) = 2 \frac{\bar{v}_{x,d}}{U_0} \left( 1 - \frac{v_{x,1}}{U_0} \right) \quad (6.21)$$

and the energy balance:

$$-2\lambda q + q^2 \left( \frac{R}{R_1} \right)^2 = \left( 1 - \left( \frac{v_{x,1}}{U_0} \right)^2 \right). \quad (6.22)$$

By mixing (6.21) and (6.22) the velocity at the disc can be written as:

$$\frac{\bar{v}_{x,d}}{U_0} = \frac{1}{2} \left( \frac{v_{x,1}}{U_0} + 1 \right) \frac{2\lambda q - q^2 \left( 1 + \ln \left( \frac{R}{R_1} \right)^2 \right)}{2\lambda q - q^2 \left( \frac{R}{R_1} \right)^2}. \quad (6.23)$$

This equation is equivalent to (5.13), indicating that the ratio contains conservative and non-conservative contributions. This will be discussed in section 6.5.

An analytical solution of (6.21) and (6.22) is not found. An implicit expression of  $v_{x,1}/U_0$  in the independent variables  $\lambda$ ,  $q$  is obtained by writing (6.22) as an expression for  $v_{x,1}$  with the help of (6.17) and substituting this in (6.21):

$$\frac{\left( 1 - \frac{v_{x,1}}{U_0} \right) \frac{v_{x,1}}{U_0} q^2}{1 - 2\lambda q - \left( \frac{v_{x,1}}{U_0} \right)^2} = \left( -q\lambda - \frac{1}{2} q^2 \left( 1 - \ln \left( \frac{q^2}{1 - 2\lambda q - \left( \frac{v_{x,1}}{U_0} \right)^2} \right) \right) \right). \quad (6.24)$$

This can be solved numerically for  $v_{x,1}/U_0$ . The wake expansion or contraction follows from (6.22) and the velocity at the disc from (6.21). The power coefficient follows by integration of (4.1) on the disc area:  $P = \int_{A_d} \mathbf{F} \cdot \mathbf{v} = \bar{v}_{x,d} \Delta H A_d$ . In dimensionless form this becomes:

$$C_p = 2\lambda q \frac{\bar{v}_{x,d}}{U_0}. \quad (6.25)$$

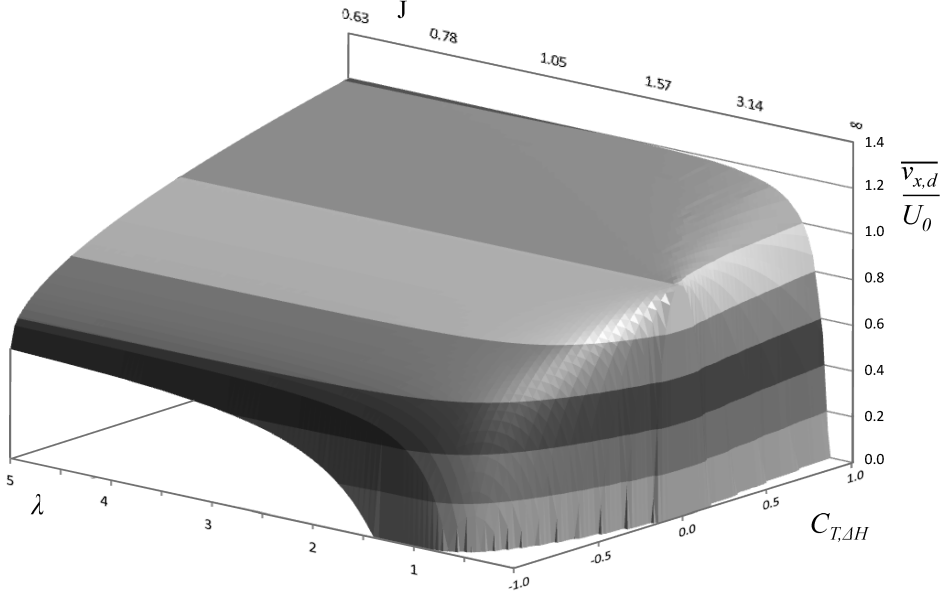


Figure 6.2: The axial velocity  $\bar{v}_{x,d}$  at the disc for wind turbine discs ( $C_{T,\Delta H} < 0$ ) and propeller ( $C_{T,\Delta H} > 0$ ) for  $0 \leq \lambda \leq 5$ .

Figures 6.2 and 6.3 show the solutions of (6.24) and (6.25) for  $0 \leq \lambda \leq 5$  and  $-1 < C_{T,\Delta H} \leq +1$ . The front left sides show  $\bar{v}_{x,d}/U_0$  respectively  $C_p$  for wind turbine discs, right behind for propeller discs. Several particularities can be observed, to be addressed in the next sections:

- for very low  $\lambda$  the velocity at propeller discs is  $< 1$ , so the wake expands as for wakes of energy extracting discs,
- a minimum  $\lambda > 0$  exists at which the velocity at the disc is 0,
- the maximum efficiency  $|C_p|$  of energy extracting discs decreases to 0 for decreasing  $\lambda$ .

### 6.3. Limit values of the Joukowsky momentum theory

**6.3.1. Results for  $\lambda \rightarrow \infty$ ,  $\lambda \rightarrow 0$ .** For large values of  $\lambda$  the wake angular momentum should go to 0, and the momentum theory should become the one-dimensional theory. For an energy extracting disc the well-known Betz-Joukowsky maximum value for  $C_p$  should be recovered. According to (6.20)  $q$  is inversely proportional to  $\lambda$  for constant  $\Delta H$ . In the balances (6.21) and (6.22) the  $q^2$  terms vanish for  $\lambda \rightarrow \infty$  with which the momentum theory without wake swirl is indeed recovered.

For the limit  $\lambda \rightarrow 0$  the energy balance (6.22) shows that the highest value for  $q^2(R/R_1)^2$  is obtained for  $v_{x,1}/U_0 = 0$ :

$$-2\lambda q + q^2 \left( \frac{R}{R_1} \right)^2 = 1. \quad (6.26)$$

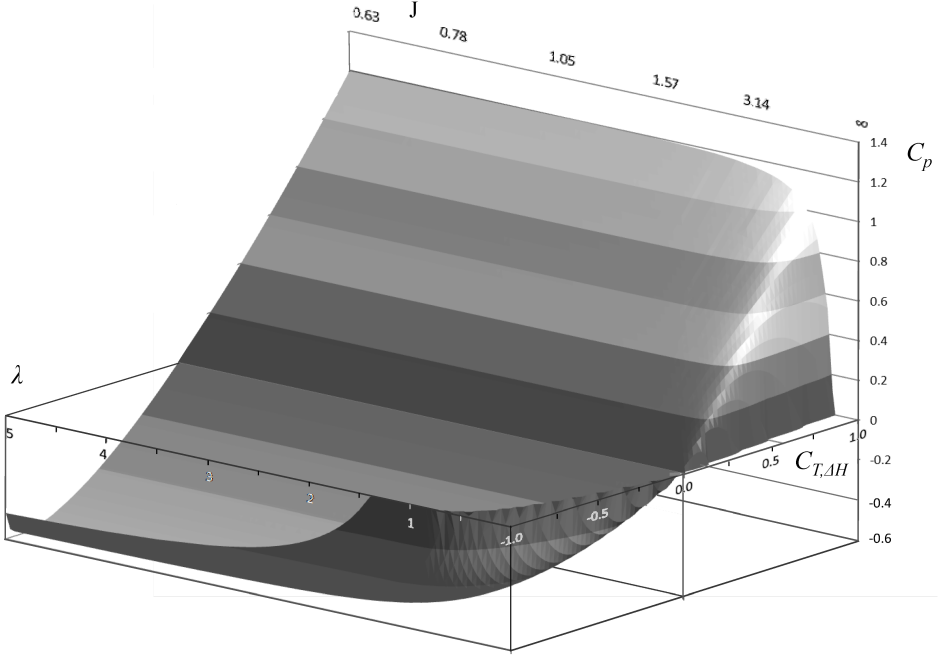


Figure 6.3: The power coefficient  $C_p$  for wind turbine discs ( $C_{T,\Delta H} < 0$ ) and propeller ( $C_{T,\Delta H} > 0$ ) for  $0 \leq \lambda \leq 5$ .

With  $v_{x,1}/U_0 = 0$  the right-hand side of the momentum balance is 0 as is clear from (6.16), by which it becomes:

$$-2\lambda q + q^2 \left( 1 - \ln \left( \frac{R_1}{R} \right)^2 \right) = 0. \quad (6.27)$$

Elimination of  $q^2$  from (6.26) and (6.27) gives the wake expansion or contraction for the highest  $q$ , lowest  $\lambda$ :

$$\left( \frac{R_1}{R} \right)^2 \left( 1 - \ln \left( \frac{R_1}{R} \right)^2 \right) = \frac{2\lambda q}{2\lambda q + 1}. \quad (6.28)$$

As an example,  $2\lambda q = \Delta H / (\frac{1}{2}\rho U_0^2) = -8/9$  results in  $R_1/R = 2.77$ ,  $q = -0.924$  from (6.26) and  $\lambda = 0.48$ . Both  $\bar{v}_{x,d}$  and  $v_{x,1}$  are 0, but the ratio of  $\bar{v}_{x,d}/v_{x,1} \rightarrow 7.69$ . This flow state is characterized by a full blockage by the disc, creating a wake with azimuthal flow only, so there is no change in axial momentum. A lower value of  $\lambda$  is not possible for this value of  $C_{T,\Delta H} = 2\lambda q$ . For  $\lambda q = 0$  with  $\lambda = 0$  (6.28) gives  $\ln(R_1/R)^2 = 1$  and (6.26) gives  $R_1/R = -q = \sqrt{e} = 1.648$  although  $\bar{v}_{x,d} = v_{x,1} = 0$ . In the wake only the azimuthal velocity is non-zero, reaching  $qR/R_1 = -1$  at the far wake boundary  $r = R_1$ . The wake expansion is close to the experimental value  $\approx 1.6$  of the wake expansion behind a solid disc reported in Craze (1977).

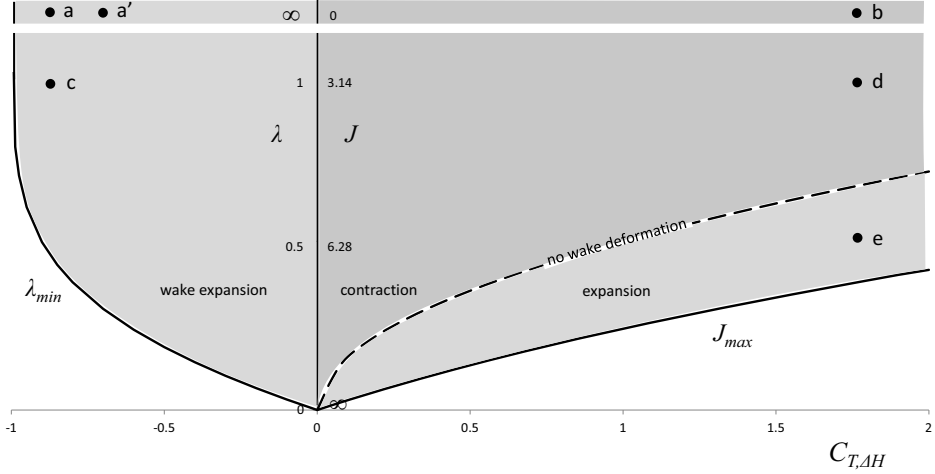


Figure 6.4: The operational regimes of an actuator disc: for negative  $C_{T,\Delta H}$  energy is extracted from the flow, for positive  $C_{T,\Delta H}$  energy is added. The flow states indicated by  $\mathbf{a}'$  ( $C_{T,\Delta H} = -0.7138, \lambda = \infty$ ) and  $\mathbf{e}$  ( $C_{T,\Delta H} = 16/9, \lambda = 0.5$  or  $J = 2\pi$ ) have identical deceleration in the far wake, so equal far wake induction. The flow states indicated by  $\mathbf{c}$  ( $C_T = -8/9, \lambda = 1$ ) and  $\mathbf{d}$  ( $C_{T,\Delta H} = 16/9, \lambda = 1$  or  $J = \pi$ ) have equal but opposite induction in the far wake. The same holds for  $\mathbf{a}$  and  $\mathbf{b}$  with the same  $C_{T,\Delta H}$  as flow states  $\mathbf{c}$  and  $\mathbf{d}$  but with  $\lambda = \infty, J = 0$ . Flow states  $\mathbf{a}$  and  $\mathbf{b}$  are the ones shown in chapter 5.

A complete blockage of the flow by energy adding disc is also possible as shown by figure 6.2 for  $C_{T,\Delta H} > 0$ . For low  $\lambda$  the axial velocity  $\bar{v}_{x,d} < U_0$  so the flow decelerates, with  $\bar{v}_{x,d} = 0$  for the lowest possible  $\lambda$ . Figure 6.4 shows the lowest attainable  $\lambda$  as a function of  $C_{T,\Delta H}$ , being the solution of (6.26) and (6.28). This behaviour for low  $\lambda$  is explained in the next section.

**6.3.2. Propeller discs with a wake of constant radius and with wake expansion.** For discs adding energy to the flow, the sign of pressure distribution (b) in figure 6.1 is opposite to the sign of (a), so flow states with a zero pressure jump at  $r = R$  are possible. With (4.6) this gives the condition  $\Omega R = \frac{1}{2}v_\varphi$  or  $\lambda = q/2$ . The result is a flow with everywhere  $v_x = U_0$ ,  $v_r = 0$ , and in the wake  $v_\varphi = \Gamma/(2\pi r)$ . The wake boundary consists of a cylindrical vortex sheet with constant radius  $R$ , having only axial vorticity carrying  $\Delta H = \frac{1}{2}(\Omega R)^2$ . At the disc edge distributions (a) and (b) cancel each other, in the far wake ( $c_{\text{expansion}}$ ) or ( $b_{\text{contraction}}$ ) are absent and finally (d) equals -(a). In other words: the swirl induces a lower pressure which is compensated by a higher pressure due to an increase in  $H$  by distribution (a), as shown by (3.3): for  $\Delta p_d = 0$  at  $r = R$   $\Delta H_d = \rho\Omega R v_{\varphi,R}$  or, by (4.5),  $\lambda = \frac{1}{2}v_{\varphi,R}/U_0 = \frac{1}{2}q$ . With this, the line ‘no wake deformation’ in figure 6.4 is given by  $\lambda = \frac{1}{2}\sqrt{C_{T,\Delta H}}$ .

For  $\lambda > q/2$  the wake contracts as expected for a disc in propeller mode. However, for  $\lambda < q/2$  the wake expands as for a disc in wind turbine mode.

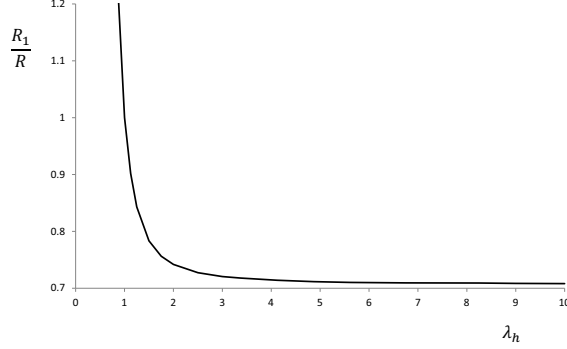


Figure 6.5: The wake expansion or contraction for a static (hovering) disc as function of  $\lambda_h$ .

Figure 6.4 shows where this transition takes place. Flow states **a'** and **e** have the same far wake deceleration. The corresponding flow patterns are shown in section 6.4, figure 6.10.

**6.3.3. The static disc or disc in hover.** This is a special flow state as  $U_0 = 0$ , so the non-dimensional equations (6.20) to (6.25) loose they meaning and an alternative derivation is required. Substitution of  $U_0 = 0$  in the balances (6.18) and (6.19) and merging (6.17) with (6.19) gives two expressions for  $v_{x,1}^2$ . Equating these yields :

$$\frac{\Omega\Gamma}{2\pi} \left( 2 \left( \frac{R_1}{R} \right)^2 - 1 \right) = \frac{1}{2} \left( \frac{\Gamma}{2\pi R} \right)^2 \left( 1 + \ln \left( \frac{R_1}{R} \right)^2 \right). \quad (6.29)$$

As in (5.10) and figure 5.4 the velocity at the static disc according to the one-dimensional momentum theory is used:  $v_{x,\text{reference}} = \sqrt{T/(2\rho A_d)} = \sqrt{\Delta p/(2\rho)}$ . Here we use  $\Delta H = \Omega\Gamma/(2\pi)$  instead of  $\Delta p$  so with (6.3)  $v_{x,\text{ref}} = \sqrt{\Omega\Gamma/(4\pi)}$ . With the introduction of the non-dimensional vortex  $q_h = \Gamma/(2\pi R v_{x,\text{ref}})$  and tip speed ratio  $\lambda_h = \Omega R/v_{x,\text{ref}}$ , and with division of (6.29) by the square of the reference velocity, we arrive at:

$$\left. \begin{aligned} 2 \left( 2 \left( \frac{R_1}{R} \right)^2 - 1 \right) &= \frac{1}{2} q_h^2 \left( 1 + \ln \left( \frac{R_1}{R} \right)^2 \right) \\ \text{with } \lambda_h q_h &= 2. \end{aligned} \right\} \quad (6.30)$$

The wake contraction  $R_1/R$  depends only on  $q_h$  or  $\lambda_h$ . Figure 6.5 shows  $R_1/R$  as a function of  $\lambda_h$ . For high  $\lambda_h$  the wake contraction becomes  $\frac{1}{2}\sqrt{2}$  being the solution in the one-dimensional theory. For low values of  $\lambda_h$   $R_1/R > 1$  so the wake expands corresponding to the results in section 6.3.2. The straight wake,  $R_1 = R$ , is obtained for  $\lambda_h = 1$ .

**6.3.4. The maximum efficiency of a wind turbine disc.** Figure 6.6 shows the maximal attainable  $|C_p|$  for discs in the wind turbine mode, and the  $|C_p| - \lambda$  curves for some values of  $C_{T,\Delta H}$ . For  $\lambda \rightarrow 0$  the efficiency  $|C_p| \rightarrow 0$ .

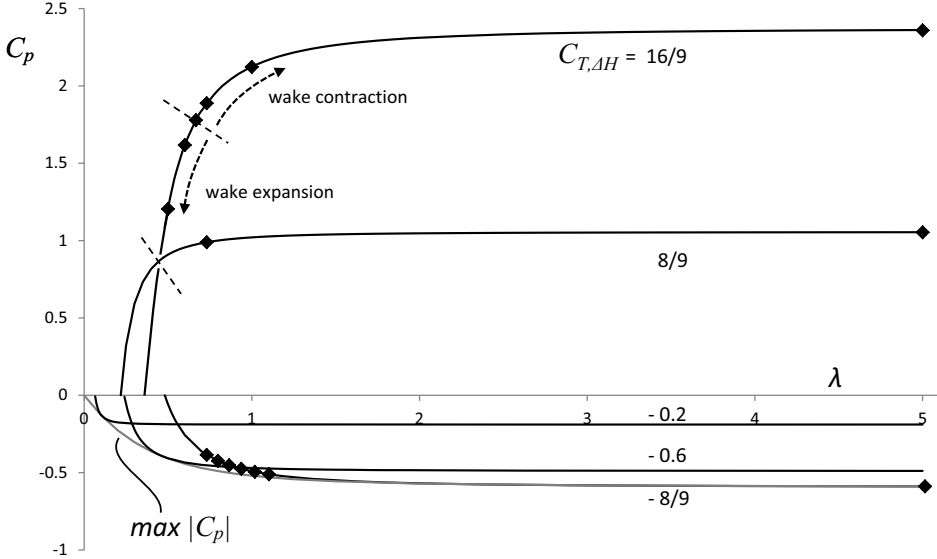


Figure 6.6: The Joukowsky momentum theory results (black lines), calculated values ( $\blacklozenge$ , see section 6.4) and the maximum wind turbine  $|C_p|$  (grey line).

The difference with  $|C_p| \rightarrow \infty$  as obtained in Sørensen and van Kuik (2011) is caused by the different treatment of the vortex core: instead of assuming that  $\delta(x)$  increases linear with the wake expansion, now  $\delta(x)$  is not specified apart from condition (6.2), and the contribution of the vortex core to the momentum balance is included. In section 6.6 the  $|C_{p,max}| - \lambda$  curve of Joukowsky discs will be compared with the same curve of Betz-Goldstein discs.

**6.3.5. The efficiency of propeller discs.** For discs representing propellers the efficiency  $\mu$  is defined as the ratio of the effective work  $TV$  where  $V$  is the flying speed, and the work done by the propeller  $Q\Omega$ . In our notation  $V$  is replaced by  $U_0$ , and, with (4.1) integrated over the disc,  $P = T\bar{v}_{x,d}$ , so for the flows considered here:

$$\eta = \frac{U_0}{\bar{v}_{x,d}}. \quad (6.31)$$

This implies that the efficiency is the inverse of figure 6.2 for  $C_T > 0$ . Referring to figure 6.4,  $\eta < 1$  for operation at  $\lambda > \lambda_{v_{x,d}=U_0}$ ,  $\eta > 1$  for  $\lambda_{min} < \lambda < \lambda_{v_{x,d}=U_0}$ , with the limit  $\eta \rightarrow \infty$  for  $\lambda \rightarrow \lambda_{min}$ . It is clear that this infinite efficiency is a consequence of the definition, not of the physics involved.

## 6.4. Numerical assessment of flow details

**6.4.1. The numerical model.** The numerical method described in section 5.3 has been adapted to include wakes with swirl. Axial and radial velocities are calculated by summation of the induction by each of the vortex rings which constitute the wake boundary. The azimuthal velocities are calculated from (6.1). The

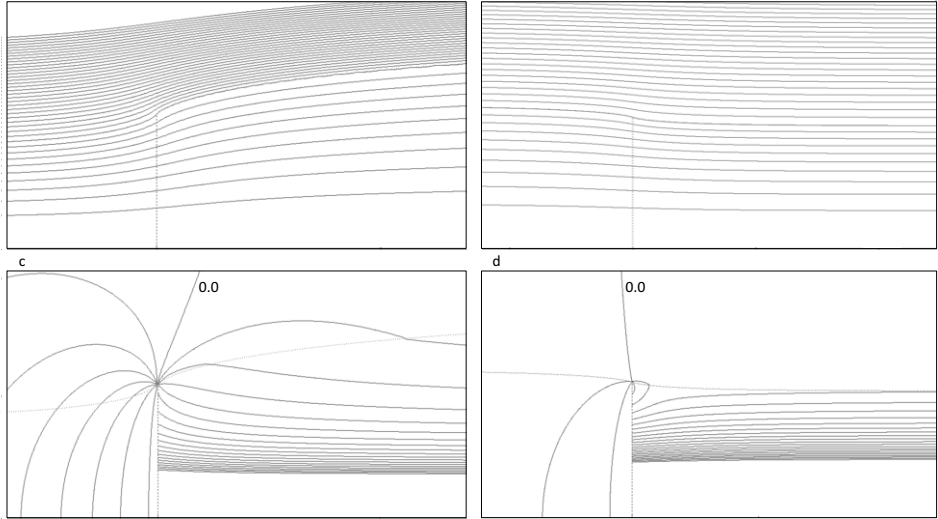


Figure 6.7: Flow states **c** and **d** with  $\lambda = 1$  corresponding to the same indications in figure 6.4: **c** shows streamlines with  $\Delta\psi = 0.1\Delta\psi_{wake}$  and isobars with  $\Delta p = 0.1\Delta H$  for  $C_{T,\Delta H} = -8/9$ , **d** for  $C_{T,\Delta H} = +16/9$ . Isobars close to the wake axis are not plotted.

shape and strength of the vortex rings are adapted in the convergence scheme to satisfy the two boundary conditions: zero pressure jump across the wake boundary, and zero cross flow. The numerical implementation is given by (D.10) and (D.11) or (D.12), with  $\Delta H$  given by (3.3), so at the wake boundary:

$$\Delta H = \Delta \left( \frac{1}{2} \rho v^2 \right) = \Delta p_d + \frac{1}{2} \rho v_\varphi^2 \quad (6.32)$$

The strength of the vortex at the axis follows from (6.20) expressed in  $H$  and  $\lambda$ :  $q = \Delta H / (\rho U_0^2 \lambda)$ . As  $q$  and  $\lambda$  depend on the disc radius, unknown at the start of the convergence towards a solution, the computation uses  $q_1$  and  $\Delta H$  as independent parameters. When  $R_d$  is known,  $q = q_1 R_1 / R$  and  $\lambda = q^{-1} \Delta H / (\rho U_0^2)$  by (3.3). Apart from these changes the code and the numerical parameters are unmodified. The results satisfy the same accuracy requirements as described in section 5.3.1. Figure 6.6 shows the calculated  $C_p(\lambda)$  for fixed values of  $2\lambda q = \Delta H / \frac{1}{2} \rho U_0^2$  and the momentum theory values. The data match very well, for discs adding energy as well as extracting energy. Also indicated are the  $\lambda$ -values below which the wake expands for positive  $C_p$  or  $C_{T,\Delta H}$  as indicated in figure 6.4. For  $\lambda = 5$  the difference in  $C_p$  compared with the values for  $\lambda \rightarrow \infty$ , so with the one-dimensional momentum theory, is less than 0.7%. Consequently, swirl may be ignored for  $\lambda > 5$ .

**6.4.2. Comparison of wind turbine and propeller discs at  $\lambda = 1$ .** Figure 6.7 shows the streamlines and isobars of the disc flow with  $\lambda = 1$  for  $C_{T,\Delta H} = -8/9$  and  $+16/9$  (flow states **c** and **d** in figure 6.4). The isobars in the

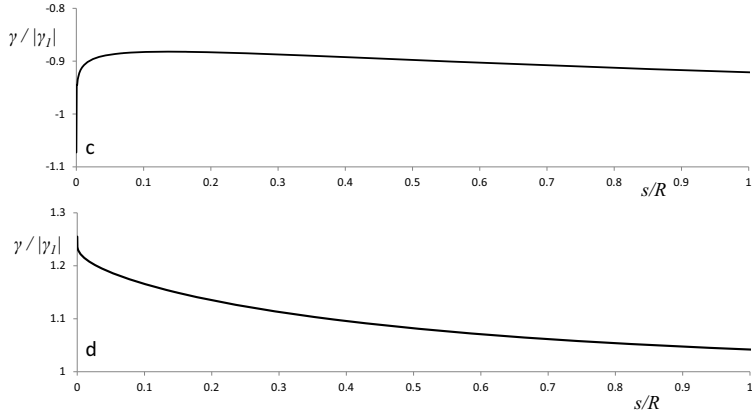


Figure 6.8: Strength of the vortex sheet as a function of the distance  $s/R$  measured along the sheet, for the flow states mentioned in figure 6.7.

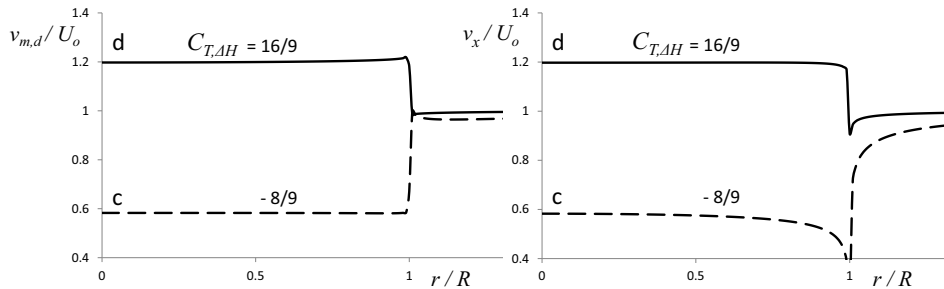


Figure 6.9: The velocity distribution at the disc for the flow states shown in figure 6.7. Left is shown the velocity in the meridian plane,  $|v_{m,d}| = \sqrt{v_x^2 + v_r^2}$ , right the axial velocity.

wake show the pressure gradient due to the swirl. The distribution of the vortex sheet strength  $\gamma$  is shown in figure 6.8, and the absolute and axial velocity at the upstream side of the disc in figure 6.9. As for the Froude disc flows a and b shown in chapter 5, the absolute velocity in the meridian plane is constant for wind turbine discs, but not for propeller discs. Apparently the presence of swirl in the wake does not affect this property. This will be discussed in section 6.5.

**6.4.3. Comparison of a wind turbine and propeller disc with similar wake expansion.** Figure 6.10 shows the flow patterns of flow states a' and e in figure 6.4 having the same wake deceleration, so the same negative value for  $\gamma_1$ . Flow state a' is generated by a wind turbine disc, e by a propeller disc. As for the flow states a and c shown in figure 6.4, the pressure distribution at the upwind side of wind turbine disc a' is constant. Similarly the pressure is non-uniform in case of propeller disc e, as for flow states b and d. By the Bernoulli equation this

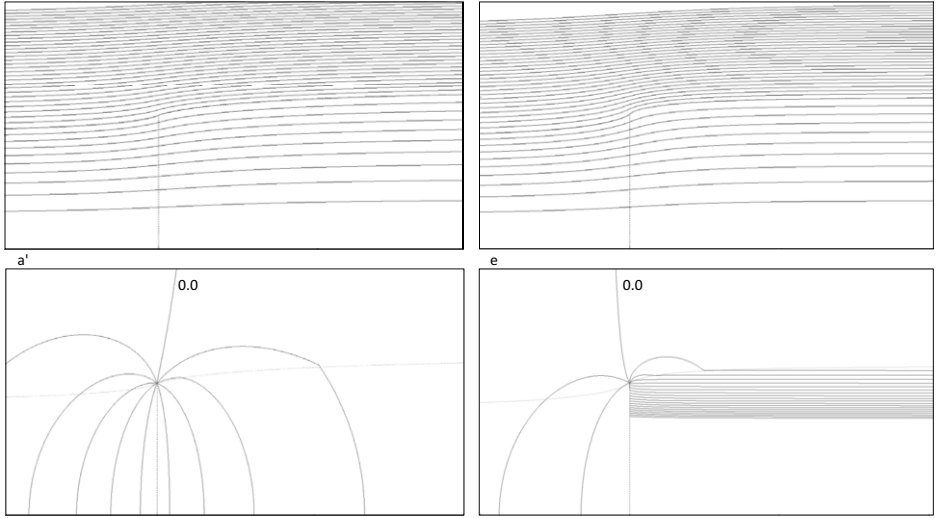


Figure 6.10: Flow states  $a'$  and  $e$  with the same axial velocity in the far wake, corresponding with the indications in figure 6.4.  $a'$  shows  $C_{T,\Delta H} = -0.7138, \lambda = \infty, R_1/R = 1.197$ ,  $e$ :  $C_{T,\Delta H} = 16/9 = 1.7777, \lambda = 0.5, R_1/R = 1.126$ . The explanation is as in figure 6.7.

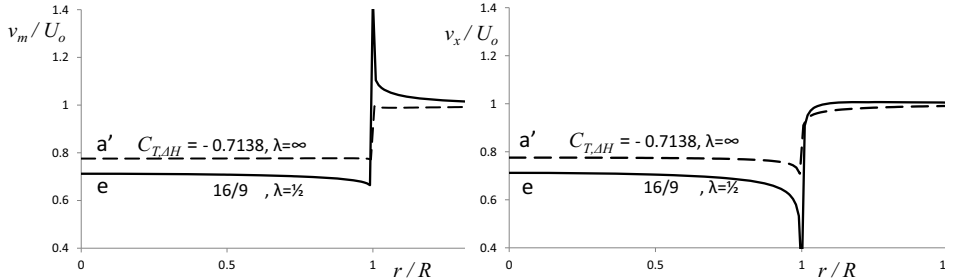


Figure 6.11: The velocity distribution at the disc for the flow states shown in figure 6.10. Left is shown the velocity in the meridional plane,  $|v_{m,d}| = \sqrt{v_x^2 + v_r^2}$ , right the axial velocity.

gives a uniform absolute velocity  $|v|$  upstream of disc  $a'$ . Figure 6.11 shows the values of the axial velocity component at the disc as well as the absolute value of the velocity vector in the meridional plane:  $|v_{m,d}| = \sqrt{v_x^2 + v_r^2}$ .

**6.4.4. The velocity at the disc.** In section 5.4.3 an explanation was sought for the absolute velocity at the Froude disc to be uniform for wind turbine discs and non-uniform for propeller discs. An explanation was found only partly, as the arguments (i) to (iii), mentioned in section 5.4.3, appear to be insufficient. These arguments, based on (5.21), did not yet include the effect of swirl. However,

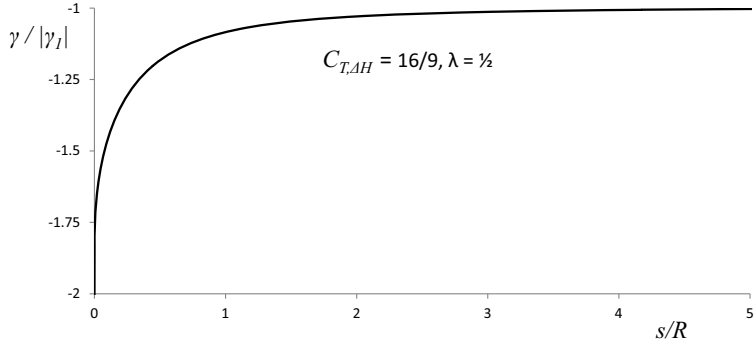


Figure 6.12: The distribution of  $\gamma$  at the wake boundary of the disc flow state e.

(5.21) is valid upstream of the disc as swirl occurs only in the wake. A constant pressure at the upstream side of the disc requires  $\partial v_{r,d} / \partial r = 0$ . With a constant pressure, the Bernoulli equation gives a constant  $|\mathbf{v}|$  at the upstream side. As  $v_x$  and  $v_r$  are continuous across the disc,  $\partial v_{r,d} / \partial r = 0$  gives a constant  $|v_{m,d}| = \sqrt{v_x^2 + v_r^2}$ . The analysis of  $\partial v_{r,d} / \partial s$  started in section 5.4.3 is continued here, with emphasis on arguments (iv), wake expansion or contraction, and (v), the non-uniform distribution of  $\gamma_\varphi$ .

A comparison of flow states a and c confirms that swirl plays no role, as also in the  $\lambda = 1$  flow state c  $|v_{m,d}| = \text{constant}$ . The same holds for wake expansion or contraction, as flow state e, having an expanding wake, shows the same characteristics as flow states b and d with contracting wakes.

By comparing the wind turbine flow states with the propeller flow states, the difference is in the distribution of  $\gamma_\varphi(s)$  with  $s$  measured along the boundary of the stream tube. Figure 6.12 shows the vorticity distribution of flow state e: the propeller disc with an expanding wake boundary. Apart from the sign of  $\gamma_\varphi$  it has the same characteristics as the distribution of flow state d in figure 6.8 and flow state b in figure 5.9:  $d\gamma_\varphi / ds$  does not change sign so there is no local maximum or minimum in  $\gamma_\varphi(s)$ . For the wind turbine disc flow states a and c, shown in figures 5.9 and 6.8, and a', not shown as it is almost identical to distribution a in figure 5.9, such a local minimum exists at  $s/R < 0.2$ .

Apparently this local maximum in the distribution of  $\gamma_\varphi$ , together with arguments (i) to (iii) mentioned in section 5.4.3, cause  $v_m$  to be uniform for wind turbine discs. A detailed analysis of the difference in induction close to the disc edge by a vortex sheet with and without such a local maximum or minimum, has to show why  $\partial v_{r,d} / \partial s = 0$  when such a maximum/minimum exists, and  $\neq 0$  when this does not exist. This is left for future research.

**6.4.5. Momentum balance per annulus.** The balance for the stream tube is defined by (6.15). In this equation the pressure acting at the stream tube boundary is absent as discussed in section 5.2. This is confirmed by the calculations for flow state c: the force in  $x$  direction resulting from the pressure

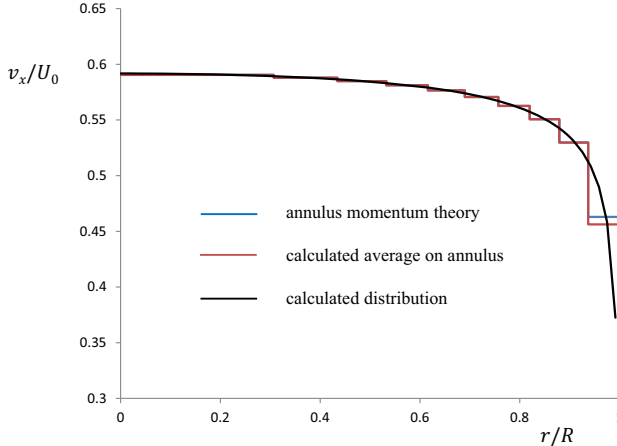


Figure 6.13:  $v_x$  at the disc for load case c with  $C_{T,\Delta H} = -8/9$  and  $\lambda = 1$ : the calculated distribution, the calculated average per annulus and the result from the momentum balance per annulus. The two annuli lines coincide except in the outboard annulus.

integrated along the wake boundary for  $-25 < x/R < 25$  is 0.2% of the non-conservative disc load  $C_{T,\Delta H}$  for the load case  $C_{T,\Delta H} = -8/9$  and  $\lambda = 1$ . When applying the momentum balance to an annulus instead of the entire stream tube, the same procedure is applied as in section 5.4.5 using the equations in section 5.2.4. Figure 6.13 shows the distribution of  $v_{x,d}$  resulting from the flow field calculation, the associated average value per annulus and the value resulting from (5.16) and (5.17). Figure 6.13 shows the result: as in figure 5.13 the calculated average per annulus coincides everywhere except at the disc edge with the momentum theory value. This confirms the results from the Froude discs in chapter 5: the annuli cannot be assumed as independent, as the pressure field contributes to the axial momentum exchange leading to the non-uniform distribution of  $v_{x,d}$ .

## 6.5. The role of swirl

The ratio in (6.23) is the ratio between the left-hand sides of the momentum balance (6.21) and energy balance (6.22) or, in other words, between the total load exerted on the flow in the stream tube control volume and the non-conservative load which is the load performing work. By this, (6.23) is equivalent to (5.13) which shows how conservative forces in the momentum balance cause the induced velocity at the disc to deviate from Froude's result that it is the average of the velocities far up- and downstream. Inspection of the pressure distributions contributing to the momentum balance as shown in figure 6.1 and listed in section 6.2.5 shows that:

- all distributions appear in the momentum balance (6.18) with (b), (c) and (e) cancelling each other apart from the remaining ( $c_{\text{expansion}}$ ) or ( $b_{\text{contraction}}$ ),

- distributions (a) and (d) appear in the energy balance (6.9), so are non-conservative,
- distributions (b), (c) and (e) do not appear in the energy balance, so are conservative.

Direct evaluation of  $(a+d+b_{\text{contraction}})$  or  $(c_{\text{expansion}})$  for the counter of the ratio  $T_{\text{total}}/T_{\text{cons}}$  in (5.13) and  $(a+d)$  for the denominator returns (6.23). The difference between the momentum and energy balances for the discs of Froude and Joukowsky is caused by the swirl-related pressure in the far wake: the conservative  $(b_{\text{contraction}})$  or  $(c_{\text{expansion}})$  and the non-conservative  $(d)$ .

The swirl related pressure distributions (b) and (c) are conservative as the gradient of the pressure and azimuthal velocity results in a conservation of potential and kinetic energy:  $\partial(p + \frac{1}{2}\rho v_\varphi^2)/\partial r = 0$  as is best illustrated by the flow without wake expansion or contraction, analysed in section 6.3.2. Still swirl has an impact on the energy balance by distribution (d). The change of  $H$  from undisturbed to its value in the far wake is given by (6.9) with the first term at the right-hand side expressing the change in kinetic energy and the second term, being the pressure (d), the change in potential energy.

The conclusion is that swirl does not contribute to a change in energy level of flow particles, expressed in  $H$ , but affects the performance through swirl-induced changes in pressure. These changes modify the shape and strength of the wake boundary vortex sheet compared with the no-swirl results of Froude discs, by which the mass flow through the disc decreases for increasing swirl. Although swirl is an essential component of disc flows, it leads to a loss of performance which is minimized by choosing  $\lambda$  as high as possible.

## 6.6. Comparison of the Joukowsky and Betz-Goldstein solutions

A comparison of the  $|C_{p,\max}| - \lambda$  curve for wind turbine discs having a Joukowsky circulation distribution with discs having a Betz-Goldstein distribution of the circulation is shown in figure 6.14. As shown by Okulov and Sørensen (2008) and Okulov (2014) the original Betz-Goldstein solution for a rotor with a finite number of blades resulted in  $|C_{p,\max}| = 1$ , as the pitch of the helicoidal wake was based on the undisturbed velocity. With the pitch based on the velocity in the rotor plane, Okulov (2014) showed that  $|C_{p,\max}|$  reaches the well-known Betz-Joukowsky maximum  $16/27$  for high  $\lambda$ . Expansion of this solution to a rotor with an infinite number of blades is shown in figure 3 of Okulov (2014). An alternative solution is published in Wood (2015) where the Goldstein formulation is adapted to allow for non-zero torque when  $\lambda \rightarrow 0$ . A comparison of the Joukowsky maximum  $|C_p|$  curve and corresponding Betz-Goldstein-Okulov/Wood curves is given in figure 6.14. The Joukowsky distribution gives higher  $|C_{p,\max}|$  than the Betz-Goldstein-based distributions, with the difference vanishing for higher  $\lambda$ . This is confirmed by Okulov and Sørensen (2010) where rotors with a finite number of blades having a Joukowsky and Betz-Goldstein-based distribution have been compared.

## 6.7. Evaluation

The momentum theory including swirl developed in this chapter solves the problem left by some other momentum theories, that the efficiency  $|C_p|$  of a wind

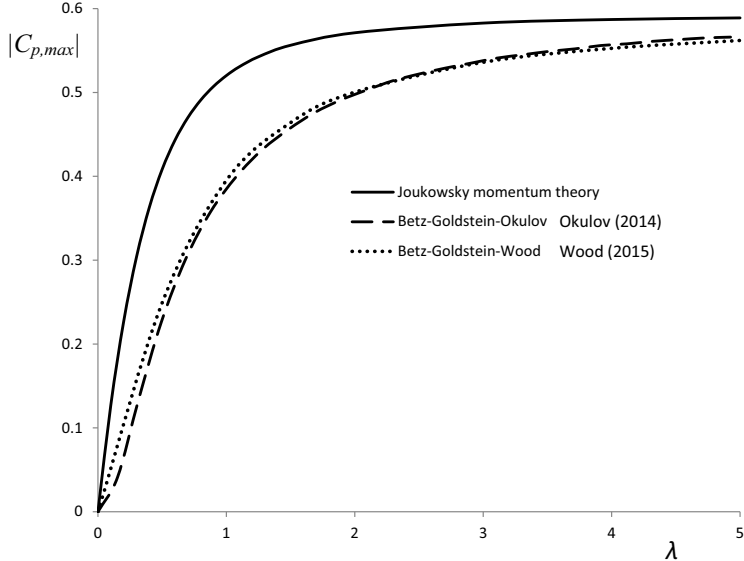


Figure 6.14: The Joukowsky actuator disc  $|C_{p,max}|$  compared with the Betz-Goldstein  $|C_{p,max}|$  solutions of Okulov (2014) and Wood (2015) for rotors with an infinite number of blades.

turbine disc becomes infinite when  $\lambda \rightarrow 0$ . The difference is in the treatment of the singular flow inherent to a vortex at the disc and wake axis with an infinitely small core. Now this core is included in the momentum balance, the singular contributions to the momentum balance annihilate each other, giving  $|C_{p,max}| \rightarrow 0$  for  $\lambda \rightarrow 0$ . The same holds for propeller discs. With this result question Q10, listed in section 1.4, is answered.

Question Q11 is answered by the same momentum theory. The product of  $\Omega$  and wake angular velocity is a measure for the work done by the force field, so swirl is essential. At the same time the swirl related pressure field acts as a conservative contribution to the momentum balance, giving a lower performance compared with disc flows without swirl. Swirl does not affect the energy content of a volume of flow as the change in kinetic energy is compensated by a change in pressure, keeping  $H$  the same. Swirl represents a loss in performance by the angular momentum, not by a change in kinetic energy.

As wind turbine discs and propeller discs are treated simultaneously, some characteristic differences have been observed, providing an answer to Q12. For all wind turbine discs the velocity in the meridian plane at the disc is uniform, so does not depend on  $r/R$ . For propeller discs this velocity is non-uniform. For a wind turbine disc, the distribution of the vortex sheet strength  $\gamma$  along the wake boundary shows a local maximum at a small distance after its leading edge, while the distribution of  $\gamma$  for propeller discs shows a smooth decrease from the leading edge to the far wake. A remarkable correspondence is that for very low  $\lambda$  not only the wind turbine wake expands, but also the propeller wake.

## Special topics: Conservative loads at a thick disc and blade tip

### 7.1. Introduction

So far only infinitely thin actuator discs and rotor blades modelled as lifting or actuator lines have been treated, carrying only radial vorticity. In this chapter two flows are discussed in which the other components of bound vorticity play a role. In section 7.2 the actuator disc has a non-zero thickness containing axial bound vorticity. Section 7.3 treats a rotor blade with non-zero chord where azimuthal bound chordwise vorticity plays a role. For the thick disc, the disc force field is sought which generates a Rankine vortex: a solid body rotation of the vortex core and potential vortex flow around it. For the rotor blade the load near the tip of a wind turbine rotor blade is studied, to find an explanation for the phenomenon that sometimes the tip vortex moves inboard after being released, before wake expansion drives it outboard. In both flows conservative forces are present, acting on the axial or azimuthal bound vorticity. This chapter is based on [van Kuik et al. \(2014\)](#) presenting a more detailed treatment of the same topics.

### 7.2. The generation of a Rankine vortex

**7.2.1. Wu's actuator disc equation.** [Wu \(1962\)](#) has formulated the axisymmetric actuator disc equation of motion expressed in the Stokes' stream function  $\Psi$  and circulation  $\Gamma$ . The actuator disc is placed normal to the undisturbed flow  $U_o$ , having an axisymmetric but otherwise arbitrary load distribution rotating with an angular velocity  $\Omega$ . Since the flow field induced by the force field is axisymmetric, it is possible to use the three-dimensional Stokes stream function  $\psi$ . [Breslin and Andersen \(1994\)](#) present an extensive discussion on Wu's equation as the authors consider his publication 'a landmark paper'. Here it suffices to say that it is the normal component of the Euler equation (2.3):

$$\frac{\partial H}{\partial n} = \mathbf{e}_n \cdot \mathbf{f} - \rho v_s \omega_\varphi + \rho v_\varphi \omega_s \quad (7.1)$$

with all kinematic terms expressed in  $\psi$  and  $\Gamma$ . Furthermore  $H$  is expressed in  $\Gamma$  using (4.4) resulting in:

$$\frac{\partial^2 \psi}{\partial x^2} + \frac{\partial^2 \psi}{\partial r^2} - \frac{1}{r} \frac{\partial \psi}{\partial r} = \frac{1}{2\pi} \frac{\partial \Gamma}{\partial \psi} \left( \Omega r^2 - \frac{\Gamma}{2\pi} \right) - \frac{r}{\rho} \frac{f_n}{v_s}. \quad (7.2)$$

The last term  $f_n$  is the same as the normal component of (4.7), being a conservative force. Without the  $f_n$  term, (7.2) is known as the [Bragg and Hawthorne \(1950\)](#) equation. [Wu \(1962\)](#) suggests that  $f_n$  may be neglected, as he considers

this to be the component of the axial force density normal to the stream tube. A significant value of  $f_n$  then requires a large radial velocity component at the disc, which is not present in general.

To test this hypothesis a solution of Wu's equation was sought without wake expansion of contraction, so with  $v_r = 0$ . There are two possibilities for a wake generated by a disc force field with a constant radius, as becomes clear by combining the Bernoulli equation (6.5) with the expression for radial pressure equilibrium (6.6):

$$\frac{\partial v_x^2}{\partial r} = 2 \left( \Omega - \frac{v_\varphi}{r} \right) \frac{\partial(rv_\varphi)}{\partial r}. \quad (7.3)$$

A flow with  $\partial v_r / \partial r = 0$  requires a constant  $v_x$  which can be established either as a rotating body, so  $v_\varphi = \Omega r$ , or as the Joukowsky flow  $v_\varphi = \Gamma / (2\pi r)$ . A Rankine vortex combines both flows: the kernel of it has a solid body rotation whereas outside the kernel the flow is a vortex flow with  $v_\varphi \propto r^{-1}$ .

**7.2.2. The force field required to generate a Rankine vortex.** The Rankine vortex flow is found to be an exact solution of Wu's equation. The kinematics of the flow generated by a force field distributed at a disc with thickness  $\epsilon$ , with a linear increase of the swirl at the disc, are given by:

$$\left. \begin{array}{lcl} \psi & = & \frac{1}{2} U_0 r^2 \\ v_\varphi & = & \begin{cases} \mathcal{C}(x)\Omega r & r \leq \delta \\ \mathcal{C}(x)\Omega \frac{\delta^2}{r} & r > \delta \\ x/\epsilon & 0 < x < \epsilon \end{cases} \\ \mathcal{C}(x) & = & \begin{cases} 1 & x \geq \epsilon \\ 0 & x \leq 0. \end{cases} \end{array} \right\} \quad (7.4)$$

where  $\delta$  is the radius of the vortex core. The flow is sketched in figure 7.1. The vorticity enclosed by the disc volume is derived by applying (A.8), with the notation  $\boldsymbol{\omega} = [\omega_x, \omega_r, \omega_\varphi]$ :

$$\boldsymbol{\omega}_d = \begin{bmatrix} 2\Omega \frac{x}{\epsilon} \\ -\Omega \frac{r}{\epsilon} \\ 0 \end{bmatrix}_{r \leq \delta} \quad \boldsymbol{\omega}_d = \begin{bmatrix} 0 \\ -\Omega \frac{\delta^2}{r\epsilon} \\ 0 \end{bmatrix}_{r > \delta}, \quad (7.5)$$

which gives, after integration across the disc thickness, the vortex sheet strength  $\gamma_d = \int \boldsymbol{\omega}_d dx$ :

$$\boldsymbol{\gamma}_d = \begin{bmatrix} \Omega \epsilon \\ -\Omega r \\ 0 \end{bmatrix}_{r \leq \delta} \quad \boldsymbol{\gamma}_d = \begin{bmatrix} 0 \\ -\Omega \frac{\delta^2}{r} \\ 0 \end{bmatrix}_{r > \delta}. \quad (7.6)$$

For the flow outside the disc volume the solution (7.4) satisfies Wu's equation (7.2), as is checked by substitution. At the disc itself, this substitution provides the expression for  $f_n$ , with  $v_s = U_0$  and  $\partial/\partial\Psi = (rU_0)^{-1} \partial/\partial r$ . It is clear that  $f_n$  is purely radial, so  $f_n = f_r$ . At the disc volume,  $f_\varphi$  is determined by (4.2) after which  $f_x$  by (4.1). For  $r > \delta$  this gives an expression for  $f_x$  that does not vanish for  $r \rightarrow \infty$ . This is corrected by adding a constant force field  $f_x = -\rho(\Omega\delta)^2/\epsilon$

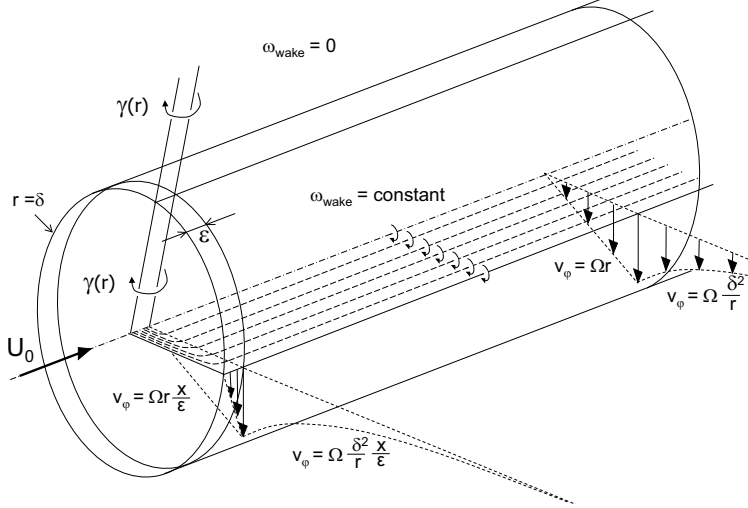


Figure 7.1: An exact solution of Wu's equation: the generation of a Rankine vortex, with core radius  $\delta$ .

for  $0 \leq r < \infty$ . This has no impact on the flow, since it adds a constant pressure downstream of the disc. It is a conservative force field satisfying (2.19) with the potential  $\mathcal{F} = \rho(\Omega\delta)^2 x/\epsilon$ . The result is, in dimensionless form:

$$\frac{\mathbf{f}}{\rho\Omega^2 r} = \begin{bmatrix} \frac{r^2 - \delta^2}{r\epsilon} - \frac{xr}{\epsilon^2} \\ \frac{2x}{\epsilon} \left(1 - \frac{x}{\epsilon}\right) \\ \frac{U_o}{\Omega} \frac{1}{\epsilon} \end{bmatrix}_{r \leq \delta} \quad \frac{\mathbf{f}}{\rho\Omega^2 r} = \begin{bmatrix} -\frac{xr}{\epsilon^2} \left(\frac{\delta}{r}\right)^4 \\ 0 \\ \frac{U_o}{\Omega r} \frac{\delta^2}{r\epsilon} \end{bmatrix}_{r > \delta}. \quad (7.7)$$

The resultant expressions for the disc load  $\mathbf{F}$  are obtained by integration of  $\mathbf{f}$  across the thickness  $\epsilon$ :

$$\frac{\mathbf{F}}{\rho(\Omega r)^2} = \begin{bmatrix} \frac{1}{2} - \left(\frac{\delta}{r}\right)^2 \\ \frac{\epsilon}{3r} \\ \frac{U_o}{\Omega r} \end{bmatrix}_{r \leq \delta} \quad \frac{\mathbf{F}}{\rho(\Omega r)^2} = \begin{bmatrix} -\frac{1}{2} \left(\frac{\delta}{r}\right)^4 \\ 0 \\ \frac{U_o}{\Omega r} \left(\frac{\delta}{r}\right)^2 \end{bmatrix}_{r > \delta}. \quad (7.8)$$

The solution satisfies the equation of motion (4.7), as is clear by substitution of (7.4) and (7.5) in (4.7).  $F_x$  and  $F_\varphi$  are independent of the thickness  $\epsilon$ .  $F_{r,r>\delta} = 0$  but  $F_{r,r<\delta}$  is  $O(\epsilon)$ , and contributes to the disc load when  $\epsilon \neq 0$ .

**7.2.3. Interpretation of the radial component of the load.** Inspection in the rotating frame of reference is possible by writing (4.7) as  $\mathbf{f} = -\rho \mathbf{v}_{rot} \times$

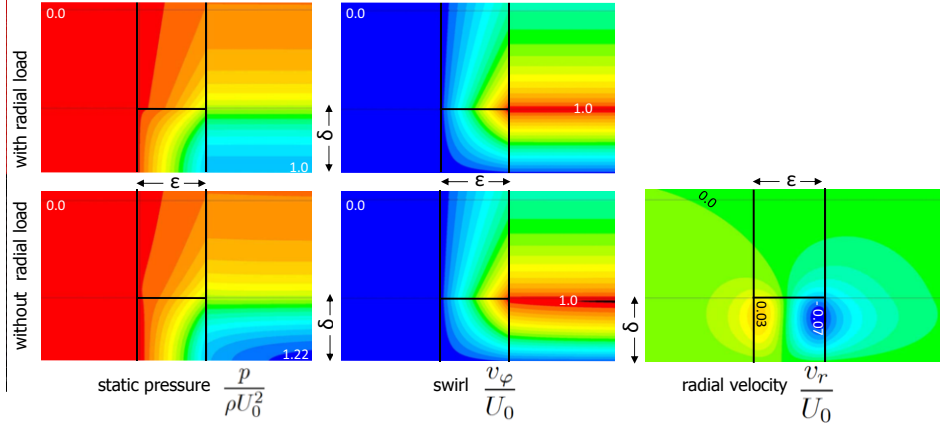


Figure 7.2: The generation of a Rankine vortex flow by the force field (7.7) with and without  $f_r$ . Shown is the meridian plane with the undisturbed flow  $U_0$  coming from left. This disc is between the vertical lines. The kernel diameter  $\delta$  equals the thickness  $\epsilon$ . Left: the pressure, middle: the swirl, right: radial velocity (not shown for  $f_r = 0$  since  $v_r = 0$  everywhere).

$\omega_{rot} + \mathbf{v}_{rot} \times 2\Omega$ , and applying this to (7.7). This shows that  $f_r$  has a Kutta-Joukowsky as well as Coriolis part, with:

$$f_{r,K-J} = 2\rho \left( 1 - \left( \frac{x}{\epsilon} \right)^2 \right) \Omega^2 r \quad (7.9)$$

$$f_{r,C} = -2\rho \left( 1 - \frac{x}{\epsilon} \right) \Omega^2 r. \quad (7.10)$$

In the inertial frame of reference the radial component of the Euler equation (2.1) with  $v_r = 0$  and  $\partial \mathbf{v}/\partial t = 0$  enables the interpretation of  $f_r$ :  $\partial p/\partial r - f_r = \rho v_\varphi^2/r$ . Evaluation of  $\rho v_\varphi^2/r$  with (7.4) gives:

$$\begin{aligned} \frac{1}{\rho} \left( \frac{\partial p}{\partial r} - f_r \right) &= \Omega \frac{\partial (rv_\varphi)}{\partial r} - v_\varphi \frac{\partial v_\varphi}{\partial r} \\ &= \Omega^2 r \mathcal{C}(x) (2 - \mathcal{C}(x)). \end{aligned} \quad (7.11)$$

In the wake  $f_r = 0$  and  $\mathcal{C} = 1$ , so  $\rho^{-1}\partial p/\partial r = \Omega^2 r = v_\varphi^2/r$  satisfying the centripetal balance (6.6). This is not the case at the disc, where  $\mathcal{C}(x) = x/\epsilon$  results in a right-hand side of (7.11) unequal to  $\rho v_\varphi^2/r$ . However, at the disc  $f_r$  is non-zero, and substitution of  $f_r$  in (7.11) gives:

$$\frac{1}{\rho} \frac{\partial p}{\partial r} = \Omega^2 r \mathcal{C}^2(x) = \frac{v_\varphi^2}{r}, \quad (7.12)$$

which shows that the radial force density is required to restore the centripetal balance at the disc.

**7.2.4. Numerical assessment of the impact of the radial load.** The analytical solution shows that for  $r \leq \delta$   $f_r \neq 0$ , but does not contribute to the disc load  $F_r = \int f_r dx$  when  $\epsilon \rightarrow 0$  since  $f_r$  remains finite in this limit. The question whether omitting  $f_r$  is allowed in a flow calculation is still unanswered. To investigate this, the flow has been calculated with the CFD code Fluent, see van Kuik et al. (2014) for more information. The undisturbed flow has been set to  $U_0 = \Omega\delta$ . The thickness  $\epsilon$  of the disc has been set to two values:  $\epsilon = 0.05\delta$  and  $1.0\delta$ . The force density distribution (7.7) is applied, but one time with and one time without the radial force  $f_r$ . For the thin disc with  $\epsilon = 0.05\delta$  the results with and without  $f_r$  are graphically almost indistinguishable, and not shown here: both calculations give the flow field (7.4) so the radial load does not matter. For the thick disc with  $\epsilon = \delta$  the results with and without  $f_r$  clearly show differences as shown in figure 7.2. With the radial load included, see the upper row, the analytical solution is reproduced exactly, and downstream of the disc the flow does not change any more. In the absence of  $f_r$  another flow field results, displayed in the lower row. The contrast with the analytical solution is observed in the wake, which is not fully developed immediately downstream of the disc, but is most visible in the plot of the radial velocity. The analytical solution gives  $v_r = 0$  in the entire flow field, but  $v_r$  in absence of  $f_r$  has a maximum value  $v_r/U_0 \approx 0.07$ .

In conclusion the numerical analysis shows that  $F_x$  and  $F_\varphi$  do not define the flow uniquely. For the thick disc,  $F_r$  satisfying (7.7) needs to be added to reproduce the analytical solution, whereas  $F_r = 0$  results in another flow solution with non-zero  $v_r$ . For thin discs  $F_r = \int_\epsilon f_r dx$  is negligible so it has no impact. Further interpretation of  $f_r$  and  $F_r$  is presented in section 7.4.

### 7.3. The rotor blade

**7.3.1. Inboard motion of a tip vortex.** Akay et al. (2012) and Micallef (2012); Micallef et al. (2013, 2014) report experiments on two two-bladed rotors of 2m diameter in the 3m diameter Open Jet Facility of TU Delft, with emphasis on the root and tip region. Schepers and Snel (2007) and Schepers et al. (2014) report experiments on a 4.5m diameter three-bladed rotor called Mexico<sup>1</sup> in the 9.5\*9.5 m<sup>2</sup> open test section of the German Dutch Wind tunnel. Xiao et al. (2011) report detailed tip vortex experiments on a 1.25m diameter model of the NREL UAE phase VI wind turbine described by Hand et al. (2001), in an open test section of 3.2m diameter. The flow near the blade tip of these rotors is such that the tip vortex, when leaving the tip, moves inboard before the wake expansion moves the vortex to a larger radius. The tendency of any tip vortex to move inboard is known from wing aerodynamics: the distance between the tip vortices in the far wake is less than the span of the wing, see figure 3.3, as during the concentration of the vorticity in two tip vortices the first integral moment with respect to the symmetry plane is invariant, see Batchelor (1970, p. 591). This corresponds with a centroid of vorticity at 70 – 90% of the half-span of the wing, depending on the load and circulation distribution. Qualitative considerations based on the Biot-Savart induction rules make clear that the inboard induction is caused by the chordwise vorticity at the tip since all other bound or free wake

---

<sup>1</sup>Measurements and EXperiments In COntrolled conditions

vorticity components cannot induce such an inboard velocity. As the downward movement of the tip vortices ( $\Delta x$  in figure 3.3) is related to the downward load exerted by the wing, being the reaction force of the lift, the question is raised whether the inboard motion  $\Delta y$  is related to a spanwise wing load. As a side step this is evaluated here for the elliptic wing.

### 7.3.2. Side step: conservative, spanwise load on an elliptic wing.

The wing is placed in the Cartesian coordinate system of figure 3.3 with the span  $b$  ranging from  $y = -b/2$  to  $y = b/2$ . The chord length has an elliptical distribution:  $c(y)/c_{\max} = \sqrt{1 - (2y/b)^2}$ . The undisturbed velocity  $U_0$  is in the  $z$ -direction with the positive  $z$  pointing downstream, the  $x$  coordinate points downwards. The elliptic planform gives an elliptic distribution of the bound circulation  $\Gamma(y)/\Gamma_{\max} = \sqrt{1 - (2y/b)^2}$ , where  $\Gamma_{\max}$  is the circulation around the wing at mid-span position. The velocity perpendicular to the undisturbed velocity, the downwash, is  $v_z = -\Gamma_{\max}/(2b)$ . The chordwise vorticity is given by  $\gamma_c = -d\Gamma/dy$  so integration of the spanwise component of the Kutta-Joukowsky load on the surface  $A$  of the half-wing gives:

$$\mathcal{S} = -\rho \int_A \mathbf{e}_y \cdot \mathbf{v} \times \boldsymbol{\gamma} dx dz = -\rho \frac{\Gamma_{\max}}{2b} \int_b c d\Gamma \quad (7.13)$$

$$= -\frac{\rho}{4} \Gamma_{\max}^2 \frac{c_{\max}}{b}. \quad (7.14)$$

Comparison with the induced drag,  $D = -\pi\rho/(8\Gamma_{\max}^2)$ , shows that the ratio  $\mathcal{S}/D = 2c_{\max}/(b\pi)$ . For an aspect ratio  $b/c_{\max} = 10$  and lift coefficient  $C_L = 1$ , the spanwise force on the half wing is 6% of the induced drag and 0.5% of the lift of the entire wing.  $\mathcal{S}$  is directed inboard, in agreement with the inboard motion of the wake vorticity.  $\mathcal{S}$  is perpendicular to the flying path so it does not convert power. It is a conservative force which is not a ‘necessary force’ like the lift and induced drag. For a very slender wing, so for  $c_{\max}/b \rightarrow 0$ ,  $\mathcal{S}$  vanishes as the bound chordwise vorticity vanishes, like  $F_r$  vanishes for the disc thickness  $\epsilon \rightarrow 0$  in section 7.2.

### 7.3.3. Conservative and non-conservative blade loads.

The vorticity dynamics involved in the creation and release of the tip vortex of a rotor blade are less clear as the wake expansion or contraction drive the tip vorticity outboard or inboard. For a propeller both effects add up but for a wind turbine rotor blade the inboard movement of the tip vortex may be cancelled by the outboard convection due to the wake expansion. It is expected that the inboard motion as observed in the mentioned experiments, is connected to a radial tip load acting on the bound chordwise vorticity as shown in figure 7.3. For simplicity it shows the most simple rotor blade with a constant cross-section  $C$  being a symmetric aerofoil without pitch or twist angle. This is not an optimal rotor design, but although not self-starting, it acts as a wind turbine rotor once  $\Omega R/U_0$  is sufficiently high. By the chosen simple configuration the blade can carry only radial and azimuthal vorticity components, which suffices for the present analysis. Figures 7.3 and 7.4 show the blade as a surface with curved lines of vorticity. Milne-Thomson (1966, §10.61) pays attention to the in-plane component of the Kutta-Joukowsky load appearing when the lifting surface contains non-parallel vorticity lines. Because

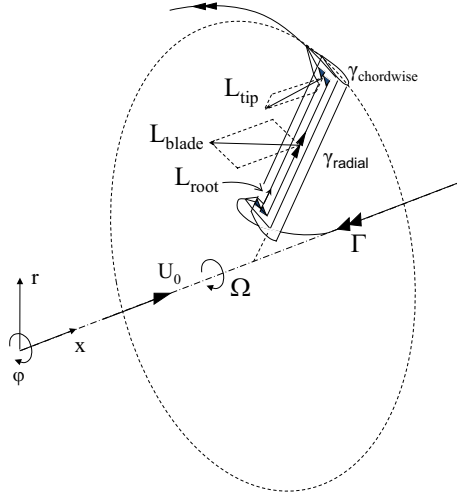


Figure 7.3: Wind turbine rotor blade bound vorticity, with loads acting on the flow. The sign conventions are similar to figures 2.2 and 4.1: all vectors are in positive direction except  $\Gamma$  at the axis and  $\gamma_{chordwise}$ . The loads are drawn assuming  $v_x > 0$ ,  $v_{\varphi,rot} < 0$ ,  $v_r = 0$  near the root and  $v_r < 0$  near the tip.

of the limited importance for wings his analysis is restricted to the observation that the spanwise load is non-zero. Here we analyse the load on both components of the bound vorticity.

The load acting on a blade cross section  $C$  is given by 4.14. With  $\omega$  expressed in its components the lift  $\mathbf{L}$  is:

$$\mathbf{L} = -\rho \int_C \mathbf{v}_{rot} \times \mathbf{e}_r \omega_r dC - \rho \int_C \mathbf{v}_{rot} \times \mathbf{e}_\varphi \omega_\varphi dC. \quad (7.15)$$

The first integral gives the load on the radial vorticity, contributing to the rotor thrust and torque. The second integral in (7.15) is the lift on azimuthal vorticity. Evaluated in the  $(s, n, \varphi)$  system using (2.5),  $\mathbf{v}_{rot} \times \mathbf{e}_\varphi \omega_\varphi = \mathbf{v} \times \mathbf{e}_\varphi \omega_\varphi = -\mathbf{e}_n v_s \omega_\varphi$  so the second integral gives the load is in the meridian plane normal to the stream tube, by which it is indicated as  $\mathbf{L}_n$ .

In order to distinguish conservative and non-conservative contributions to  $\mathbf{L}$ ,  $\nabla \times \mathbf{L} = \int \nabla \times \mathbf{f} dC$  is evaluated in the  $(s, n, \varphi)$  system, giving:

$$\iint_C \left[ \mathbf{e}_s \left( \frac{\partial (rf_\varphi)}{r \partial n} - \frac{\partial f_n}{r \partial \varphi} \right) + \mathbf{e}_n \left( \frac{\partial f_s}{r \partial \varphi} - \frac{\partial f_\varphi}{\partial s} \right) + \mathbf{e}_\varphi \left( \frac{\partial f_n}{\partial s} - \frac{\partial f_s}{\partial n} \right) \right] r d\varphi ds. \quad (7.16)$$

Despite the derivatives to  $\varphi$  and  $s$  being non-zero, they vanish after integration, so:

$$\frac{1}{\rho} \nabla \times \mathbf{L} = \int_C \left[ \mathbf{e}_s \frac{\partial (rf_\varphi)}{r \partial n} - \mathbf{e}_\varphi \frac{\partial f_s}{\partial n} \right] dC = \mathbf{e}_s \frac{\partial (rL_\varphi)}{r \partial n} - \mathbf{e}_\varphi \frac{\partial L_s}{\partial n}. \quad (7.17)$$

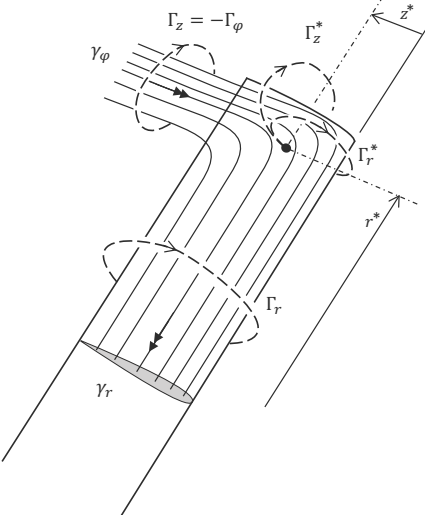


Figure 7.4: Schematic representation of bound and free vorticity of the wind turbine blade tip of figure 7.3.

$\mathbf{L}_n$  is not included in (7.17) so it is conservative, while the other components of  $\mathbf{L}$  are non-conservative. With  $z$  measured from the leading edge to the trailing edge  $0 \leq z \leq c$ . Comparison of (7.15) and (7.17) allows a decomposition of  $\mathbf{L}$  as:

$$\mathbf{L}_{non-cons} = -\rho \int_C \mathbf{v}_{rot} \times \mathbf{e}_r \omega_r dC = -\rho \bar{\mathbf{v}}_{rot} \times \int_0^c \mathbf{e}_r \gamma_r dz \quad (7.18)$$

$$\mathbf{L}_{cons} = \mathbf{L}_n = -\rho \int_C \mathbf{v} \times \mathbf{e}_\varphi \omega_\varphi dC = -\rho \bar{\mathbf{v}} \times \int_0^c \mathbf{e}_\varphi \gamma_\varphi dz. \quad (7.19)$$

with  $\bar{\mathbf{v}}$  and  $\bar{\mathbf{v}}_{rot}$  being the average values across the thickness of the cross section  $C$ . Furthermore  $\int_{leading\ edge}^{trailing\ edge} rd\varphi$  has been replaced by  $\int_0^c dz$ . The non-conservative part of  $\mathbf{L}$  acts upon the spanwise or radial vorticity, while the conservative  $\mathbf{L}_n$ , having an axial as well as radial component, acts upon the chordwise vorticity.

The relation between both components is now expressed in terms of the circulation  $\Gamma$ . For any lifting surface the well known relation between the change of spanwise circulation and trailing vorticity is (3.1). Expressed in the rotor coordinates of figures 7.3 and 7.4 this becomes  $\gamma_\varphi = -\partial \Gamma_r / \partial r$ . The subscript  $r$  indicates that  $\Gamma$  is defined in a plane normal to a radius, enclosing radial  $\gamma$ . Similarly the circulation  $\Gamma_\varphi$  is defined in a plane normal to the chordwise direction, enclosing azimuthal  $\gamma$ , see figure 7.4. Inspection of the derivation of this relation as presented by e.g. Lighthill (1986) shows that it also holds at the blade surface itself with  $\Gamma_r^*$  measured from the leading edge:  $\gamma_\varphi^* = -\partial \Gamma_r^* / \partial r$ . When measured from a local value of  $r^*$  to the tip then  $\Gamma_\varphi^*(r) = \int_{r^*}^R \gamma_\varphi dr$  or  $\gamma_\varphi^* = \partial \Gamma_\varphi^* / \partial r$ . Combining

both expressions for  $\gamma_\varphi^*$  gives  $\gamma_\varphi^* = -\partial\Gamma_r^*/\partial r = \partial\Gamma_\varphi^*/\partial r$  or:

$$\frac{\partial(\Gamma_r^* + \Gamma_\varphi^*)}{\partial r} = 0, \quad (7.20)$$

in which  $\Gamma_r^* = \int_{* \text{ position}}^{\text{leading edge}} \gamma_r r d\varphi = \int_0^{z^*} \gamma_r dz$  and  $\Gamma_\varphi^* = \int_{r^*}^R \gamma_\varphi dr$ . Expressed in  $z$  this becomes  $\Gamma_z^* = -\Gamma_\varphi^* = \int_{r^*}^R \gamma_z dr$ . It provides a coupling between the radial vorticity in (7.18) and the azimuthal vorticity (7.19). With (7.20)  $\Gamma_z^* = \Gamma_r^*$  for a fixed chordwise position  $z^*$ , indicated in figure 7.4. By comparing this with (7.19) the expression for the local  $\mathbf{L}_{cons}^*$  becomes:

$$\mathbf{L}_{cons}^* = -\rho \bar{\mathbf{v}} \times \mathbf{e}_z \int_o^1 \Gamma_z^* d\frac{z}{c}. \quad (7.21)$$

The occurrence of a load acting on chordwise vorticity at the tip is known from measurements on helicopter and propeller model rotors. [Gray et al. \(1980\)](#) show the measured pressure distribution at the tip of a model rotor operating in hover, resulting in a significant increase of the normal force for  $r/R > 0.98$ . [Ragni et al. \(2011a,b\)](#) report propeller tip measurements using SPIV and CFD calculations showing details of the pressure distribution at the tip. A very good agreement between experimentally obtained and calculated tip pressure is shown in figure 8 of ([Ragni et al. \(2011b\)](#)), but no data for the integrated loads are given. As the pressure contours at the suction side of the propeller blade have the same sign, this results in a non-zero radial load after integration on the radially projected blade surface.

Here (7.21) will be evaluated using data from one of the TU Delft experiments described in detail in [Micallef \(2012\)](#), with emphasis on the axial as well as radial component.

**7.3.4. Experimental and numerical results for a model wind turbine rotor.** [Micallef \(2012\)](#) gives the details of the experiment with the 2m diameter, two-bladed TUD-B rotor in the 3m diameter Open Jet Facility of TU Delft. Figure 7.5 shows the almost cylindrical blade shape of the TUD-B rotor with a blunt tip surface having a zero pitch angle at  $r = R$ . All results concern the rotor operating at its optimal tip speed ratio  $\lambda = 7$  at a wind speed of 6 m/s. Figure 7.5 also shows the plane of observation and the coordinate systems. Besides the  $(x, r, \varphi)$  system defined in figure 7.3 also the local  $(x, z, r)$  system is used since it is convenient to express local flow properties in the chordwise coordinate  $z$ . Apart from the experimental data obtained by SPIV measurements, the CFD code implemented by [Herráez et al. \(2014a,b\)](#) and the vortex panel code developed by [Micallef et al. \(2013\)](#) are used to capture the tip flow in detail. A summary of these models is presented in [van Kuik et al. \(2014\)](#).

Figure 7.6 shows the measured and calculated radial flow in the plane of observation as defined in figure 7.5. At the tip a large difference in radial velocity at the pressure side of the blade tip ( $x < 0$ ) and suction side is visible, indicating chordwise vorticity bounded at the tip. This vorticity component is shown in figure 7.7 indicating high values for  $r/R > 0.97$ . This chordwise vorticity may be

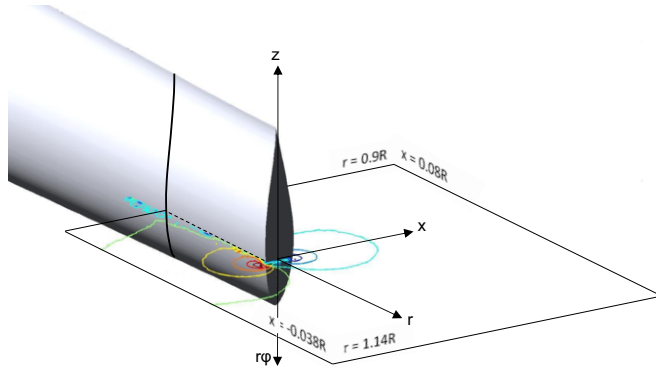


Figure 7.5: The geometry of the tip of the TUD-B rotor, the coordinate system and the plane of observation, used for the measurements and calculations. The isolines indicate the radial velocity. The square contour of the plane of observation is used to determine the chordwise bound circulation at various chordwise positions of the plane. The chordwise coordinate  $z$  is measured from the leading edge where  $z = 0$ .

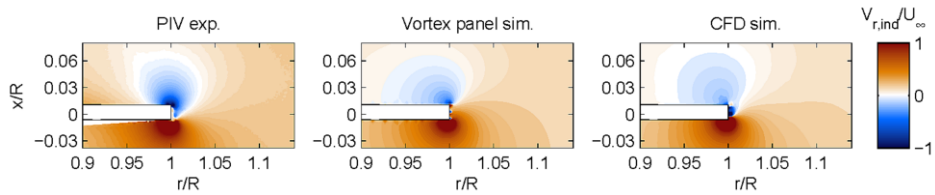


Figure 7.6: Comparison of the radial velocities in the plane through the quarter-chord tip position.

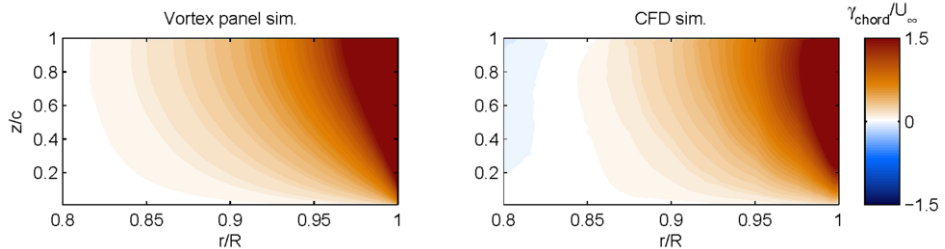


Figure 7.7: The chordwise vorticity determined by difference in radial velocities.

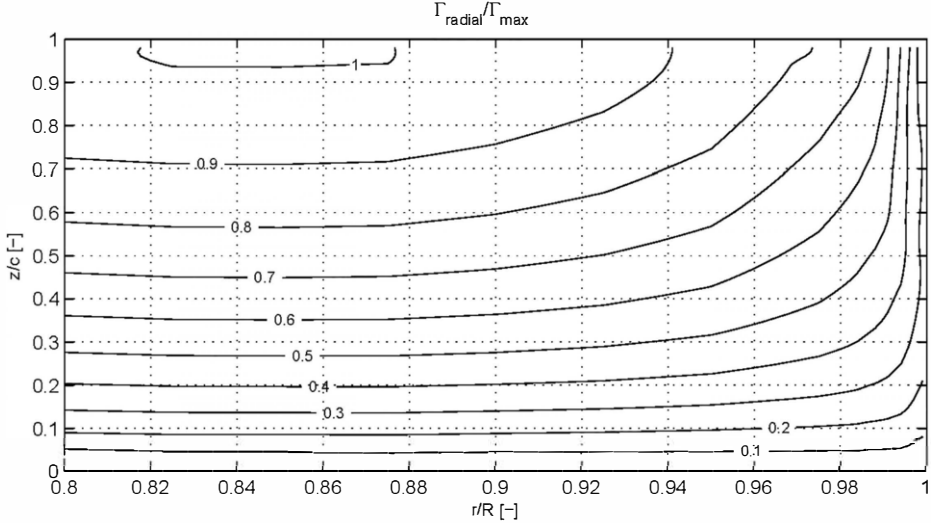


Figure 7.8: Iso-lines of constant percentage of the local circulation  $\Gamma_r^*/\Gamma_{r,\max}$  around the TUD-B rotor blade, determined by the CFD method. As  $\Gamma_r^* = \Gamma_z^*$  the iso-lines also give the circulation measured from the tip.

considered as the beginning of the tip vortex as shown in detail by [Micallef et al. \(2014, 2018\)](#).

Figure 7.8 shows how the circulation  $\Gamma_r^*$  measured around blade bound radial vorticity  $\gamma_r$  is connected to the circulation  $\Gamma_z^*$  measured around bound chordwise vorticity  $\gamma_\varphi$ , with a visual explanation of  $\Gamma_r^*$  and  $\Gamma_z^*$  in figure 7.4. The value of the iso-circulation lines gives the local circulation, measured from the leading edge divided by the maximum blade circulation. This maximum occurs at the trailing edge at  $r/R = 0.825$ . As  $\Gamma_r^*\Gamma_z^*$  for a fixed position  $r^*, z^*$ , the iso-lines give the value for  $\Gamma_r^*$ , measured along the chord from the leading edge, as well as  $\Gamma_z^*$ , measured along the radius from the tip to inboard. As an example at the trailing edge the spanwise circulation increases from 0 at  $r = R$  to  $\approx 0.9\Gamma_{r,\max}^*$  at  $r = 0.94R$ . In other words, 90% of the radial circulation leaves the blade as chordwise circulation in the outer 6% of the blade. The figure shows that a small amount of the circulation leaves the tip, see the iso-lines 0.1 and 0.2. This missing part is not analysed further, but it is unbound vorticity or the contribution of the flat tip surface to the bound circulation.

The measured and CFD-calculated velocity field is integrated along the contour displayed in figure 7.5, to obtain the circulation  $\Gamma_r^*(z)$  around the chordwise vorticity at  $r = 0.9R$  at 6 chordwise positions. Details of the procedure are given in [van Kuik et al. \(2014\)](#), with the results shown in the left part of figure 7.9. The two curves agree reasonably well.

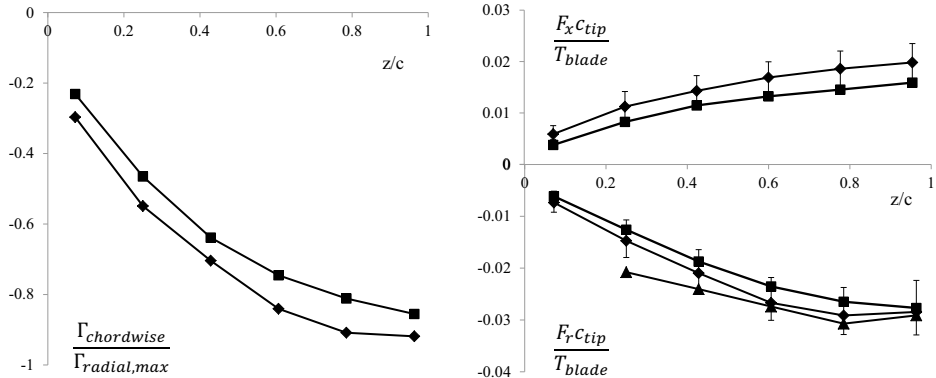


Figure 7.9: Left: chordwise circulation, right: axial and radial load. The squares show the K-J method applied to the CFD data. The diamond marker indicates the same applied to the experimental data. The triangles present the experimental momentum method. The error bars for the K-J experimental load show the sensitivity for the position to determine  $v_{ref}$ .  $T_{blade}$  is the thrust on a single blade. The sensitivity of the radial load for variations of the contour in the momentum method is 5% of the values indicated.

**7.3.5. Determination of the conservative tip load.** The conservative tip force (7.21), decomposed in the axial force  $F_x$  and radial force  $F_r$ , is determined by several means.

- Equation (7.21) gives the load on the chordwise vorticity for a certain radius so integration along  $r$  gives the total load. This is approximated by the following procedure. The force is calculated by chordwise integration of the Kutta-Joukowsky load  $-\rho \mathbf{v}_{ref} \times \boldsymbol{\Gamma}$  where the equivalent velocity  $\mathbf{v}_{ref}$  is the velocity in the  $(x; r)$  plane at a position close to the tip. The variation in the results by varying this position is shown by the error bars in figure 7.9, giving results for the CFD and experimental obtained data.
- The radial load  $F_r$  is obtained by direct integration of the pressure as calculated by the CFD code.
- Furthermore the radial load is found by applying a radial momentum balance using the measured velocity field based on a contour as shown in figure 7.5, however with  $r = R$  as inboard boundary instead of  $r = 0.9R$ . By doing so the pressure at the flat tip surface is the source term in the balance giving the radial load. The sensitivity for the choice of the contour is checked by varying the position of the other contour sides. The momentum method is described and applied in [del Campo et al. \(2013, 2014, 2015\)](#) where it is applied to determine the load on the radial circulation.

The results of figure 7.9 are integrated along the chord to obtain the normal and radial load given in table 7.1. The results agree reasonably well, with the pressure integrated radial load most deviating. The ratio of the radial force to the thrust of the blade has the same order of magnitude as the ratio of the spanwise force to

Table 7.1: The axial load  $F_x$  and radial load  $F_r$  at the tip, as % of  $T_{blade}$ . P, K-J and MOM refer to the pressure, Kutta-Joukowsky and momentum methods explained in section 7.3.5.

	CFD		Experiment	
	P	K-J	K-J	MOM
$F_x$		1.0	$1.3 \pm 0.3$	-
$-F_r$	1.2	1.8	$1.9 \pm 0.4$	$2.2 \pm 0.1$

the lift at one half of an elliptic wing calculated in section 7.3.2: 1 – 2%, so the contribution of the conservative tip loads to the overall rotor load is very small. However, when  $F_x$  and  $F_r$  are normalized by the thrust acting on the blade tip for  $r/R > 0.9$ , the order of magnitude changes to 10%.

**7.3.6. The tip vortex trajectory.** Besides the loads, the tip vortex trajectories are compared. Figure 7.10 shows the calculated trajectories in comparison with the measured values. The CFD-blade results corresponds to the CFD analysis discussed so far, the actuator line (CFD-AL) results are presented below<sup>2</sup>. The CFD-AL method is a standard actuator line method, applied including the tip correction proposed by Shen et al. (2005b). Both CFD results are obtained by taking the average position of 100 streamlines forming the tip vortex. For the panel code the trajectory is the vorticity filament that leaves the blade at the trailing edge of the tip. Although there are differences between the experimental data and calculated trajectories, the CFD-blade and panel code results confirm that the tip vortex moves somewhat inboard before expansion starts after approximately 30° azimuth angle after the  $c/4$  position. The CFD-AL line does not show any inboard movement. The wake expansion in CFD-AL starts immediately after the tip vortex is released, while this is delayed in CFD-blade. When the expansion part of CFD-blade is interpolated to  $r = R$  keeping the same slope for large  $\varphi$ , the equivalent delay in wake expansion compared to CFD-AL is 50° azimuth angle.

Since in the AL method all chordwise information is discarded, the bound chordwise vorticity and the loads acting on it are absent, so  $\mathbf{L}_{cons} = 0$ . The difference between the CFD-blade and CFD-AL lines in figure 7.10 is the difference in including or discarding conservative tip loads. So far both codes did not use any tip correction. In the next chapter a tip correction in combination with a model for the conservative tip load is treated, with emphasis on the tip vortex trajectory and the impact of a delayed wake expansion on the blade loads.

## 7.4. The role of conservative forces

In the previous sections three examples of conservative forces have been shown: the radial load on axial disc bound vorticity in section 7.2, the spanwise load on chordwise vorticity of an elliptic wing in section 7.3.2 and the axial and radial load on chordwise vorticity of a rotor blade in section 7.3.3. A common

<sup>2</sup>The AL result is taken from Herráez et al. (2017) instead of van Kuik et al. (2014) as it is much more accurate, e.g. 3 times more blade elements distributed along the radius.

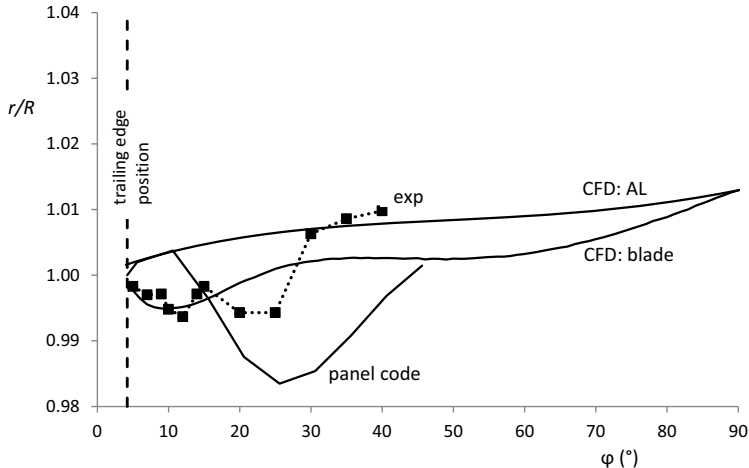


Figure 7.10: The radial coordinate of the tip vortex as a function of the azimuth angle measured from the  $c/4$  position.

property is that the conservative loads act on bound vorticity, which existence depends on the dimension of the lifting surface perpendicular to its main bound vorticity. For the wing and blade the main vorticity is the spanwise vorticity, which behaves as a Dirac delta function when the chord becomes 0 in case of lifting or actuator line modelling. For the actuator disc the main bound vorticity is the radial vorticity, with the axial vorticity vanishing for the thickness going to 0. This implies that conservative and non-conservative forces depend in essentially different ways on the geometry of the surface or volume carrying them. For analyses with non-conservative loads, no geometrical information is necessary once the circulation is defined. In contrast to this, conservative forces do depend on geometry since the disc thickness or blade chord have to be known. Since conservative forces do not convert power nor produce vorticity, they may be discarded from the force field that induces the flow, without violating conservation laws or far field boundary conditions. This was shown by the disc calculations without the radial force, and the actuator line calculations for the rotor. However, the resulting flow field differs from the 'original' flow field as shown in figure 7.2 for the disc and figure 7.10 for the blade tip.

The physical origin of the conservative force field is the same as of the non-conservative one: the pressure distribution. Realizing this, a different explanation of the dependency of the spanwise or radial load on the dimensions of the cross section is possible. Projection of the wing or blade surface in spanwise or radial direction gives the surface which is observed when looking from the wing - blade tip to the inboard direction. The pressure integrated on this surface gives the spanwise or radial load. For a vanishing chord length the projected surface disappears and so does the radial load. For the conservative additional lift at the tip a similar reasoning is possible: when the chord tends to 0 the spanwise bound vorticity as well as the chordwise vorticity become concentrated in a discrete vortex,

but, unlike the spanwise vortex, the tip vortex has no length or surface to which it is bound.

## 7.5. Evaluation

In previous chapters the disc was assumed to have a zero thickness, and the rotor blade zero thickness and chord. This chapter deviates from this by analysing the flow induced by a force field acting on a thick disc, as well the flow around a rotor blade tip with a non-zero cross section. In both cases conservative forces appear in the equations of motion. These conservative forces become 0 for vanishing dimensions in contrast to the non-conservative forces. The role of the conservative forces is to maintain the local flow and pressure equilibrium at the volume where the non-conservative force density is distributed. Apart from understanding the role of force fields, there is one result relevant for wind turbine rotor flows: the conservative tip load on the chordwise bound vorticity at the tip explains why some experiments show that the tip vortex moves inboard after being released, before wake expansion drives it outboard. Question Q13 listed in section 1.4 addressed this tip flow effect, which will be included in the discussion about tip corrections in the next chapter.

This page intentionally left blank

## From disc theory to BEM models: the tip correction

### 8.1. Introduction

In the previous chapters we have refreshed the one- and two-dimensional actuator disc theories and shown that these are a solid basis for rotor models. However, the step to convert actuator disc theory to rotor models has not yet been set. The textbook by [Sørensen \(2015\)](#) presents an excellent overview of momentum-based models and treats BEM with emphasis on the differences between some versions, the limitations and the add-on engineering rules that make BEM the most used rotor design method for wind turbines. Here we limit ourselves to the basic form of BEM, assuming the rotor to operate in undisturbed uniform parallel flow aligned with the rotor axis. The essential steps in the conversion from actuator disc theory to BEM have to do with:

- (i) the radial distribution of the induction: apply the disc momentum theory per annulus, including the contribution of the pressure at the boundary of the annulus, with an assumed load on the blade element replacing the disc load,
- (ii) the azimuthal distribution of the induction: account for the azimuthal non-uniformity in rotor flows in contrast to axi-symmetric disc flows,
- (iii) the radial distribution of the blade circulation: for an ideal Joukowsky rotor this circulation is constant, which is physically not possible,
- (iv) iterative optimisation: determine the lift and drag on the blade element by blade element theory, based on the previous steps, and optimise the performance by varying the blade geometry in an iterative procedure.

This chapter discusses step (i) to (iii), preceded by section 8.2 on the tip correction that is most used to account for (i) to (iii). In current BEM practice, the tip correction is the single measure to convert the disc flow to a rotor flow. This correction is based on a correction of Prandtl for (ii), but has a consequence for the radial distribution of the induction, (i), and thereby modifies the circulation, (iii). Despite these interactions (i)-(iii) are treated here separately to emphasise the differences in cause and effect.

### 8.2. Development of the tip correction

**8.2.1. In BEM methods.** The tip correction  $F$  used in most BEM models is based on the appendix by Prandtl added to the paper of [Betz \(1919\)](#), on the ideal circulation distribution for lightly loaded discs discussed in section 1.2.3 and shown in figure 1.1. Prandtl's appendix presents a correction  $F$  to Betz's model

to account for a finite number of blades, resulting in a correction of the induced velocity at the rotor plane. The correction is derived as a two-dimensional solution where Betz's model is three-dimensional. As this correction is most noticeable near the tip it is commonly called a tip correction although no details of the tip geometry are included. Prandtl himself and [Glauert \(1935, ch. VII-4\)](#) name it a correction for the effect of number of blades and do not use the words 'tip correction'. After Prandtl the correction has been modified by many, as can be read in [Sørensen \(2015, chapter 8\)](#) and [Branlard \(2017, chapter 13\)](#). [Glauert \(1935, ch. VII-4\)](#) has adapted Prandtl's model, by which it corrects the induction at the blade position instead of the azimuthally averaged induction. Thereafter many have fine tuned the Prandtl-Glauert correction by adding tip geometry input and by validation with experiments and CFD calculations. In particular this is done by wind energy researchers like [Shen et al. \(2005a\)](#), [Branlard et al. \(2013\)](#), [Shen et al. \(2014\)](#), [Schmitz and Maniaci \(2016\)](#), [Maniaci and Schmitz \(2016\)](#), [Sørensen et al. \(2016\)](#), [Wimhurst and Wilden \(2017\)](#) and [El khchine and Sriti \(2017\)](#). The contribution by [Shen et al. \(2005a\)](#) adds a correction  $F_1$  to achieve 3-D tip-aerofoil properties in combination with the Prandtl-Glauert correction for the induction at the blade position.  $F$  and  $F_1$  and their role in the momentum balance will be treated in section [8.3](#).

[Wood et al. \(2016\)](#) and [Wood \(2018\)](#) treat the Prandtl correction for rotors having a circulation distribution for which the correction was developed: the Betz-Goldstein distribution mentioned in section [1.2.3](#). For the Joukowsky distribution the physical meaning of the correction is not that clear any more: originally Prandtl derived it as a 2-D correction for the 3-D optimal Betz circulation distribution for lightly loaded discs, but it is applied to BEM which optimises for a heavily loaded Joukowsky distribution. Furthermore, many of the adaptations and additions do not have a basis in the circulation model of Betz and Prandtl, but in validations by experiments and CFD results. The result is an efficient engineering model to obtain the induced velocity at the blade position, 3-D tip-aerofoil properties and, in an iterative process, the load at the outer part of the blade.

**8.2.2. In actuator disc, actuator line and lifting line methods.** [Shen et al. \(2005b\)](#) have developed a tip correction method to be used for actuator disc and actuator line analyses analogous to the method in [Shen et al. \(2005a\)](#). The same equations for  $F$  and  $F_1$  are used as for BEM, but the application is different. As actuator disc flows are obtained by CFD or vorticity based flow solvers, the relation between loads and flow field is exact, apart from numerical discretisation issues, so there is no need for a tip correction  $F$ . The same holds for  $F_1$ , correcting 2-D aerofoil properties to 3-D, when the disc load is prescribed as in the analyses in chapter [5](#) and [6](#). If the actuator disc is to represent real blade loads instead of an axisymmetric disc load, correction  $F$  in combination with  $F_1$  is recommended. For actuator line and lifting line analyses the same reasoning applies:  $F$  is not required to obtain the correct flow field, and  $F_1$  is not necessary when the line load or circulation is prescribed, as for the flow cases shown in figure [2.4](#). In case the load at the actuator or lifting line is obtained in an iterative procedure with a blade element analysis, correction  $F_1$  is required.

### 8.3. The distribution of the axial velocity

**8.3.1. The radial distribution.** At the time Prandtl derived his correction the velocity distribution at the Froude or Joukowsky disc was not yet known. In chapter 5 this distribution has been calculated for a range of thrust coefficients for Froude discs representing wind turbines, so it is worthwhile to compare this with the results of BEM with a tip correction. The tip correction used is the one of Shen et al. (2005a, 2014). In this model the Prandtl-Glauert correction  $F$ , correcting the azimuthally averaged induction to the induction at the blade position, is extended by a correction  $F_1$  to modify 2-D aerofoil properties to 3-D properties, originating from the tip flow. The equation for  $F$  is:

$$F = \frac{2}{\pi} \cos^{-1} \left[ \exp \left( -\frac{B}{2} \left( \frac{R}{r} - 1 \right) \frac{1}{\sin(\theta)} \right) \right], \quad (8.1)$$

where  $\theta$  is the local inflow angle, with  $\sin(\theta) = v_{x,B} / \sqrt{(\Omega r - v_{\varphi,B})^2 + v_{x,B}^2}$ . To account for local tip shape properties, some details of the tip geometry are included in this correction  $F_1$ :

$$\left. \begin{aligned} F_1 &= \frac{2}{\pi} \cos^{-1} \left[ \exp \left( -g \frac{B}{2} \left( \frac{R}{r} - 1 \right)^n \frac{1}{\sin(\theta)} \right) \right] \\ g &= \exp \left[ \frac{0.125(B\lambda - 21)}{1 - 2k} \right] + 0.1 \\ n &= 1 + 0.5k \end{aligned} \right\} \quad (8.2)$$

where  $k$  is the minimum value of chord-to-radius derivative at the tip. The value  $k = -0.45$ , used by Shen, is kept unchanged. When  $B$ ,  $\lambda$  are given,  $F$  and  $F_1$  are known except for  $v_{x,B}$  or the induction  $a_B = (1 - v_{x,B}/U_0)$ . For  $n = 1$  and  $g = 1$ ,  $F_1$  is identical to  $F$ , the Prandtl-Glauert correction.  $F_1$  is the correction of the blade loads by Shen et al., so the combination of  $F_1$  and  $F$  is called the Prandtl-Glauert-Shen (PGS) correction. In BEM this is used in the momentum balance to solve  $a_B$ :

$$C_t F_1 = 4a_B F (1 - a_B F), \quad (8.3)$$

with the local thrust coefficient  $C_t$  originating from blade element theory based on 2-D aerofoil properties. For a given  $C_t F_1$ , the quantity  $a_B F$  is solved as the azimuthally averaged induction resulting from the momentum theory without any radial dependency of the results. The local induction  $a_B$  follows after division by  $F$ .

For the actuator disc  $C_t$  is given by (4.26). Here we use it without the  $q^2$  term, as discussed in section 4.2.3, while  $C_t$  is treated as if it is based on aerofoil properties. The momentum theory solution of (8.3) will be compared with the calculated actuator disc results obtained in chapter 5, for the same uncorrected  $C_t$ .

For wind turbine discs the radial distribution of the axial velocity is given by the function  $G$ , described by (5.23) and (5.24), and shown in figure 5.14. It is used in combination with the local momentum equation:

$$\left. \begin{aligned} C_t &= 4a(1 - a) \\ 1 - a_B &= G(1 - a) \end{aligned} \right\} \quad (8.4)$$

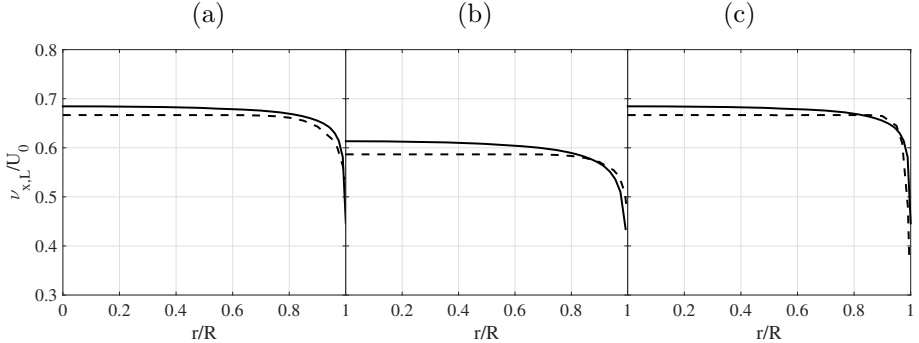


Figure 8.1: The axial velocity distribution obtained from the momentum theory + PGS correction (dash line) and actuator disc function  $G$  (solid line). (a) to (c) correspond with the flow cases in table 8.1

The first equation gives the induction  $a$  as if the local and disc-averaged momentum equations are the same, the second equation gives the local value. The comparison of both methods, (8.3) and (8.4), is done for the load cases given in table 8.1, representing an optimal rotor (a), a heavily loaded rotor (b) and a very fast running rotor (c). The results are shown in figure 8.1, presenting  $v_{x,B}$  as resulting from the PGS correction and  $G$  function. The PGS correction has little effect for  $r < 0.8R$  so the the axial velocity is lower than the  $G$ -function for  $r/R < 0.8$ . For  $r/R > 0.8$  the actuator disc line  $G$  corresponds reasonably well with the PGS corrected results.

**8.3.2. The azimuthal distribution: averaged or at blade position.** Actuator Line and Lifting Line models have been introduced in section 2.3: both have a constant circulation and do not apply any correction. For rotors modelled as an AL or LL operating in a uniform flow aligned with the rotor axis, the induction at the position of the AL/LL by the bound vorticity of the other AL/LL is zero. The same holds for the azimuthally averaged induction by the AL/LL, as follows by considerations of anti-symmetry based on the Biot-Savart rules. It is only wake vorticity that defines the induction at the AL/LL and the azimuthally averaged induction, irrespective of the radial distribution of the bound  $\Gamma$ . When the blade is modelled with a non-zero chord length, the anti-symmetry is distorted so the induction may be different. In sections 8.3.3 and 8.4.2 the effect of non-zero chord will be discussed.

Table 8.1: Flow cases

Case #	$\lambda$	$C_T$
(a)	7	0.888
(b)	7	0.970
(c)	20	0.888

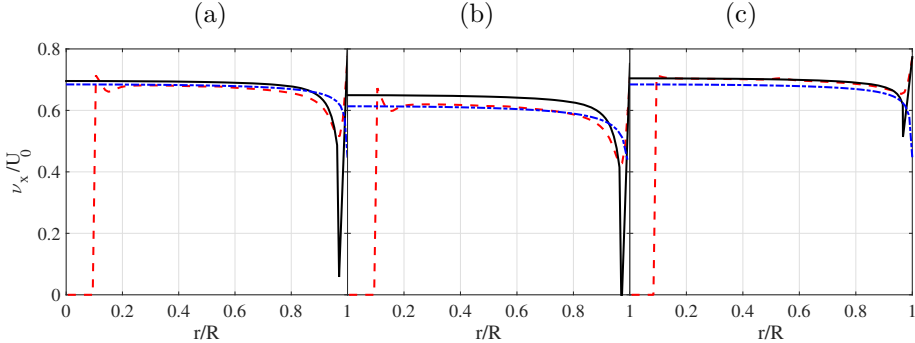


Figure 8.2: The axial velocity distribution at the actuator line (red dashed line), the lifting line (black solid line) and the actuator disc (blue dashed-dot line) for cases (a), (b) and (c) defined in table 8.1

Here we compare the velocity distribution at the disc as calculated in chapter 5 with the velocity at the position of a 3-bladed rotor modelled as an AL or LL generating the same thrust. The load cases used in this comparison are given in table 8.1, with the axial velocity distribution for case (a) shown in figure 2.4.

As shown in figure 3.2-a the vortex emanating from the tip of a rotor blade has a small axial and a large azimuthal component when  $\lambda$  is sufficiently high. Then the induction by wake vorticity at the rotor plane will show little non-uniformity in azimuthal direction, apart from the induction at the outer part of the AL/LL by the very first part of the tip vortex. This is confirmed by the AL/LL calculations for the three load cases. In figure 8.2 the distribution of the axial velocity of the actuator disc as given by (5.23) is compared with the distribution calculated by the AL and LL models at the blade position. As the AL model does not give results close to the rotor axis, see figure 2.4, the graphs show a jump to 0 for  $r/R < 0.1$ . The numerical discretisation of both models and the consequences for the accuracy are described in van Kuik et al. (2015b), but some aspects are treated here. The minimum value for  $v_x$  should be at  $r/R = 1$  for an infinitely thin vortex core, but occurs at a lower radius for both models. This is a consequence of the vortex core size, as is confirmed by figure 9 of Segalini and Alfredsson (2013) showing the same behaviour and explanation. Furthermore the discretisation parameters have not been optimised per load case, given computational limitations. For  $r/R < 0.8$  the AL, LL and disc results agree reasonably in cases (a), show a deviation of the LL model in the heavily loaded case (b) and of the disc results in the high  $\lambda$  case (c). With respect to the shape of the distribution for  $r/R > 0.8$  the AL and LL models agree well but show a steeper curve than the disc distribution, so  $v_{x,B} \text{ AL/LL} < v_{x,disc}$ , except for case (c). Case (a) is treated too in Segalini and Alfredsson (2013). Figure 9 of this paper compares the induction at the lifting line,  $a_B$ , with the azimuthally averaged induction  $\bar{a}$ , showing that  $a_B/\bar{a} > 1$  so  $v_{x,B} < \bar{v}_x$ , especially near the tip. This is the effect of the nearby position of the first part of the tip vortex, responsible for the azimuthal non-uniformity in wake-induced  $v_x$ . As in the high  $\lambda$  case (c) the tip vortices are less strong compared to

the strength in (a) with equal thrust, the non-uniformity in (c) is less compared to (a) by which the distributions match better.

Figure 8.2 shows that in case the disc distribution  $G$  is used as basis for the momentum balance in BEM, the required correction from  $\bar{a}(r)$  to  $a_B(r)$  is much smaller than from the uniform induction  $a$  used in BEM, to the PGS corrected  $a_B(r)$ .

**8.3.3. The azimuthal distribution: decambering of aerofoils.** In BEM the blades are not modelled as a line, but have a non-zero chord. The anti-symmetry considerations mentioned in the previous section are not exact any more. The Blade-Element part in BEM relies on two-dimensional aerofoil data to determine the lift and drag once the local velocity vector is known. This data assume that the induction is uniform along the chord. This is not the case as can be observed in figure 2.4: the axial velocity at both sides of the AL-LL is not the same. In front of the AL-LL (in anti-clockwise direction)  $v_x$  is larger than at positions after the line. For a rotor with a non-zero chord, this implies that at the leading edge of the aerofoil  $v_x$  is higher than at the aerodynamic centre,  $c/4$ . At the trailing edge  $v_x$  is lower than at the aerodynamic centre. Expressed in the axial induction this implies that  $v_{x,induced}$  increases from leading to trailing edge, corresponding to figure 1 in Sørensen et al. (2015), who introduced the decamber correction to account for the non-uniform induction. As shown in this paper, the non-uniform induction has the same effect as a negative camber added to the aerofoil: it decreases the lift by increasing the zero-lift angle of attack.

Although the decambering occurs along the entire blade span, the correction proposed by Sørensen et al. (2015) is called a refined tip correction as it is most noticeable at the tip. It is a correction of the zero-lift angle  $\Delta\alpha_{C_l=0}$ , obtained by an iterative calculation of the induced velocity at several chordwise positions. In each iteration  $\Delta\alpha_{C_l=0}$  leads to a change in the circulation  $\Gamma$  of the blade, so to a change in induction. For a given rotor geometry the correction can be calculated for various flow angles. During performance computations the actual correction can be obtained by interpolation .

Sørensen et al. (2015) use their correction together with the Prandtl-Glauert tip correction (8.1). Comparison of lifting line and BEM results, both with the decamber correction, show an improved agreement with results by a vortex lattice method, compared with uncorrected results. The vortex lattice method includes modelling of the blade surface as a (bound) vortex sheet. The change in circulation and loads for modern rotor blades is significant in the outer part of the blade where the thrust is lowered by 7 – 8%. The change in performance is small.

#### 8.4. The radial distribution of $\Gamma_{blade}$

For Joukowsky discs and rotors the bound circulation  $\Gamma$  is taken to be constant, but this is physically not possible. The circulation of a lifting surface will gradually go to 0 when  $r \rightarrow 0$ . For the TUD-B rotor analysed in the previous chapter this occurs for  $r/R > 0.85$ , see figure 7.8. This figure shows a second aspect of the tip flow: the creation of the tip vortex for  $r/R > 0.95$ . This involves strong three-dimensional aerodynamics, in contrast to the aerodynamics of blade sections at some distance from the root and tip, for which two-dimensional or

blade element aerodynamics is sufficient. In classical wing theory both effects are modelled as a function of the aspect ratio  $\mathcal{A} = b/c$  where  $b$  is the span and  $c$  the maximum chord. The usefulness of this method is discussed in the next section, whereas the role of chordwise bound vorticity is treated in section 8.4.2.

**8.4.1. The aspect ratio as a measure for tip effects.** The tip or root are the positions where the bound vorticity changes direction from spanwise to chordwise and releases a free vortex into the flow, as shown in figures 7.4 and 7.8. For straight rectangular wings the tip effect or effective angle of attack is expressed in the aspect ratio  $\mathcal{A}$ :  $\alpha_{\mathcal{A}} = C_L/(\pi \mathcal{A}_{eff})$ . Glauert (1935, ch. VI-7) discusses such an effective aspect ratio to be used in propeller design. However, as noted by Corten (2001a) this  $\alpha_{\mathcal{A}}$  is the change of  $\alpha$  due to the induction by the tip vortices, which is already taken into account in the momentum balance. Not captured by the momentum balance is the following tip effect. For large  $\mathcal{A}$  the lift of a wing is linear in  $\alpha$  but for  $\mathcal{A} \rightarrow 0$  the lift becomes quadratic in  $\alpha$ , see e.g. Rathakrishnan (2013, section 8.3). The reason is that the tip vortices, emerging at the suction side of the surface, give additional lift due to their low pressure, see e.g. figure 4.34 in Küchemann (1978). For rotor blades the same physical phenomena occur, see e.g. Gray et al. (1980) who show the measured pressure distribution at the tip of a model rotor operating in hover, resulting in a significant increase of the normal force for  $r/R > 0.98$ . van Kuik et al. (2014, figure 8) show the same behaviour for the TU-B rotor analysed in chapter 7. This phenomenon comes back in the next section.

Although the aspect ratio is an elegant parameter to model the finiteness of the span of a lifting surface, it does not model the physical origin of tip effects but rather the effects of it. Expressed in terms of pressure, the origin is in the equalisation of the over-pressure at one side of the surface to the under-pressure at the other side, called suction-side. The equalisation is achieved by flow passing along the tip from pressure to suction side. Wimshurst and Wilden (2018) use this pressure approach to study the behaviour of the tip flow. Expressed in vorticity terms, the origin is in the change of bound spanwise vorticity to free tip vorticity. In section 7.3 this transition has been analysed, with emphasis on the bound chordwise vorticity and the load it carries. In the next section we will discuss in more detail how to model this.

**8.4.2. Chordwise vorticity and conservative loads at the tip.** In chapter 7 the conservative load on bound chordwise vorticity at the tip of a wind turbine blade has been analysed. A comparison of a body-fitted CFD solution, with chordwise information, with an actuator line solution, without chordwise information, showed that the AL method<sup>1</sup> cannot reproduce the inboard motion of a tip vortex whereas the body-fitted CFD method does so. In Herráez et al. (2017) the AL method is extended to account for bound chordwise vorticity by artificially introducing conservative tip loads. These loads are determined as Kutta-Joukowsky loads on bound chordwise vorticity  $-\rho \mathbf{v} \times \boldsymbol{\Gamma}_{chord}$  where  $\boldsymbol{\Gamma}_{chord}$  is assumed to be  $\zeta \boldsymbol{\Gamma}_{max,spanwise}$  with  $\zeta$  an engineering number  $0 < \zeta < 1$ . Tentatively  $\zeta = 0.75$ .

---

<sup>1</sup>The AL method used for figures 7.10 and 8.3 differs from the AL method of figure 8.2 where  $\boldsymbol{\Gamma}$  is constant, without any correction. Now the load distribution is based on the TUD-B rotor geometry, with Shen's correction  $F_1$  but without the Prandtl-Glauert function  $F$ .

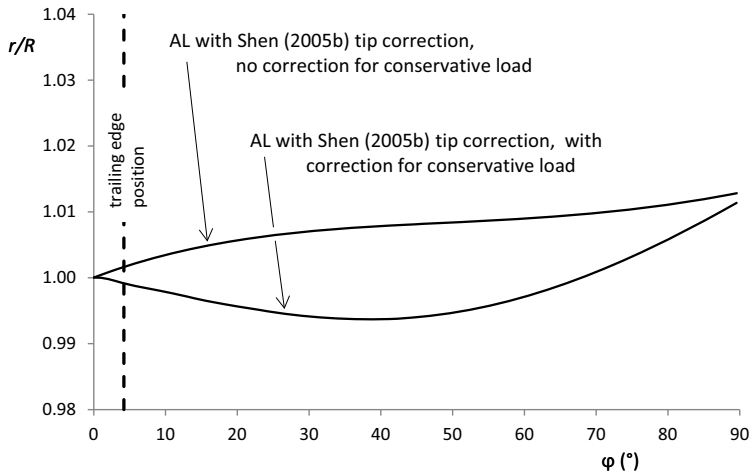


Figure 8.3: The radial coordinate of the tip vortex of the TU-D B rotor as determined by full CFD and AL solutions.

is chosen, corresponding to the circulation leaving the blade between  $r/R = 0.98$  and 1.0 as shown in figure 7.8. The result is shown in figure 8.3 which makes clear that a conventional AL cannot capture the inboard motion of the tip vortex as shown in figure 7.10. The forces acting on the chordwise vorticity, with  $\zeta = 0.75$ , have the same order of magnitude as in table 7.1: 1% of the blade thrust. Therefore the importance of this correction is not in the determination of loads and power, but in the precise location of the tip vortices required for an optimisation of the tip geometry. As shown in Herráez et al. (2017) the correction for the tip loads leads to a modest change in the induced velocity, angle of attack and loads for  $0.9 < r/R < 1$ .

## 8.5. Evaluation

The last question, Q14, listed in section 1.4, addresses the tip correction. Chapter 8 has analysed several tip flow properties, leaving ample room for discussion and future work. The results of the AL/LL calculations have to be considered as preliminary, awaiting studies with more flow cases and a higher accuracy. Still, some conclusions can already be drawn:

- The wind turbine disc distribution  $G$  of  $v_{x,d}$ , see (5.24), and the PGS distribution (8.2, 8.3) match reasonably well close to the edge. This may be considered as a mutual confirmation.
- The axial velocity at the position of the blade close to the tip is lower than the azimuthally averaged value, which is to be expected due to the induction by the first part of the tip vortex causing the azimuthal non-uniformity in wake-induced  $v_{x,d}$
- The mutual relation between induction and load at the tip is not easy to capture in a single correction. The PGS correction does not include the decamber

correction nor the correction for the presence of chordwise vorticity at the tip. Both effects have a limited effect on the overall load and performance but are relevant for a detailed, optimised tip design.

Further research and discussion is required about the following:

- The PGS distribution is well-tuned by many researchers but its physical basis does not match the optimisation of rotors according to a Joukowsky distribution. Now this basis, being the distribution  $G$  for the Joukowsky disc, is known, this could replace the PGS distribution
- In case the disc distribution  $G$  is used as basis for the momentum balance in BEM, the correction from  $\bar{a}(r)$  to  $a_B(r)$  is much smaller than from the uniform induction  $a$  used in BEM to the PGS corrected  $a_B$ . The use of  $G$  could lead to a more accurate assessment of  $a_B$
- It is not yet clear whether the PGS correction and the correction for the chordwise bound vorticity can be used together, as both corrections have a different background.

These topics for discussion are left for future research. Validation by experiments and full CFD solutions will provide insight whether there is room for improvement compared the current practice of using BEM with the PGS correction.

This page intentionally left blank

## Epilogue

The evaluation of the results per chapter is presented in the last section of each chapter, and not included here in detail. This Epilogue takes some distance and looks back at the main results.

With the force field term retained in the Euler equation of motion, the relations between a force field and the conversion of energy can be interpreted in the conceptual framework of solid mechanics: conservative force exchange potential and kinetic energy but do not perform work. Non-conservative forces do so, and change the Bernoulli parameter  $H$ . Moreover, non-conservative forces generate vorticity, conservative forces conserve vorticity. As, from a fluid dynamic point of view, these processes are governing rotor flows, the force field method is shown to be very helpful in the evaluation and understanding of actuator disc and rotor flows. A new actuator disc equation has been derived, see (4.7), valid for any distribution of  $\mathbf{f}$ . Thanks to the similarity with the Kutta-Joukowsky expression for the load on a vortex, the physically plausible result that the actuator disc is a rotor subjected to the limit of an infinite number of blades, is confirmed by analytical limit transitions.

The momentum theory of Froude and Joukowsky actuator discs has been formulated in terms conservative and non-conservative force fields. The non-uniformity of the axial velocity at the disc is shown to be the consequence of the pressure field, acting as a conservative load. The same holds for the difference between the Joukowsky disc performance and the Froude disc performance: in Joukowsky disc flows, part of the swirl induced pressure field appears as a conservative contribution to the momentum balance, so is absent in the energy balance leading to deviations from Froude discs. A remarkable result is that at the disc, the velocity in the meridian plane is constant for wind turbine discs, with or without swirl. For propeller discs this velocity is non-uniform.

Conservative loads appear when the load carrying surfaces like a disc, rotor blade or wing, are modelled with real, non-zero dimensions. The origin is found in the distribution of bound vorticity: when bound vorticity lines are non-parallel, e.g. at the tip of a rotor blade, the mutual induction gives rise to these conservative forces. With this phenomenon, the initially inboard motion of a tip vortex of wind turbine rotor blades could be explained.

Much more detailed information about disc and rotor flows is available, compared with the first decades of the previous century. This makes it worthwhile to reconsider the assumptions and engineering models with which disc results have been made amenable for rotor modelling. A first attempt to use the obtained disc velocity distribution has been presented, and compared with the current practice

of using the disc averaged velocity with a tip correction. Although the correspondence is reasonably good, much more validation and tuning is required to give this method a firm basis. The same holds for adding the conservative tip load in actuator line modelling: the presented first attempt reproduces the inboard motion of the tip vortex, but more testing on more load cases is required.

## APPENDIX A

### Vector expressions in cylindrical coordinates

$$\nabla v = \mathbf{e}_x \frac{\partial v}{\partial x} + \mathbf{e}_r \frac{\partial v}{\partial r} + \mathbf{e}_\varphi \frac{1}{r} \frac{\partial v}{\partial \varphi} \quad (\text{A.1})$$

$$\nabla^2 v = \frac{\partial^2 v}{\partial x^2} + \frac{1}{r} \frac{\partial}{\partial r} \left( r \frac{\partial v}{\partial r} \right) + \frac{1}{r^2} \frac{\partial^2 v}{\partial \varphi^2} \quad (\text{A.2})$$

$$\nabla \cdot \mathbf{v} = \frac{\partial v_x}{\partial x} + \frac{1}{r} \frac{\partial v_r}{\partial r} + \frac{1}{r} \frac{\partial v_\varphi}{\partial \varphi} \quad (\text{A.3})$$

$$(\mathbf{v} \cdot \nabla) \mathbf{v} = \mathbf{e}_x (\mathbf{v} \cdot \nabla v_x) + \mathbf{e}_r \left( \mathbf{v} \cdot \nabla v_r - \frac{v_\varphi^2}{r} \right) + \mathbf{e}_\varphi \left( \mathbf{v} \cdot \nabla v_\varphi + \frac{v_\varphi v_r}{r} \right) \quad (\text{A.4})$$

$$\mathbf{v} \cdot \nabla v = v_x \frac{\partial v}{\partial x} + v_r \frac{\partial v}{\partial r} + v_\varphi \frac{1}{r} \frac{\partial v}{\partial \varphi} \quad (\text{A.5})$$

$$(\mathbf{v} \cdot \nabla) \boldsymbol{\omega} = \mathbf{e}_x (\mathbf{v} \cdot \nabla \omega_x) + \mathbf{e}_r \left( \mathbf{v} \cdot \nabla \omega_r - \frac{v_\varphi \omega_\varphi}{r} \right) + \mathbf{e}_\varphi \left( \mathbf{v} \cdot \nabla \omega_\varphi + \frac{v_\varphi \omega_r}{r} \right) \quad (\text{A.6})$$

$$(\boldsymbol{\omega} \cdot \nabla) \mathbf{v} = \mathbf{e}_x (\boldsymbol{\omega} \cdot \nabla v_x) + \mathbf{e}_r \left( \boldsymbol{\omega} \cdot \nabla v_r - \frac{v_\varphi \omega_\varphi}{r} \right) + \mathbf{e}_\varphi \left( \boldsymbol{\omega} \cdot \nabla v_\varphi + \frac{v_r \omega_\varphi}{r} \right) \quad (\text{A.7})$$

$$\boldsymbol{\omega} = \mathbf{e}_x \left( \frac{1}{r} \frac{\partial (rv_\varphi)}{\partial r} - \frac{1}{r} \frac{\partial v_r}{\partial \varphi} \right) + \mathbf{e}_r \left( \frac{1}{r} \frac{\partial v_x}{\partial \varphi} - \frac{\partial v_\varphi}{\partial x} \right) + \mathbf{e}_\varphi \left( \frac{\partial v_r}{\partial x} - \frac{\partial v_x}{\partial r} \right) \quad (\text{A.8})$$

$$\mathbf{v} \times \boldsymbol{\omega} = \mathbf{e}_x (v_r \omega_\varphi - v_\varphi \omega_r) + \mathbf{e}_r (v_\varphi \omega_x - v_x \omega_\varphi) + \mathbf{e}_\varphi (v_x \omega_r - v_r \omega_x) \quad (\text{A.9})$$

$$\frac{1}{\rho} (\mathbf{f} - \nabla p) = \frac{\partial \mathbf{v}}{\partial t} + \mathbf{e}_x \mathbf{v} \cdot \nabla v_x + \mathbf{e}_r \left( \mathbf{v} \cdot \nabla v_r - \frac{v_\varphi^2}{r} \right) + \mathbf{e}_\varphi \left( \mathbf{v} \cdot \nabla v_\varphi + \frac{v_\varphi v_r}{r} \right) \quad (\text{A.10})$$

This page intentionally left blank

## APPENDIX B

### Balance of angular momentum

This appendix is restricted to steady 3-D axisymmetric flows without swirl and steady 2-D flows. The curl of the Euler equation (2.3) gives

$$\frac{1}{\rho} \nabla \times \mathbf{f} = -\nabla \times (\mathbf{v} \times \boldsymbol{\omega}). \quad (\text{B.1})$$

In the meridian plane a circle  $C$  is defined with polar coordinates  $(\xi, \theta)$ , enclosing area  $A$ . Integration of (B.1) on  $A$  shows, using Stokes' theorem:

$$\frac{1}{\rho} \oint_C \mathbf{f} \cdot d\mathbf{c} = - \oint_C (\mathbf{v} \times \boldsymbol{\omega}) \cdot d\mathbf{c} = \oint_C v_\xi \omega_\varphi \xi d\theta, \quad (\text{B.2})$$

where  $d\mathbf{c}$  is tangent to  $C$ . Using  $\omega_\varphi = \partial(\xi v_\theta) / (\xi \partial \xi) - \partial v_\xi / (\xi \partial \theta)$  and  $\oint v_\xi \partial v_\xi = 0$ , (B.2) becomes:

$$\begin{aligned} \frac{1}{\rho} \oint_C \mathbf{f} \cdot d\mathbf{c} &= \oint_C v_\xi \frac{\partial(\xi v_\theta)}{\partial \xi} d\theta \\ &= \oint_C \left( \frac{\partial(\xi v_\theta v_\xi)}{\xi \partial \xi} - v_\theta \frac{\partial v_\xi}{\partial \xi} \right) \xi d\theta. \end{aligned} \quad (\text{B.3})$$

Multiplication of (B.3) by  $\xi^*$  and integration for  $0 \leq \xi^* \leq \xi$  gives the torque  $Q(\xi)$  about the centre of  $C$  exerted by the force field  $\mathbf{f}$  within  $C$ :

$$\begin{aligned} \frac{1}{\rho} Q &= \frac{1}{\rho} \int_0^\xi \xi^* \oint_C \mathbf{f} \cdot d\mathbf{c} d\xi^* \\ &= \int_0^\xi \oint_C (d(\xi^* v_\theta v_\xi) - v_\theta \xi^* dv_\xi) \xi^* d\theta \\ &= \int_0^\xi \oint_C d(\xi^{*2} v_\theta v_\xi) d\theta - \int_0^\xi \oint_C \xi^* v_\theta d(v_\xi \xi^*) d\theta. \end{aligned} \quad (\text{B.4})$$

The second integral is evaluated with the continuity equation (2.2) expressed in the  $(\xi, \theta)$  coordinate system:

$$\begin{aligned} \frac{\partial v_x}{\partial x} + \frac{\partial(rv_r)}{r \partial r} &= \frac{\partial v_x}{\partial x} + \frac{\partial v_r}{\partial r} + \frac{v_r}{r} \\ &= \frac{\partial(\xi v_\xi)}{\xi^* \partial \xi^*} + \frac{\partial v_\theta}{\xi^* \partial \theta} + \frac{v_r}{r} = 0, \end{aligned} \quad (\text{B.5})$$

by which:

$$\begin{aligned} \int_0^\xi \oint_C \xi^* v_\theta d(v_\xi \xi^*) d\theta &= - \int_0^\xi \oint_C \xi^* v_\theta dv_\theta d\xi^* - \int_0^\xi \oint_C v_\theta \frac{v_r}{r} \xi^{*2} d\xi^* d\theta \\ &= - \int_0^\xi \oint_C v_\theta \frac{v_r}{r} \xi^{*2} d\xi^* d\theta, \end{aligned} \quad (\text{B.6})$$

so  $Q$  is:

$$\begin{aligned} \frac{1}{\rho} Q &= \int_0^\xi \oint_C d(\xi^{*2} v_\theta v_\xi) d\theta + \int_0^\xi \oint_C v_\theta \frac{v_r}{r} \xi^{*2} d\xi^* d\theta \\ &= \oint_C \xi v_\theta v_\xi dC + \iint_A \xi^* v_\theta \frac{v_r}{r} dA. \end{aligned} \quad (\text{B.7})$$

This is the balance of angular momentum with control surface  $C$ . The first term at the right hand side gives the 2-D balance in which the torque equals the increase of angular momentum, being the mass transport  $\rho v_\xi$  having an angular momentum  $\xi v_\theta$  integrated along the contour  $C$ . The second term gives the change of angular momentum  $\xi^* v_\theta$  as a consequence of the vorticity stretching, see the last term at the right hand side of (3.16).

This shows that (B.1) indeed is the balance of angular momentum in differential form.

## APPENDIX C

# The blade load expressed as pressure distribution

In (4.14)  $\mathbf{L}$  is expressed in kinematic terms. However, physically it is pressure at a surface that creates a resultant load, so (4.14) has to have an equivalent pressure formulation. Integrated along the span on a volume  $V$  enclosing the blade, this gives the resultant force  $\mathbf{R}$

$$\mathbf{R} = -\rho \int_V \mathbf{v}_{rot} \times \boldsymbol{\omega} dV = -\rho \int_V \mathbf{v}_{rot} \times \boldsymbol{\omega}_{rot} dV + 2\rho \int_V \mathbf{v}_{rot} \times \mathbf{e}_x \Omega dV \quad (\text{C.1})$$

The distribution of  $\boldsymbol{\omega}$  at  $V$  is equivalent to the concentration of  $\boldsymbol{\omega}$  in an infinitely thin vortex sheet  $\boldsymbol{\gamma} = \int \boldsymbol{\omega} dn$  at the surface  $A$  of  $V$ , with  $\mathbf{n}$  normal to  $A$  and  $\mathbf{v}_{rot} = 0$  inside  $V$ . Consequently, the last integral does not contribute to  $\mathbf{R}$ . Since  $\boldsymbol{\gamma} = \mathbf{e}_n \times (\mathbf{v}_{rot,inside} - \mathbf{v}_{rot,outside})$  and the velocity at the sheet  $\mathbf{v}_{rot} = \frac{1}{2}(\mathbf{v}_{rot,inside} + \mathbf{v}_{rot,outside})$  the first integral becomes

$$-\rho \int_V \mathbf{v}_{rot} \times \boldsymbol{\omega}_{rot} dV = -\frac{\rho}{2} \int_A \overline{\mathbf{v}_{rot}} \times \boldsymbol{\gamma} dA = -\frac{\rho}{2} \int_A \mathbf{e}_n |\mathbf{v}_{rot,outside}|^2 dA. \quad (\text{C.2})$$

$\mathbf{v}_{rot,outside}$  is determined at streamlines tangent to the blade surface / vortex sheet, where  $\boldsymbol{\omega} = 0$  and  $\mathbf{f} = 0$ . By combining  $\nabla H_{rot} = \nabla \left( H - \rho v_\varphi \Omega r + \frac{\rho}{2} (\Omega r)^2 \right)$  with (2.22) it follows that  $H_{rot,outside} = \frac{\rho}{2} (\Omega r)^2 + c$  where  $c$  is a constant, so  $\frac{\rho}{2} |\mathbf{v}_{rot,outside}|^2 = c - (p - p_0) + \frac{\rho}{2} (\Omega r)^2$ . The contribution of  $c + p_0 + \frac{\rho}{2} (\Omega r)^2$  vanishes in the closed contour integral. Herewith (C.1) becomes

$$\mathbf{R} = -\rho \int_V \mathbf{v}_{rot} \times \boldsymbol{\omega} dV = \int_A p \mathbf{e}_n dA \quad (\text{C.3})$$

The product  $\mathbf{e}_x \cdot \mathbf{e}_n dA$  is equal to  $dA_x$  where  $A_x$  is the projection of the blade surface in axial direction.  $\mathbf{R}$  can be decomposed in the axial, radial or span-wise and azimuthal components:

$$\mathbf{R} = \mathbf{e}_x \int_A p dA_x + \mathbf{e}_r \int_A p dA_r + \mathbf{e}_\varphi \int_A p dA_\varphi \quad (\text{C.4})$$

The axial and azimuthal components of  $\mathbf{R}$  contribute to the rotor thrust and torque. The radial component does not do so, and does not perform work, by which it is a conservative component of the blade load.

This page intentionally left blank

## APPENDIX D

# The potential flow model

### D.1. Components of the model

The numerical model of the actuator disc wake vortex sheet has 2 components:  
Axisymmetric vortex rings: From the disc position  $x = 0$  up to  $x = 30$  the sheet is discretised using  $N$  vortex rings  $\Gamma_i(x_i, r_i)$ . The distribution of rings is not equidistant: for  $i = 1 \dots N$  the axial position  $x_i = (1 - \cos(i\pi/(c_1 N)))^{c_2}$  where  $c_1$  and  $c_2$  are constants tuned to make a smooth transition to the second component. For the results shown here  $c_1 = 2.72$ ,  $c_2 = 0.7$ . The values for  $N$  are given in the main text.

The expressions for the flow field induced by a ring at position are given by [Yoon and Heister \(2004\)](#):

$$\left. \begin{aligned} v_x &= \frac{\Gamma_i}{4\pi} r_i \left[ \left( r_i + r \frac{A}{B} \right) I_2 - \frac{r}{B} I_1 \right] \\ v_r &= \frac{\Gamma_i}{4\pi} r_i \left( \frac{x - x_i}{B} \right) (I_1 - A I_2) \\ \Psi &= \frac{\Gamma_i}{2\pi} \sqrt{r r_i} \left[ \left( \frac{2}{k} - k \right) K(k) - \frac{2}{k} E(k) \right] \end{aligned} \right\} \begin{aligned} \text{with} \\ A &= (x - x_i)^2 + r^2 + r_i^2 & B &= -2r r_i \\ I_1 &= \frac{4}{\rho_2} K(k) & I_2 &= \frac{4}{\rho_2^3} \frac{E(k)}{1 - k} & k &= \sqrt{1 - \left( \frac{\rho_1}{\rho_2} \right)^2} \\ \rho_1 &= \sqrt{(x - x_i)^2 + (r - r_i)^2} \\ \rho_2 &= \sqrt{(x - x_i)^2 + (r + r_i)^2} \end{aligned} \quad \rho_1 \geq \delta. \quad (\text{D.1})$$

$K(k)$  and  $E(k)$  are the complete elliptic integrals of the 1<sup>st</sup> and 2<sup>nd</sup> kind. At the position of the ring  $\rho_1 = 0$ ,  $\rho_2 = 1$  so  $k = 1$ . For  $k \rightarrow 1$   $K(k) \propto \log(1 - k)$  while  $E(k) = 1$ . Evaluation of the expressions shows that close to the ring  $v_x$  is dominated by the  $1/\rho_1$  singularity in  $I_1$ , known from linear vortices, and a weaker logarithmic singularity in  $I_2$  caused by the curvature of the ring. To avoid infinite velocities, a vortex kernel with diameter  $\delta$  is introduced. For  $\rho_1 \leq \delta/2$  the

expressions given by [Marshall \(2001\)](#), p. 270-271) are used:

$$\left. \begin{aligned} v_x &= \frac{\Gamma_i}{4\pi r_i} \left[ (\log \left( \frac{16r_i}{\delta} \right) - \frac{1}{4}) \right] \\ v_r &= 0 \\ \Psi &= \frac{\Gamma_i}{2\pi} \left[ (\log \left( \frac{16r_i}{\delta} \right) - \frac{3}{2}) \right] \end{aligned} \right\} \rho_1 < \frac{\delta}{2}. \quad (\text{D.2})$$

The semi-infinite vortex tube: The far wake, starting at  $x = 30$ , is the semi-infinite cylindrical vortex tube with constant strength  $\gamma$  and radius  $R_{tube} = 1.0$ . The vortex tube strength is given by the velocity jump across the tube boundary in the far wake, e.g. for a thrust coefficient  $C_T = \Delta p / (\frac{1}{2}\rho U_0^2) = -8/9$  the velocity in the wake is  $v_x/U_0 = 1/3$  so  $\gamma_{wake}/U_0 = -2/3$ . Suppose the semi-infinite tube is closed at infinity by a tube end plate with equal strength of vorticity. This has no effect on the flow at finite distance from the opening. Then the tube surface is a 3-D vortex sheet of uniform vorticity strength, which is equivalent to a dipole distribution of uniform strength, see [Marshall \(2001\)](#), p. 204). Surfaces with uniform dipole strength are treated by potential theory, see [Courant and Hilbert \(1967\)](#), p. 232), showing that the potential is proportional to the solid angle at the position of evaluation subtended by the aperture of the surface. This is confirmed by an independent evaluation of the expression for the velocity field  $\mathbf{v}$  induced by a closed vortex line  $\Gamma$  as given by [Saffman \(1992\)](#):

$$\mathbf{v} = -\frac{\Gamma}{4\pi} \nabla \Theta \quad (\text{D.3})$$

in which  $\Theta$  is the solid angle, expressed in steradian, subtended by the closed vortex line at the position of evaluation of  $\mathbf{v}$ . For an axisymmetric tube extending from  $x = x_0$  to  $x = \infty$ , having radius  $R_{tube}$  and constant strength  $\gamma$ , this becomes:

$$\mathbf{v}(x, r) = -\frac{\gamma}{4\pi} \int_{x_0}^{\infty} \nabla \Theta(x_0, R_{tube}, \xi) d\xi \quad (\text{D.4})$$

or, omitting  $(x, r)$ ,  $(x_0, R_{tube})$ :

$$v_x = -\frac{\gamma}{4\pi} \int_{x_0}^{\infty} \frac{\partial \Theta(\xi)}{\partial x} d\xi = \frac{\gamma}{4\pi} (\Theta(x_0) - \Theta(\infty)). \quad (\text{D.5})$$

Since  $\Theta(\infty) = 0$  this becomes:

$$v_x = -\frac{\gamma}{4\pi} \Theta \quad (\text{D.6})$$

where  $\Theta$  is the angle subtended by the entrance of the vortex tube. [Paxton \(1959\)](#) gives the expressions for the solid angle subtended by a ring, expressed in complete elliptic integrals. If the opening of the tube is denoted by  $x = x_0$ ,  $r = r_0$ , this becomes:

$$\Theta = \left( \frac{r_0 - r}{|r_0 - r|} + 1 \right) \pi + 2 \frac{(x - x_0)}{\rho_2} \left( K(k) - \frac{r - r_0}{r + r_0} \Pi(\alpha, k) \right), \quad \alpha = 2 \frac{\sqrt{rr_0}}{r + r_0} \quad (\text{D.7})$$

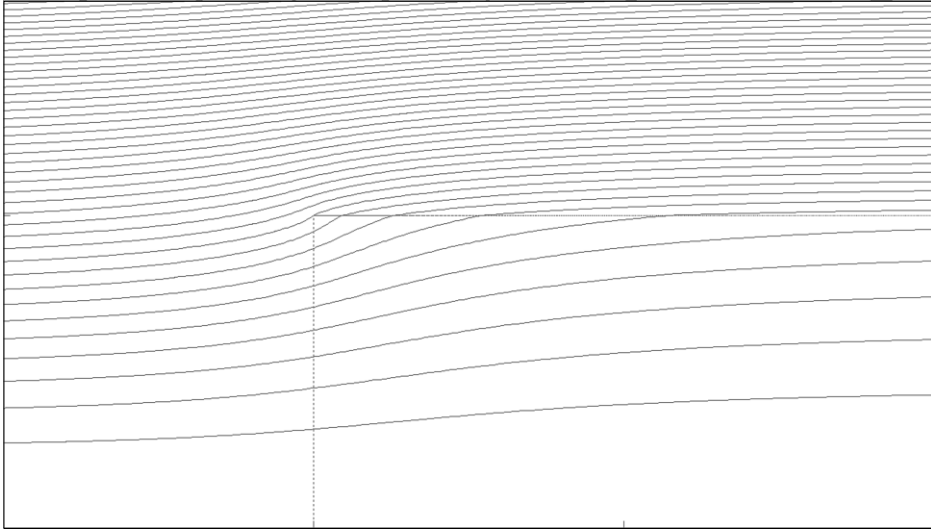


Figure D.1: Streamlines for a semi-infinite vortex tube in parallel flow

where now  $\rho_2 = \sqrt{(x - x_0)^2 + (r + r_0)^2}$  and  $\Pi(\alpha, k)$  is the complete elliptic integral of the 3<sup>rd</sup> kind.

[Branlard and Gaunaa \(2015\)](#) have published a different derivation of the same expression for the axial velocity, and present the expression for the radial velocity:

$$v_r = -\frac{\gamma}{2\pi} \sqrt{\frac{r_0}{r}} \left( \left( \frac{2}{k} - k \right) K(k) - \frac{2}{k} E(k) \right). \quad (\text{D.8})$$

As this equation was not yet known at the time of making the code, the continuity equation was used to numerically determine  $v_r$ . This was compared with (D.8) for verification, showing accurate correspondence, see section [D.3](#).

At  $r = 0$  (D.6) plus (D.7) yield a simple expression at the centerline, first published by [Snel and Schepers \(1995\)](#):

$$v_{x,r=0} = \frac{\gamma}{2} \left( 1 + \frac{(x - x_0)}{\sqrt{(x - x_0)^2 + R_{\text{tube}}^2}} \right). \quad (\text{D.9})$$

## D.2. Convergence scheme

The calculation starts with the configuration presented in the previous section: all vortex rings have the diameter and strength per unit length of the far wake tube, so  $\Gamma_i = \gamma_{\text{wake}}(x_i - x_{i-1})$  with  $r_i = R_{\text{wake}}$ . In each convergence step  $j$  the discretised part is adapted, so the shape and strength of the wake  $x_i < 30R_{\text{wake}}$  changes per step while the far wake vortex sheet radius and strength remain the same, as shown in figure [5.3](#). This implies that the disc radius, equal to the radius of the first vortex ring, is a variable, but that the axial position is invariant.

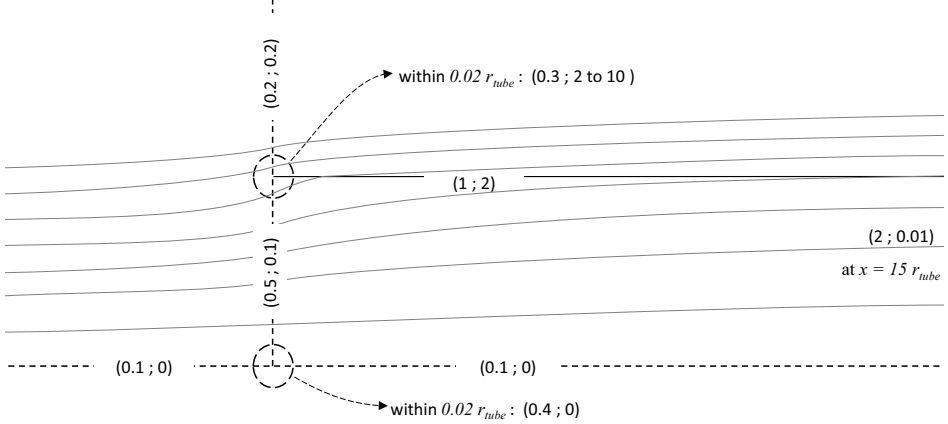


Figure D.2: Deviation of the calculated ( $v_x$  ;  $v_r$ ) with the analytical solutions (D.6) to (D.9), expressed in %, for  $N = 6909$ ,  $\delta = 0.0001$ . The deviation exceeds 2 % for  $v_r$  close to the leading edge of the tube.

The two boundary conditions used to adapt the shape and strength are  $\Psi_{ring} - \Psi_{wake} = 0$  and  $\Delta H_{sheet} = F$ . With the help of (5.19) and (6.32) this is implemented as:

$$\Delta\Gamma_{ring,i}|_{j+1} = (s_{i+1} - s_i) \frac{\Delta H}{\rho} \frac{d\Gamma}{v_{s,i}} \Big|_j, \quad (\text{D.10})$$

$$\Delta r_{ring,i}|_{j+1} = \frac{\Psi_{ring,i} - \Psi_{wake}}{R_1} \frac{d\Psi}{v_{x,i}} \Big|_j. \quad (\text{D.11})$$

$(s_{i+1} - s_i)$  is the distance between 2 rings,  $d$  is the damping being 0.05 for both boundary conditions.  $\Psi$  is calculated at the vortex core position,  $v_s$  at a position  $r/r_i = 0.95$ . After sufficient convergence is achieved, a second scheme is applied for fine tuning. The dynamic condition (D.10) remains unchanged, while the kinematic condition becomes:

$$\Delta r_{ring,i}|_{j+1} = -\frac{R_1}{U_0} v_{n,i} d_{v_n} \Big|_j. \quad (\text{D.12})$$

with  $v_n$  calculated at the position of the vortex core. This implies that the axial coordinate of the vortex ring is adapted too, as the vortex core position moves normal to the wake boundary surface calculated in the previous iteration. The damping parameters for both conditions are controlled manually, with  $d_\Gamma = d_{v_n} = 0.0001$  as highest damping for both conditions. The first convergence scheme is very robust, while the second scheme requires manual tuning of the damping parameters to convergence. Increasing the damping by lowering  $d$  improves convergence at the cost of longer computation times. The iteration is stopped when both boundary conditions are satisfied with an accuracy better than 2 %.

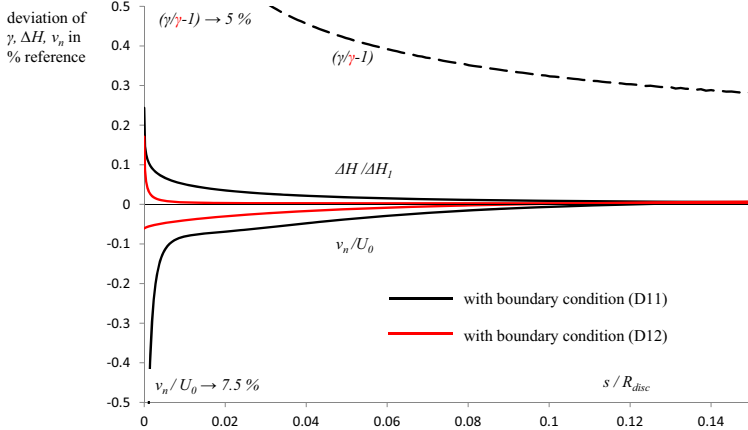


Figure D.3: Deviation of the calculated  $\gamma(s)$ ,  $v_n(s)$  and  $\Delta H(s)$ , for  $C_T = 16/9$ ,  $N = 6909$ ,  $\delta = 0.0001$ . The black lines show the results for satisfied boundary conditions (D.11) and (D.10), the blue lines for satisfied (D.11) and (D.12). For  $\gamma(s)$  the ratio of both solutions is shown. The differences in  $\Psi(s)$  and in the position of the vortex rings (both not shown) are smaller than the difference in  $\Delta H(s)$ . The ratio of the wake contraction for both cases is 1.000035

### D.3. Verification, sensitivity and accuracy

In the first iteration of the convergence scheme, all vortex rings plus the far wake vortex tube constitute a semi-infinite vortex tube of constant strength and diameter starting at  $x = 0$ . Figure D.1 shows the streamlines for the tube flow with  $\gamma_{\text{tube}}/U_0 = -2/3$  placed in a parallel flow  $U_0$ . The vortex model is verified by comparing the numerical results of this first iteration with the analytical solution (D.6) to (D.9).

The accuracy is shown in figure D.2. Except within a distance of 0.02 from the edge of the tube, the deviation is less than 2%. At this leading edge the radial velocity deviates in the order of percentages. The consequence of this becomes clear by comparing the results of the two convergence schemes as shown in figure D.3 for flow state  $C_T = 16/9$ . The effect of  $v_n$  being non-zero close to the edge of the disc has consequences for the distribution of  $\gamma(s)$ , has a 1 % impact on  $\Delta H(s)$  and a negligible impact on  $\Psi(s)$ , as well as  $r_{\text{rings}}(x)$ . Apparently the difference in  $\gamma(s)$  does not affect the other flow properties more than 2 %. Furthermore, it appears that the numerical discretisation and convergence scheme give an uncertainty of several % in  $v_n(s)$  or in  $\gamma(s)$  close to the leading edge. The insensitivity for the other flow parameters has been checked for all  $0 > C_T \geq -0.96$  with  $N = 4656$ ,  $\delta = 0.001$ : the difference in using (D.11) or (D.12) leads to differences in  $r_{\text{rings}}(x)$ ,  $\Psi(s)$  and  $\Delta H(s)$  of less than 3 %, but the normal velocity close to the leading edge deviates percentages of  $U_0$ . For more negative  $C_T$  the difference grows: 1% for  $C_T = -0.995$ . When (D.12) is used,  $v_n$  is also less than 2 % of  $U_0$  while the other conditions remain the same.

Table D.1: Sensitivity of  $R/R_1$  for  $C_T = -8/9$ , in % deviation from the momentum theory value.

$N \downarrow \delta \rightarrow$	0.0015	0.001	0.0005	0.0001
6909				0.98
4956			0.99	0.98
4656		0.75	0.71	0.10
4355	0.59			

Table D.2: Number of vortex rings of which the vortex core overlaps with the core of the neighbouring ring, for  $C_T = -8/9$ .

$N \downarrow \delta \rightarrow$	0.0015	0.001	0.0005	0.0001
6909				0
4956			0	0
4656		14	2	0
4355	0			

The numerical method has 2 independent model parameters: the number of rings  $N$  and the vortex core radius  $\delta/R_1$ . A sensitivity analysis for both parameters has resulted in table D.1. It is clear that the results are insensitive to variations in both parameters. However, this is not the case for the properties of the vortex sheet close to its leading edge. table D.2 shows that for some of the combination the vortex cores of the very first rings may overlap:

The overlap has an impact on the position of the rings and the distribution  $\gamma$ : the shape and strength of the vortex sheet are not smooth enough. An example is shown in [van Kuik and Lignarolo \(2016, figure 9\)](#) showing the distribution of  $\gamma$  as calculated with  $N = 4656$  and  $\delta = 0.001$ . The anomalous value at  $s = 0$  is caused by the overlap of the first ring with the second one. For all calculations done with  $N = 6909$  and  $\delta = 0.0001$  there is no overlap yielding a smooth  $\gamma$  distributions, as shown in figures 5.9 and 6.8. All analyses in chapter 5 showing details of boundary conditions and  $\gamma$  have been done with  $N = 6909$ ,  $\delta = 0.0001$ .

Finally, the computed values of the disc-averaged velocity at the disc have been compared with the values of momentum theory. In the wind turbine regime deviations are less than 2% for  $C_T < -0.96$ , increasing up to 1.5% for  $C_T = -0.998$ . In the propeller regime all results shown in figure 5.4 have the same accuracy.

The conclusions of this section are:

- The vortex model is verified by comparison with an analytical solution of the semi-infinite vortex tube, yielding deviations in local velocity vectors less than 2 % for  $N = 6909$ ,  $\delta = 0.0001$ , except for the velocity component normal to the vortex sheet within a distance  $0.02R_{tube}$  from its leading edge.
- By comparison of solutions converged to a constant stream function  $\Psi$ , having similar deviations in normal velocity, with solutions converged to constant  $\Psi$

and  $v_n \leq 0.0002U_0$  it has been shown that calculated flow properties differ less than 3 %, except for  $\gamma$  deviating more for  $s/R_{disc} < 0.13$ .

- By this uncertainty in  $\gamma$  or  $v_n$  close to the disc edge, accurate quantitative conclusions with respect to the vortex sheet strength close to the disc edge are not possible. Qualitative conclusions are possible as the accuracy is limited to a few %. It has an effect of  $\leq 3\%$  on other flow parameters.
- The results are, with deviations of 2%, insensitive to variations in  $N$  and  $\delta$ . The smoothness of the wake boundary vorticity distribution increases with higher  $N$ .
- The overall accuracy is assessed at 3%, except for flow details within a distance of  $0.13R_{disc}$  from the disc edge, and for  $C_T < -0.96$ .

This page intentionally left blank

## Bibliography

- Akay, B.; Ferreira, C.S., and van Bussel, G.J.W. 2012, Experimental and Numerical Quantification of Radial Flow in the Root Region of a HAWT. *AIAA 50th Aerospace Science Meeting*, AIAA 2012-(January):1–10. doi: pdf/10.2514/6.2012-896.
- Anderson, H.B.; Milborrow, D.J., and Ross, J.N. 1982, Performance and wake measurements on a 3 m diameter horizontal axis wind turbine rotor. In *Proc. 4th Int'l. Symposium on Wind Energy Systems. Stockholm, BHRA*, 1982.
- Anderson Jr, J.D. 2011, *Fundamentals of Aerodynamics*. McGraw-Hill, Singapore. ISBN 0073398101. doi: 10.1036/0072373350.
- Batchelor, G.K. 1970, *An introduction to fluid dynamics*. Cambridge University Press, Cambridge. doi: 10.1017/CBO9780511800955.
- Bendemann, F. 1910, Luftschraubenuntersuchenden. *Zeitschrift für Flugtechnik und Motorluftschiffahrt*, 7:177–198.
- Betz, A. 1919, *Schraubenpropeller mit geringstem Energieverlust*. Reprint of 4 famous papers by Universitatsverlag Göttingen.
- Betz, A. 1920, Das Maximum der theoretisch möglichen Ausnutzung des Windes durch Windmotoren. *Zeitschrift für das gesamte Turbinenwesen*, 26:307–309.
- Betz, A. 1921, Vortices and the related principles of hydrodynamics. *Naca TN 68, translated from Zeitschrift für Flugtechnik und Motorluftschiffart*.
- Betz, A. 1926, *Wind-Energie und ihre Ausnutzung durch WindMühlen*. Vandenhoeck & Ruprecht, Göttingen.
- Betz, A. 1950, Wie entsteht ein Wirbel in einer wenig zähen Flüssigkeit? *Die Naturwissenschaften*, 37(9):7–10.
- Bothezat, G. 1917, Research of work phenomenon for propeller with blades, Petrograd 1917. English translation in: *The General Theory of Blade Screw, Chapter 3. NACA Report*, 29: 198–225.
- Bragg, S.L. and Hawthorne, W.R. 1950, Some exact solutions of the flow through annual cascade actuator discs. *J. Aeronaut. Sci.* 17, 243249. *Journal of the Aeronautical Sciences*, 17(4):243–249.
- Branlard, E. 2017, *Wind Turbine Aerodynamics and Vorticity-Based Methods*. Springer International Publishing. ISBN 9783319551630. doi: 10.1007/978-3-319-55164-7.
- Branlard, E and Gaunaa, M. 2015, Cylindrical vortex wake model : right cylinder. *Wind Energy*, 18(11):1973–1987. doi: 10.1002/we.1800.
- Branlard, E.; Dixon, K., and Gaunaa, M. 2013, Vortex methods to answer the need for improved understanding and modelling of tip-loss factors. *IET Renewable Power Generation*, 7(4):311–320. ISSN 1752-1416. doi: 10.1049/iet-rpg.2012.0283.
- Branlard, E; Gaunaa, M, and Machefaux, E. 2014, Investigation of a new model accounting for rotors of finite tip-speed ratio in yaw or tilt. *Journal of Physics: Conference Series*, 524 (Torque2014):012124. ISSN 1742-6596. doi: 10.1088/1742-6596/524/1/012124.
- Breslin, J. P. and Andersen, P. 1994, *Hydrodynamics of ship propellers*. Cambridge University Press. ISBN 0521413605.
- Burton, T.; Jenkins, N.; Sharpe, D.J., and Bossanyi, E. 2011, *Wind Energy Handbook*. Wiley. ISBN 9780471489979. doi: 10.1002/0470846062.
- Calaf, M.; Meneveau, C., and Meyers, J. 2010, Large eddy simulation study of fully developed wind-turbine array boundary layers. *Physics of Fluids*, 22(1):1–16. ISSN 10706631. doi: 10.1063/1.382466.

- Churchfield, M.; Lee, S.; Moriarty, P.; Martinez, L.; Leonardi, S.; Vijayakumar, G., and Brasseur, J. 2012, A Large-Eddy Simulations of Wind-Plant Aerodynamics. *50th AIAA Aerospace Sciences Meeting*, (January):1–19. doi: 10.2514/6.2012-537.
- Clancy, L.J. 1986, *Aerodynamics*. reprint by Longman Scientific & Technical, London. ISBN 0582988802, 9780582988804.
- Conway, J.T. 1998, Exact actuator disk solutions for non-uniform heavy loading and slip-stream contraction. *Journal of Fluid Mechanics*, 365:235–267. ISSN 00221120. doi: 10.1017/S0022112098001372.
- Corten, G.P. 2001a, Aspect ratio correction for wind turbine blades. In *presentation at the IEA Joint Action Aerodynamics of Wind turbines, 15th symposium*, Athens.
- Corten, G.P. 2001b, Novel Views on the Extraction of Energy from Wind-Heat Generation and Terrain Concentration. In *EWEC2001 Copenhagen*, pages 1–5, 2001b.
- Courant, R. and Hilbert, D. 1967, *Methoden der mathematischen Physik II*. Springer Verlag, Berlin, Heidelberg. ISBN 978-3-642-58039-0.
- Crawford, C. 2006, Re-examination of the Precepts of the Blade Element Momentum Theory for Coning Rotors. *Wind Energy*, 9:457–478. doi: 10.1002/we.197.
- Craze, D.J. 1977, On the near wake behind a circular disc. *6th Australasian Hydraulics and Fluid Mechanics Conference*, pages 282–286.
- Darmofal, D.L. 1993, The Role of Vorticity Dynamics in Vortex Breakdown, AIAA 93-3036. In *AIAA 24th Fluid Dynamic conference*, number 5, pages 1–14, 1993.
- de Vries, O. 1979, *Fluid dynamic aspects of wind energy conversion*, AGARD-AG-243. AGARD, Amsterdam. ISBN ISBN, 9283513266, 9789283513261.
- del Campo, V.; Ragni, D.; Micallef, D.; Akay, B.; Diez, J., and Ferreira, C. S. 2013, Non intrusive 3D load calculation during yaw conditions. In *EWEA2013*, 2013.
- del Campo, V.; Ragni, D.; Micallef, D., and Akay, B. 2014, 3D load estimation on a horizontal axis wind turbine using SPIV. *Wind Energy*, 17(11):1645–1657. doi: 10.1002/we.1658.
- del Campo, V.; Ragni, D.; Micallef, D.; Diez, J., and Simão Ferreira, C. J. 2015, Estimation of loads on a horizontal axis wind turbine. *Wind Energy*, 18(11):1875–1891. doi: 10.1002/we.1658.
- El khchine, Y. and Sriti, M. 2017, Tip Loss Factor Effects on Aerodynamic Performances of Horizontal Axis Wind Turbine. *Energy Procedia*, 118:136–140. ISSN 18766102. doi: 10.1016/j.egypro.2017.07.028.
- Fleming, P.; Gebraad, P.M.O.; Lee, S.; Van Wingerden, J.W.; Johnson, K.; Churchfield, M.; Michalakes, J.; Spalart, P., and Moriarty, P. 2015, Simulation comparison of wake mitigation control strategies for a two-turbine case. *Wind Energy*, 18:2135–2143. doi: 10.1002/we.1658.
- Froude, R.E. 1889, On the part played in propulsion by differences of fluid pressure. *13th Session of the Institution of Naval Architects*, 30:390–405.
- Glauert, H. 1926, The analysis of experimental results in the windmill brake and vortex ring state of an airscrew, ARC R&M 1026. Technical report.
- Glauert, H. 1935, *The General Momentum Theory*, in: *Aerodynamic Theory volume IV division L*. Springer, reprinted as Dover Edition.
- Goldstein, S. 1929, On the vortex theory of screw propellers. *Proc. R. Soc. Lond. A*, 123: 440–465.
- Goorjian, P.M. 1972, An Invalid Equation in the General Momentum Theory of the Actuator Disk. *AIAA journal*, 10(4):543–544.
- Gray, R.B.; McMahon, H.M.; Shenoy, K.R., and Hammer, M.L. 1980, Surface pressure measurements at two tips of a model helicopter rotor in hover. *NASA CR3281*.
- Greenberg, M.D. 1972, Nonlinear actuator disk theory. *Zeitschrift für Flugwissenschaften*, 20: 90–98.
- Haans, W.; Sant, T.; Van Kuik, G.A.M., and van Bussel, G.J.W. 2008, HAWT Near-Wake Aerodynamics, Part I: Axial Flow Conditions. *Wind Energy*, 11:245–264. doi: 10.1002/we.262.
- Hand, M.M.; Simms, D.A.; Fingersh, L.J.; Jager, D.W.; Cotrell, J.R.; Schreck, S., and Larwood, S.M. 2001, Unsteady aerodynamics experiment phase VI: wind tunnel test configurations and available data campaigns. Technical report, Tech Rep. NREL/TP-500-29955. National Renewable Energy Laboratory.
- Hansen, M.O.L. 2008, *Aerodynamics of Wind Turbines*. Earthscan. ISBN 9781844074389.

- Helmholtz, H. 1858, Über Integrale der hydrodynamischen Gleichungen, welche den Wirbelbewegungen entsprechen. *Journal für die reine und angewandte Mathematik*, 55:25–55.
- Herráez, I.; Medjroubi, W.; Stoevesandt, B., and Peinke, J. 2014a, Aerodynamic Simulation of the MEXICO Rotor. *Journal of Physics: Conference Series*, 555:012051. ISSN 1742-6588. doi: 10.1088/1742-6596/555/1/012051.
- Herráez, I.; Stoevesandt, B., and Peinke, J. 2014b, Insight into Rotational Effects on a Wind Turbine Blade Using NavierStokes Computations. *Energies*, 7(10):6798–6822. ISSN 1996-1073. doi: 10.3390/en7106798.
- Herráez, I.; Micallef, D., and Van Kuik, G.A.M. 2017, Influence of the conservative rotor loads on the near wake of a wind turbine. *Journal of Physics: Conference Series*, 854(1):1–10. ISSN 17426596. doi: 10.1088/1742-6596/854/1/012022.
- Hoff, W. 1921, Theory of the ideal windmill, NACA TN 46. Technical report.
- Hölling, M.; Peinke, J., and Ivanell, S., editors. 2014, *Wind Energy - Impact of Turbulence*. Springer Verlag, Berlin, Heidelberg. ISBN 978-3-642-54696-9. doi: 10.1007/978-3-642-54696-9.
- Horlock, J.H. 1978, *Actuator Disc Theory*. McGraw-Hill. ISBN 978-0070303607.
- Joukowsky, J.N. 1912, Vortex theory of the screw Propeller I. *Trudy Avia Raschetno- Ispytatel'nogo Byuro (in Russian) Also published in Gauthier-Villars et Cie. (eds). Théorie Tourbillonnaire de l'Hélice Propulsive, Quatrième Mémoire*. 1929; 1: 147., 16(1):1–31.
- Joukowsky, J.N. 1914, Vortex theory of the screw propeller II. *Trudy Avia Raschetno- Ispytatel'nogo Byuro (in Russian) Also published in Gauthier-Villars et Cie. (eds). Théorie Tourbillonnaire de l'Hélice Propulsive, Quatrième Mémoire*. 1929; 2: 4893., 17(1):1–33.
- Joukowsky, J.N. 1915, Vortex theory of the screw propeller III. *Trudy Avia Raschetno- Ispytatel'nogo Byuro (in Russian) Also published in Gauthier-Villars et Cie. (eds). Théorie Tourbillonnaire de l'Hélice Propulsive, Quatrième Mémoire*. 1929; 3: 4893., 17(2):1–23.
- Joukowsky, J.N. 1918, Vortex theory of the screw propeller IV. *Trudy Avia Raschetno- Ispytatel'nogo Byuro (in Russian) Also published in Gauthier-Villars et Cie. (eds). Théorie Tourbillonnaire de l'Hélice Propulsive, Quatrième Mémoire*. 1929; 4: 123198, 3:1–97.
- Joukowsky, J.N. 1920, Joukowsky windmills of the NEJ type. *Transactions of the Central Institute for Aero-Hydrodynamics of Moscow*, pages 405–430.
- Katz, J. and Plotkin, A. 2001, *Low-speed aerodynamics*. Cambridge University Press, New York, second edition. ISBN 9780511810329. doi: 10.1017/CBO9780511810329.
- Küchemann, F.R.S. 1978, *The aerodynamic design of aircraft*. Pergamon Press.
- Kundu, P.K. 1990, *Fluid Mechanics*. Academic Press Inc. ISBN 978-0123821003.
- Lanchester, F.W. 1907, *Aerodynamics*. A. Constable & co. ltd., London.
- Lanchester, F.W. 1915, A contribution to the theory of propulsion and the screw propeller. *Fifty-sixth session of the Institution of Naval Architects*.
- Leishman, J.G. 2006, *Principles of Helicopter Aerodynamics*, 2nd edition. Cambridge University Press. ISBN 0521858607, 9780521858601.
- Lighthill, J. 1986, *An informal introduction to fluid mechanics*. Clarendon Press, Oxford. ISBN 0198536313, 9780198536314.
- Lignarolo, L.E.M.; Ferreira, C.S., and van Bussel, G.J.W. 2016a, Experimental comparison of a wind turbine and of an actuator disc wake. *Journal of Renewable and Sustainable Energy*, 8(023301):1–26. ISSN 1941-7012. doi: 10.1063/1.4941926.
- Lignarolo, L.E.M.; Mehta, D.; Stevens, R.J.A.M.; Yilmaz, A.E.; Meyers, J.; Andersen, S J; Van Kuik, G.A.M.; Meneveau, C.; Holierhoek, J.; Simão Ferreira, C.J.; Ragni, D., and van Bussel, G.J.W. 2016b, Validation of four LES and a vortex model against PIV measurements of the near wake of an actuator disk and a wind turbine. *Renewable Energy*, 94:510–523. ISSN 09601481. doi: 10.1016/j.renene.2016.03.070.
- Madsen, H.A. 1996, A CFD analysis of the actuator disc flow compared with momentum theory results. *10th IEA Aerodynamic Expert Meeting*, pages 109–124.
- Madsen, H.A. and Paulsen, U.S. 1990, An integrated rotor and turbulent wake model compared with experiment. In *European Community Wind Energy Conference*, pages 269–273, Madrid.
- Madsen, H.A.; Mikkelsen, R.F.; Øye, S.; Bak, C., and Johansen, J. 2007, A Detailed investigation of the Blade Element Momentum (BEM) model based on analytical and numerical results and proposal for modifications of the BEM model. *Journal of Physics: Conference*

- Series*, 75:012016. ISSN 1742-6596. doi: 10.1088/1742-6596/75/1/012016.
- Madsen, H.A.; Bak, C.; Døssing, M.; Mikkelsen, R.F., and Øye, S. 2010, Validation and modification of the Blade Element Momentum theory based on comparisons with actuator disc simulations. *Wind Energy*, 13:373–389. doi: 10.1002/we359.
- Maniaci, D. and Schmitz, S. 2016, Extended Glauert Tip Correction to Include Vortex Rollup Effects. *Journal of Physics: Conference Series*, 753:022051. ISSN 1742-6588. doi: 10.1088/1742-6596/753/2/022051.
- Manwell, J.F.; McGowan, J.G., and Rogers, A.L. 2009, *Wind energy explained*. John Wiley & Sons, Ltd, 2nd edition. ISBN 9780470015001. doi: 10.1002/9781119994367.
- Marshall, J.S. 2001, *Inviscid Incompressible Flow*. John Wiley and Sons. ISBN 978-0-471-37566-1.
- Martínez-Tossas, L.A.; Churchfield, M.J., and Meneveau, C. 2017, Optimal smoothing length scale for actuator line models of wind turbine blades based on Gaussian body force distribution. *Wind Energy*, 20(6):1083–1096. doi: 10.1002/we.2081.
- Medici, D. and Alfredsson, P.H. 2006, Measurements on a wind turbine wake: 3D effects and bluff body vortex shedding. *Wind Energy*, 9:219–236. doi: 10.1002/we.156.
- Meyer, R.E. 1982, *Introduction to mathematical fluid dynamics*. Dover Publications Inc., New York. ISBN 978-0486615547.
- Micallef, D. 2012, *3D flows near a HAWT rotor*. PhD thesis, available at TU-Delft repository and U Malta. ISBN 9789995703134. doi: 10.4233/uuid:ca471701-2817-4a36-9839-4545c1cce45.
- Micallef, D.; van Bussel, G.J.W.; Ferreira, C.S., and Sant, T. 2013, An investigation of radial velocities for a horizontal axis wind turbine in axial and yawed flows. *Wind Energy*, 16: 529–544. doi: 10.1002/we.1503.
- Micallef, D.; Akay, B.; Ferreira, C.S.; Sant, T., and van Bussel, G.J.W. 2014, The origins of a wind turbine tip vortex. *Journal of Physics: Conference Series*, 012074(1). ISSN 17426596. doi: 10.1088/1742-6596/555/1/012074.
- Micallef, D.; Simão Ferreira, C.J.; Sant, T., and van Bussel, G.J.W. 2018, Experimental and numerical investigation of tip vortex generation and evolution on horizontal axis wind turbines. *Wind Energy*, 19(8):1485–1501. doi: 10.1002/we.1932.
- Mikkelsen, R.F. personal communication at the Visby Wake conference, 2011.
- Mikkelsen, R.F.; Øye, S.; Sørensen, J.N.; Madsen, H.A., and Shen, W.Z. 2009, Analysis of Wake Expansion and Induction near Tip. In *Proceedings EWEC2009*, Marseille.
- Milne-Thomson, L.M. 1966, *Theoretical Aerodynamics*. MacMillan and Company Ltd, republished in 1973 by Dover Publications. ISBN 048661980X, 9780486619804.
- Morrison, P.J. 2006, *Hamiltonian Fluid Dynamics*, volume 2. Elsevier, Amsterdam. doi: 10.1016/B0-12-512666-2/00246-7.
- Morton, B.R. 1984, The generation and decay of vorticity. *Geophysical & Astrophysical Fluid Dynamics*, 28:277–308. doi: 10.1080/03091928408230368.
- Munk, M. 1920, Wind-driven propellers (or "windmills"), from *Zeitschrift für Flugtechnik und Motorluftschiffart*, NACA TM 201. Technical report.
- Okulov, V.L. 2014, Limit cases for rotor theories with Betz optimization. *Journal of Physics: Conference Series*, 524:012129. ISSN 1742-6596. doi: 10.1088/1742-6596/524/1/012129.
- Okulov, V.L. and Sørensen, J. N. 2010, Maximum efficiency of wind turbine rotors using Joukowsky and Betz approaches. *Journal of Fluid Mechanics*, 649:497–508. ISSN 0022-1120. doi: 10.1017/S0022112010000509.
- Okulov, V.L. and Sørensen, J.N. 2008, Refined Betz limit for rotors with a finite number of blades. *Wind Energy*, 11(4):415–426. ISSN 10954244. doi: 10.1002/we.274.
- Okulov, V.L. and van Kuik, G.A.M. 2012, The Betz Joukowsky limit : on the contribution to rotor aerodynamics by the British, German and Russian scientific schools. *Wind Energy*, 15: 335–344. doi: 10.1002/we.464.
- Okulov, V.L.; Sørensen, J.N., and Wood, D.H. 2015, Rotor theories by Professor Joukowsky: Vortex Theories. *Progress in Aerospace Sciences*, 73:19–46. ISSN 03760421. doi: 10.1016/j.paerosci.2014.10.002.
- Øye, S. 1990, A simple vortex model. In McAnulty, K. F., editor, *Third IEA Symposium on the Aerodynamics of Wind Turbine*, pages 1–15, Harwell. ETSU.

- Parra, E.A.; Boorsma, K.; Schepers, J.G., and Snel, H. 2016, Momentum considerations on the New MEXICO experiment. *Journal of Physics: Conference Series*, 753:072001. ISSN 1742-6588. doi: 10.1088/1742-6596/753/7/072001.
- Paxton, F. 1959, Solid Angle Calculation for a Circular Disk. *The review of scientific instruments*, 30(4):254–258.
- Porté-Agel, F.; Wu, T.Y.; Lu, H., and Conzemius, R.J. 2011, Large-eddy simulation of atmospheric boundary layer flow through wind turbines and wind farms. *Journal of Wind Engineering and Industrial Aerodynamics*, 99(4):154–168. ISSN 01676105. doi: 10.1016/j.jweia.2011.01.011.
- Prandtl, L. 1918, Tragflügeltheorie I. Mitteilung. *Nachrichten der Königlichem Gesellschaft der Wissenschaften zü Göttingen, Mathematisch-physikalische Klasse*, pages 451–477.
- Prandtl, L. Über die Entstehung von Wirbeln in der idealen Flüssigkeit, mit Anwendung auf die Tragflügeltheorie und andere Aufgaben. In *von Kármán, Levi-Cevita (Eds.), Vorträge aus dem Gebiete der Hydro- und Aerodynamik*, pages 18–33. Springer, Berlin, 1924.
- Ragni, D.; Oudheusden, B.W., and Scarano, F. 2011a, Non-intrusive aerodynamic loads analysis of an aircraft propeller blade. *Experiments in Fluids*, 51(2):361–371. ISSN 0723-4864. doi: 10.1007/s00348-011-1057-7.
- Ragni, D.; Oudheusden, B.W., and Scarano, F. 2011b, 3D pressure imaging of an aircraft propeller blade-tip flow by phase-locked stereoscopic PIV. *Experiments in Fluids*, 52(2): 463–477. ISSN 0723-4864. doi: 10.1007/s00348-011-1236-6.
- Rankine, W.J.M. 1865, On the mechanical principles of the action of propellers. In *6th session of the Institution of Naval Architects*, number 9, pages 13–19, 1865.
- Rathakrishnan, E. 2013, *Theoretical Aerodynamics*. John Wiley & Sons, Ltd. ISBN 1118479378, 9781118479377.
- Réthoré, P.-E.; van der Laan, P.; Troldborg, N.; Zahle, F., and Sørensen, N. 2014, Verification and validation of an actuator disc model. *Wind Energy*, 17:919–937. doi: 10.1002/we.1607.
- Rosen, A. and Gur, O. 2008, Novel Approach to Axisymmetric Actuator Disk Modeling. *AIAA Journal*, 46(11):2914–2925. ISSN 0001-1452. doi: 10.2514/1.37383.
- Saffman, P.G. 1992, *Vortex Dynamics*. University Press., Cambridge, monographs edition. ISBN 052142058X, 9780521420587.
- Sanderse, B. 2011, Review of computational fluid dynamics for wind turbine wake aerodynamics. *Wind Energy*, 14:799–819. doi: 10.1002/we.458.
- Schaffarczyk, A.P. 2014, *Introduction to wind turbine aerodynamics*. Springer Verlag, Berlin-Heidelberg. ISBN 3642364098, 9783642364099. doi: 10.1007/978-3-642-36409-9.
- Schepers, J.G. 2012, *Engineering models in wind energy aerodynamics*. PhD thesis, available at TU-Delft repository. ISBN 9789461915078.
- Schepers, J.G. and Snel, H. 2007, Model experiments in controlled conditions (MEXICO). Technical report, ECN Report ECN-E-07042.
- Schepers, J.G.; Boorsma, K, and Munduate, X. 2014, Final Results from Mexnext-I: Analysis of detailed aerodynamic measurements on a 4.5 m diameter rotor placed in the large German Dutch Wind Tunnel DNW. *Journal of Physics: Conference Series*, 555:012089. ISSN 1742-6588. doi: 10.1088/1742-6596/555/1/012089.
- Schmidt, G.H. and Sparenberg, J.A. 1977, On the edge singularity of an actuator disk with large constant normal load. *Journal of Ship Research*, 21(2):125–131.
- Schmitz, S. and Maniaci, D.C. 2016, Analytical Method to Determine a Tip Loss Factor for Highly-Loaded Wind Turbine Rotors. *34th Wind Energy Symposium at AIAA SciTech Forum*, pages 1–16. doi: 10.2514/6.2016-0752.
- Segalini, A. and Alfredsson, P.H. 2013, A simplified vortex model of propeller and wind-turbine wakes. *Journal of Fluid Mechanics*, 725:91–116. ISSN 0022-1120. doi: 10.1017/jfm.2013.182.
- Sharpe, D.J. jul 2004, A general momentum theory applied to an energy-extracting actuator disc. *Wind Energy*, 7(3):177–188. ISSN 1095-4244. doi: 10.1002/we.118.
- Shen, W.Z.; Mikkelsen, R.F.; Sørensen, J.N., and Bak, C. 2005a, Tip loss corrections for wind turbine computations. *Wind Energy*, 8(4):457–475. ISSN 1095-4244. doi: 10.1002/we.153.
- Shen, W.Z.; Sørensen, J.N., and Mikkelsen, R.F. 2005b, Tip Loss Correction for Actuator/NavierStokes Computations. *Journal of Solar Energy Engineering*, 127(2):209. ISSN 01996231. doi: 10.1115/1.1850488.

- Shen, W.Z.; Zhu, W. J., and Sørensen, J.N. 2014, Study of tip loss corrections using CFD rotor computations. *Journal of Physics: Conference Series*, 555:012094. ISSN 1742-6588. doi: 10.1088/1742-6596/555/1/012094.
- Shives, M. and Crawford, C. 2013, Mesh and load distribution requirements for actuator line CFD simulations. *Wind Energy*, 16:1183–1196. doi: 10.1002/we.1546.
- Sibuet Watters, C.; Breton, S. P., and Masson, C. 2010, Application of the actuator surface concept to wind turbine rotor aerodynamics. *Wind Energy*, 13(5):433–447. doi: 10.1002/we.365.
- Simão Ferreira, C.J. 2009, *The near wake of the VAWT: 2D and 3D views of the VAWT aerodynamics*. PhD thesis, TU Delft repository.
- Snel, H. and Schepers, J.G. 1995, Joint investigation of dynamic inflow effects and implementation of an engineering method. Technical report, ECN-C-94-107.
- Sørensen, J.N. 2011, Aerodynamic Aspects of Wind Energy Conversion. *Annual Review of Fluid Mechanics*, 43(1):427–448. ISSN 0066-4189. doi: 10.1146/annurev-fluid-122109-160801.
- Sørensen, J.N. 2015, *General momentum theory for horizontal axis wind turbines*. Springer International Publishing, Heidelberg. ISBN 978-3-319-22113-7. doi: 10.1007/978-3-319-22114-4.
- Sørensen, J.N. and Mikkelsen, R.F. 2001, On the validity of the blade element momentum method. In *EWEC2001*, pages 362–366, Copenhagen.
- Sørensen, J.N. and Myken, A. 1992, Unsteady actuator disc model for horizontal axis wind turbines. *Journal of Wind Engineering and Industrial ...*, 39:139–149.
- Sørensen, J.N. and Shen, W.Z. 2002, Numerical Modeling of Wind Turbine Wakes. *Journal of Fluids Engineering*, 124(2):393. ISSN 00982202. doi: 10.1115/1.1471361.
- Sørensen, J.N. and van Kuik, G.A.M. 2011, General momentum theory for wind turbines at low tip speed ratios. *Wind Energy*, 14:821–839. doi: 10.1002/we.423.
- Sørensen, J.N.; Shen, W.Z., and Munduate, X. 1998, Analysis of wake states by a full field actuator disc model. *Wind Energy*, 88:73–88. doi: 10.1002/(SICI)1099-1824(199812)1:2<73::AID-WE12>3.0.CO;2-L.
- Sørensen, J.N.; Dag, K.O., and Ramos-García, N. 2015, A refined tip correction based on decambering. *Wind Energy*, 19(5):787–802. doi: 10.1002/we.1865.
- Sørensen, J.N.; Okulov, V.L.; Mikkelsen, R.F.; Naumov, I.V., and Litvinov, I.V. 2016, Comparison of classical methods for blade design and the influence of tip correction on rotor performance. *Journal of Physics: Conference Series*, 753(Torque):022020. ISSN 1742-6588. doi: 10.1088/1742-6596/753/2/022020.
- Spalart, P.R. 2003, On the simple actuator disk. *Journal of Fluid Mechanics*, 494:399–405. ISSN 00221120. doi: 10.1017/S0022112003006128.
- Stepniewski, W.Z. and Keys, S.N. 1978, *Rotary wind aerodynamics*. Dover Publications Inc., New York. ISBN 978-0486646473.
- Stevens, R.J.A.M. and Meneveau, C. 2017, Flow Structure and Turbulence in Wind Farms. *Annual Review of Fluid Mechanics*, 49(1):311–339. ISSN 0066-4189. doi: 10.1146/annurev-fluid-010816-060206.
- Thoma, D. 1925, Grundsätzliches zur einfachen Strahltheorie der Schraube. *Zeitschrift für Flugtechnik und Motorluftschiffahrt*, 16(10):206–208.
- Thwaites, B. 1960, *Incompressible aerodynamics*. Clarendon Press, Oxford. ISBN 978-0486654652.
- Troldborg, N.; Sørensen, J.N., and Mikkelsen, R.F. 2010, Numerical simulations of wake characteristics of a wind turbine in uniform inflow. *Wind Energy*, 13:86–99. doi: 10.1002/we.345.
- van Holten, T. 1981, Concentrator systems for wind energy, with emphasis on tip-vanes. *Wind Engineering*, 5(1):29–45.
- van Kuik, G.A.M. 1989, Experimental verification of an improved actuator disc concept. In *Proceedings of the 15th European Rotorcraft Forum*, Amsterdam.
- van Kuik, G.A.M. 2004, The flow induced by Prandtl's self-similar vortex sheet spirals at infinite distance from the spiral kernel. *European Journal of Mechanics - B/Fluids*, 23(4):607–616. ISSN 09977546. doi: 10.1016/j.euromechflu.2004.01.002.
- van Kuik, G.A.M. 2007, The Lanchester - Betz - Joukowsky limit. *Wind Energy*, 10(3):289–291. ISSN 10954244. doi: 10.1002/we.218.

- van Kuik, G.A.M. 2009, A steady solution for Prandtl's self-similar vortex sheet spirals. *European Journal of Mechanics - B/Fluids*, 28(2):296–298. ISSN 09977546. doi: 10.1016/j.euromechflu.2008.05.007.
- van Kuik, G.A.M. 2016, Momentum theory of Joukowsky actuator discs with swirl. *Journal of Physics: Conference Series*, 753:022021. ISSN 1742-6588. doi: 10.1088/1742-6596/753/2/022021.
- van Kuik, G.A.M. 2017, Joukowsky actuator disc momentum theory. *Wind Energy Science*, 2: 307–316. ISSN 2366-7621. doi: 10.5194/wes-2016-55.
- van Kuik, G.A.M. 2018, Comparison of actuator disc flows representing wind turbines and propellers. *Journal of Physics Conference Series*, accepted.
- van Kuik, G.A.M. and Lignarolo, L.E.M. 2016, Potential flow solutions for energy extracting actuator disc flows. *Wind Energy*, 19:1391–1406. doi: 10.1002/we.1902.
- van Kuik, G.A.M.; Micallef, D.; Herraez, I.; van Zuijlen, A.H., and Ragni, D. 2014, The role of conservative forces in rotor aerodynamics. *Journal of Fluid Mechanics*, 750:284–315. ISSN 0022-1120. doi: 10.1017/jfm.2014.256.
- van Kuik, G.A.M.; Sørensen, J.N., and Okulov, V.L. 2015a, Rotor theories by Professor Joukowsky: Momentum theories. *Progress in Aerospace Sciences*, 73:1–18. ISSN 03760421. doi: 10.1016/j.paerosci.2014.10.001.
- van Kuik, G.A.M.; Yu, W.; Sarmast, S., and Ivanell, S. 2015b, Comparison of actuator disc and Joukowsky rotor flows, to explore the need for a tip correction. *Journal of Physics Conference Series*, 625:012013. doi: 10.1088/1742-6596/625/1/012013.
- van Kuik, G.A.M.; Peinke, J.; Nijssen, R.; Lekou, D.; Mann, J.; Ferreira, C.S.; van Wingerden, J.W.; Schlipf, D.; Gebraad, P.; Polinder, H.; Abrahamsen, A.; van Bussel, G.J.W.; Tavner, P.; Bottasso, C.L.; Muskulus, M.; Matha, D.; Lindeboom, H.J.; Degraer, S.; Kramer, O.; Lehnhoff, S.; Sonnenschein, M.; Morthorst, P.E., and Skytte, K. 2016, Long-term research challenges in wind energy a research agenda by the European Academy of Wind Energy. *Wind Energy Science*, 1(1):1–39. ISSN 2366-7443. doi: 10.5194/wes-1-1-2016.
- Vetchinkin, V. P. 1913, Calculation of screw propeller, part I. *Buletenei Politekhnicheskogo obshchestva (in Russian)*, 5.
- Vetchinkin, V. P. 1918, Calculation of screw propeller, part II. *Trudy Avia Raschetno-Ispytatelnogo Byuro*, 4:1–129.
- von Kármán, Th. and Burgers, T.M. Motion of a perfect fluid produced by external forces. In Durand, W.F., editor, *Aerodynamic Theory, Volume II, Division E, chap. IIIA*. Springer Verlag, 1935.
- Wald, Q.R. 2006, The aerodynamics of propellers. *Progress in Aerospace Sciences*, 42(2):85–128. ISSN 03760421. doi: 10.1016/j.paerosci.2006.04.001.
- Wimshurst, S.; Metherell, A.J.F.; Wilson, D.M.A.; Milborrow, D.J., and Ross, J. N. 1984, Wind turbine rotor performance in the high thrust region. In *Sixth BWEE Conference*, 1984.
- Wilson, R.E. and Lissaman, P.B.S. 1974, Applied aerodynamics of wind power machines. *NASA STI/Recon. Technical Report N*, 75(May):22669. doi: 10.1007/978-3-642-91487-4-3.
- Wimshurst, A. and Wilden, R. H. J. 2017, Analysis of a tip correction factor for horizontal axis turbines. *Wind Energy*. ISSN 10954244. doi: 10.1002/we.2106.
- Wimshurst, A. and Wilden, R.H.J. 2018, Computational observations of the tip loss mechanism experienced by horizontal axis rotors. *Wind Energy*, (Early View):1–14. ISSN 10954244. doi: 10.1002/we.2177.
- Wood, D.H. 2007, Including swirl in the actuator disk analysis of wind turbines. *Wind Engineering*, 31(5):317–323.
- Wood, D.H. 2015, Maximum wind turbine performance at low tip speed ratio. *Journal of Renewable and Sustainable Energy*, 7:053126. doi: 10.1063/1.4934895.
- Wood, D.H. 2018, Application of extended vortex theory for blade element analysis of horizontal-axis wind turbines. *Renewable Energy*, 121:188–194. ISSN 09601481. doi: 10.1016/j.renene.2017.12.085.
- Wood, D.H.; Okulov, V.L., and Bhattacharjee, D. 2016, Direct calculation of wind turbine tip loss. *Renewable Energy*, 95:269–276. ISSN 0960-1481. doi: 10.1016/j.renene.2016.04.017.
- Wu, T.Y. 1962, Flow through a heavily loaded actuator disc. *Schiffstechnik*, 9(47):134–138.

- Xiao, J.; Wu, J.; Chen, L., and Shi, Z. 2011, Particle image velocimetry (PIV) measurements of tip vortex wake structure of wind turbine. *Applied Mathematics and Mechanics*, 32(6): 729–738. ISSN 0253-4827. doi: 10.1007/s10483-011-1452-x.
- Xiros, M.I. and Xiros, N.I. 2007, Remarks on wind turbine power absorption increase by including the axial force due to the radial pressure gradient in the general momentum theory. *Wind Energy*, 10(1):99–102. ISSN 10954244. doi: 10.1002/we.203.
- Yoon, S.S. and Heister, S.D. 2004, Analytical formulas for the velocity field induced by an infinitely thin vortex ring. *International journal for numerical methods in fluids*, 44:665–672. doi: 10.1002/fld.666.

# Index

- actuator disc, 1–11, 13, 20, 21, 23, 25, 27, 29, 31, 33–35, 38–40, 42–44, 47, 50, 51, 57, 61, 63, 71, 80, 81, 94, 97–101, 115  
adding energy, 10, 23, 38, 50, 57, 61, 69, 71, 73–77, 80  
extracting energy, 5, 10, 38, 42, 50, 57, 59, 61, 63, 69, 70, 72, 74–77, 79, 80, 99, 104  
actuator line, 7, 8, 13, 17, 18, 38, 42, 81, 93, 94, 98, 100–104  
AL, *see* actuator line  
angular momentum, 3, 19, 28, 42, 63, 69, 80, 111, 112  
annulus, 9, 10, 33, 44, 46, 47, 57–59, 61, 78, 97  
balance of  
  energy, 2, 21, 22, 63, 67–69, 78, 79  
  mass, 63, 67  
  momentum, 2, 3, 22, 43–46, 57, 59, 61, 63, 65–68, 70, 73, 77, 78, 80, 92, 99, 102, 105  
balance of angular momentum, *see* angular momentum  
BEM, *see* Blade Element Momentum  
Bernoulli, 10, 14, 16, 19, 22, 23, 27, 34, 42, 45, 51, 54, 55, 57, 65–67, 75, 82  
Betz-Goldstein distribution, 4, 63, 73, 79, 98  
Betz-Joukowsky limit, 5  
Blade Element Momentum, 2, 5, 7–9, 11, 13, 36, 57, 59, 97, 98, 102, 105  
boundary layer, 1, 8  
circulation, 3, 8–11, 17, 25–31, 63, 79, 81, 85, 86, 88, 90–92, 94, 97, 98, 100, 102, 104  
conservative forces, *see* forces  
contraction, *see* wake contraction  
design, 5, 7–9, 33, 36, 86, 97, 103, 105  
drone, 4
- efficiency, 5, 10, 50, 63, 69, 72, 73, 79  
elliptic wing, 86, 93  
energy  
  conservation, 10, 13, 79  
  conversion, 9, 13, 22, 37, 40  
  kinetic, 3, 20–23, 34, 79, 80  
  potential, 10, 19, 22, 23, 34, 79  
energy balance, *see* balance  
Euler equation, 9, 13, 15, 19, 21, 25, 34, 63, 81, 84, 111  
expansion, *see* wake expansion  
forces  
  conservative, 10, 19, 22, 23, 26, 43, 45, 46, 58, 78, 81, 86, 93–95  
  non-conservative, 10, 13, 17, 22, 23, 25, 26, 31, 34, 94, 95  
helicopter, *see* rotor  
Helmholtz, 10, 25–27, 31  
hover, 1, 4, 5, 8, 30, 43, 45, 72, 89, 103  
induction, 9, 38, 50, 55, 59, 71, 73, 85, 97–105  
Joukowsky distribution, 9, 63, 79, 98, 99, 105  
kinetic energy, *see* energy  
lifting line, 4, 7, 17, 18, 29, 35, 36, 38, 42, 98, 100–102, 104  
LL, *see* lifting line  
mass balance, *see* balance  
momentum balance, *see* balance  
non-conservative forces, *see* forces  
performance, 1, 3, 4, 21, 31, 47, 50, 63, 79, 80, 97, 102, 105  
potential energy, *see* energy  
propeller, *see* rotor  
propeller disc, *see* actuator disc adding energy

- Rankine vortex, 28, 37, 63, 81, 82, 84  
rotational speed, 3, 8, 10, 21, 33, 37, 42,  
43, 63  
rotor  
  propeller, 1–5, 7, 43, 61, 69–71, 73, 80,  
    86, 89, 103, 120  
  helicopter rotor, 1, 4, 5, 7, 45, 89  
  ship screw, 1, 3  
  wind turbine rotor, 1, 7, 36, 81, 86, 87,  
    89, 95  
screw, *see* rotor  
swirl, 7, 10, 19, 23, 29–31, 37, 56, 61, 63,  
65, 66, 69, 71, 73–76, 78–80, 82, 84,  
111  
tip correction, 7, 9, 11, 93, 95, 97–100,  
102, 104  
tip vortex, 25, 31, 81, 85, 86, 91, 93, 95,  
101, 102, 104  
turbulence, 1, 7, 8, 40  
vorticity  
  conservation, 13, 26  
  convection, 27, 29, 30, 86  
  generation, 18, 19, 25, 27, 31, 81, 83, 84  
  stretching, 18, 29, 30, 112  
  tilting, 18, 29, 30  
wake, 3, 4, 7, 10, 19–22, 27–31, 34–45, 47,  
50, 63–65, 67, 69–76, 79, 82, 84–86,  
100, 104, 115–117  
boundary, 10, 50, 51, 55, 61, 65, 77, 78,  
80, 118, 121  
contraction, 2, 4, 10, 40, 57, 59, 68, 70,  
72, 77, 79, 82, 86, 119  
expansion, 2, 4, 10, 11, 40–42, 50, 51,  
56, 57, 59, 68, 70–73, 75, 77, 79, 81,  
82, 85, 86, 93, 95  
  rotation, 3, 59  
wind energy, 5, 7, 8, 98  
wind farm, 1, 8  
wind turbine disc, *see* actuator disc  
  extracting energy  
wind turbine rotor, *see* rotor